Spatial properties of dayside Pi2 pulsations : Implications for the generation of the oscillating current system from polar to equatorial ionosphere

今城，峻

Kyushu University

Doctoral Thesis

Spatial properties of dayside Pi2 pulsations:

Implications for the generation of the oscillating current system from polar to equatorial ionosphere

Author:
Shun Imajo

Supervisor:
Akimasa Yoshikawa

A thesis submitted in fulfilment of the requirements
for the degree of Doctor of Philosophy

in the

Graduate School of Science
Department of Earth and Planetary Sciences

February 2016

Declaration of Authorship

I, Shun Imajo, declare that this thesis titled, 'Spatial properties of dayside Pi2 pulsations: Implications for the generation of the oscillating current system from polar to equatorial ionosphere' and the work presented in it are my own. I confirm that:

- This work was done wholly or mainly while in candidature for a research degree at this University.

- Where any part of this thesis has previously been submitted for a degree or any other qualification at this University or any other institution, this has been clearly stated.

- Where I have consulted the published work of others, this is always clearly attributed.

- Where I have quoted from the work of others, the source is always given. With the exception of such quotations, this thesis is entirely my own work.

- I have acknowledged all main sources of help.

- Where the thesis is based on work done by myself jointly with others, I have made clear exactly what was done by others and what I have contributed myself.

Signed:

_____

Date:

_____

Abstract

Doctor of Philosophy

Spatial properties of dayside Pi2 pulsations: Implications for the generation of the oscillating current system from polar to equatorial ionosphere

by Shun Imajo

To know impacts of magnetospheric electromagnetic disturbances on the ground, it is important to understand the physical process of the disturbance propagation depending on source locations and temporal-spatial scales. The Pi2 pulsation, which is a type of geomagnetic pulsations, is considered a useful natural signal for investigating the propagation of the disturbance from a localized source in the nightside magnetosphere to the distant dayside magnetic equator on the ground. The Pi2 observed at the dayside magnetic equator shows the amplitude enhancement, which has been interpreted as evidence of the polar-to-equatorial coupling of the ionosphere. However, this interpretation has not been supported by clear evidence and the structure and physics of the coupling is poorly understood. The purpose of this thesis is to present detail observations of dayside and terminator Pi2s and provide a quantitative interpretation of the observational results by a numerical model.

The thesis first clarified effects of the dawn and dusk terminators on Pi2 pulsations. I examined Pi2 pulsations observed simultaneously at middle-to-low latitude stations around the dawn and dusk terminators. It was found that the phase reversal of the D component occurred around the dawn and dusk terminators whereas the H component was nearly in phase. The D component was in antiphase with respect to the magnetic equator in not only darkness but also sunlight. A statistical analysis using Pi2 events that occurred during 1 November 2011 to 31 October 2012 showed that some features of Pi2s were controlled by the relative location of the terminator (at 100 km in altitude, the highly conducting E region) rather than local time. The phase reversal of the D component occurred $0.5 - 1$ h after sunrise and $1 - 2$ h before sunset. The D-to-H amplitude ratio on the dawn side started to increase at sunrise and reached a peak at

near 2 h after sunrise, while the D-to-H amplitude ratio on the dusk side reached a peak at sunset. The change of the features controlled by the terminator cannot be explained by only existing models (e.g., plasmaspheric resonance, substorm current wedge oscillation). I suggested that the terminator effect can be explained by a change of magnetic effects from the nightside FAC to the meridional ionospheric current flowing on the sunlit side of the terminator, and vice versa. The meridional current is expected to be a part of the dayside current system including the equatorial Cowling current.

I analyzed Pi2 events using at least 36 magnetometers in the dayside middle-to-equatorial latitude (geomagnetic latitude lower than 60° and the sunlit region at 100 km in altitude) to examine the dayside ionospheric current system. I derived equivalent current distributions, which are a useful approach to visualize an ionospheric current structure if the magnetic effect of ionospheric current is dominant in an examined region. Equivalent current vectors of Pi2 are determined by rotating filtered horizontal magnetic field vectors at the local maxima of horizontal amplitude ($\sqrt{\Delta H^2 + \Delta D^2}$, where ΔH and ΔD are bandpass filtered north-south and east-west component geomagnetic data, respectively, with a period of 40 to 150 s) by an angle of 90 degrees clockwise. The local maxima of horizontal amplitude of Pi2 are nearly coincident at overall dayside stations, indicating that their oscillations directed in the major axis are nearly in phase. The meridional component of equivalent current vectors was reversed between in the prenoon sector and the postnoon sector, so as to connect the equatorial equivalent current to higher latitude regions. The equivalent currents exhibited the prenoon-postnoon asymmetry that the ratio of the meridional component to the zonal component in prenoon sector was larger than that in the postnoon sector. It was confirmed that the averaged features are consistent with features of the individual events using the case studies. Taking into account the prenoon-postnoon asymmetry of D-to-H amplitude ratio, I inferred that the meridional current intensively flows into the equator in the prenoon sector and gradually returns from the equator in the postnoon sector.

The present observational results imply that dayside Pi2 is associated with oscillating ionospheric current. To quantitatively examine the proposed model current system, I calculated the ground magnetic field produced by the three-dimensional current system consisting of FACs localized in the nightside auroral region, the magnetospheric closure current, and the ionospheric current produced by the FACs. It was assumed that the FACs flowed along the dipole field line, and the magnetospheric closure current flowed in azimuthal direction to connect between equatorial footprints of the center of the FACs. The ionospheric current was derived by numerically solving the global electrostatic potential distribution. The simulated ionospheric current on the dayside showed the similar pattern to the observed equivalent current on the dayside. The simulated equivalent current also showed the similar pattern to the observed equivalent current on

the dayside, indicating that the ionospheric current mainly contributed to the dayside equivalent current. On the other hand, since the ionospheric current is very weak in the nightside low latitudes, the magnetospheric current mainly contributed to the magnetic field in this region. The sense of both simulated H and D magnetic fields is consistent with the longitudinal phase variation of the observed Pi2. By separation of contributions of each current element, it was found that D component phase reversals around the terminator are caused by a change between magnetic effects of FACs and meridional ionospheric currents.

While the previous Pi2 model for low latitudes have not quantitatively explained the observational result, the proposed model current system well explains the magnetic vector (or equivalent current vector) of Pi2 magnetic perturbation. The asymmetry of the dayside ionospheric current is considered to be due to the Hall current and its polarization field. The formation of the polar-to-equatorial ionospheric current implies that the global Cowling channel can be applied to the nightside-source phenomena. I concluded that Pi2 pulsations are sent to the dayside ground by the quasi-electrostatic oscillating ionospheric current formed in the polar-to-equatorial region driven by localized nightside FACs.

Acknowledgements

Contents

List of Figures

List of Tables

Abbreviations

FAC	**F**ield-**A**ligned **C**urrent
GM	**G**eo**M**agnetic
IC	**I**onospheric **C**urrent
MCC	**M**agnetospheric **C**losure **C**urrent
MHD	**M**agneto**H**ydoro**D**ynamics
MLT	**M**agnetic **L**ocal **T**ime
LT	**L**ocal **T**ime
SC	**S**udden **C**ommencement
SCW	**S**ubstorm **C**urrent **W**edge
SI	**S**udden **I**mpulse
ULF	**U**ltra-**L**ow **F**requency

Chapter 1

General Introduction

1.1 Propagation of Magnetospheric Disturbances to the Ground Surface

The Earth is surrounded by the plasma originating from the Earth's atmosphere and the solar wind which is the outflow of the coronal gas. The ionosphere is the region at $\sim 80-1000$ km in altitude filled with dense Earth's atmosphere ionized by the solar radiation and particle precipitation. The outside of the ionosphere is the magnetosphere that is the cavity formed by the Earth's magnetic field in the solar wind. The ionosphere electrodynamically interacts with the magnetosphere, and the energy is exchanged between both regions. Various types of the electromagnetic disturbance are generated in the magnetosphere by the direct and/or loading-unloading processes. These disturbances are transmitted in various modes to the ground surface. The reach of the disturbance can be seen as the variation of the ground magnetic field. If the variation is very large, large induced electric fields have potential impacts on transmission lines, pipe lines, and sensitive electronic devices. To know impacts of magnetospheric electromagnetic disturbances on the ground, it is important to understand the physical process of the disturbance propagation depending on source locations and temporal-spatial scales.

The electric current plays an important role in the transmission of low-frequency disturbances. These disturbances typically originate from the magnetospheric current perpendicular to the Earth's main field. The perpendicular current is driven by the opposite drift motion between the ion and the electron due to forces of the inertia, the magnetic

pressure gradient, and the plasma pressure gradient. If the perpendicular current $(\boldsymbol{j}_\perp)$ converge, the field-aligned current $(\boldsymbol{j}_{//})$ diverge because of the current continuity law

$$-\nabla \cdot \boldsymbol{j}_\perp = \nabla \cdot \boldsymbol{j}_{//} = \mathrm{B}_0 \frac{\partial}{\partial s} \left(\frac{j_{//}}{\mathrm{B}_0} \right), \tag{1.1}$$

where $\boldsymbol{j}$ and s are the magnetospheric current and the displacement along the background magnetic field $\mathbf{B_0}$.

The field-aligned currents $j_{//}$ (FACs), which are the magnetospheric current parallel to the the background magnetic field, transmit the magnetospheric current into the ionosphere. Assuming that the thickness of the ionosphere is negligible, the current flowing into the ionosphere is diverge the horizontal direction. Considering the current continuity, the equation is given by

$$\boldsymbol{j}_{//} = \nabla \cdot \mathbf{J}. \tag{1.2}$$

Here $\mathbf{J}$ represents the the height-integrated current density of the horizontal ionospheric current. The distribution of $\mathbf{J}$ can be given by the Ohm's law as:

$$\mathbf{J} = \mathbf{\Sigma} \cdot \mathbf{E}, \tag{1.3}$$

where $\mathbf{E}$ and $\mathbf{\Sigma}$ are the ionospheric horizontal electric field the ionospheric height-integrated conductivity tensor. The distribution of the $\mathbf{J}$ is complicated because the $\mathbf{\Sigma}$ is nonuniform and highly variable. $\mathbf{E}$ can be modified by the polarization charge to ensure current continuity, and the divergence of the ionospheric current at the conductivity edge causes the FAC driven in the ionosphere (e.g., *Ellis and Southwood*, 1983; *Glassmeier*, 1983; *Itonaga and Kitamura*, 1988). If the time derivative of the ionospheric current is significant, rotational ionospheric electric field arises and the Hall current can diverge even if the conductivity is uniform (e.g., *Yoshikawa*, 2002). Thus the real current system becomes complicated.

The magnetic disturbances that have much smaller amplitude than $\mathbf{B_0}$ can propagate in the plasma as magnetohydrodynamic (MHD) waves. The fast mode (magnetosonic)

wave, which is a compressional wave mode of MHD wave modes, can propagate in the direction perpendicular to the background magnetic field. The fast mode wave involve in the perpendicular current that flows along the wavefront. The perpendicular current diverges if there are inhomogeneous medium and curvilinear magnetic field line (e.g., *Tamao*, 1964; *Itonaga and Yoshikawa*, 1996). The divergence of the current acts as a source of the shear Alfvén waves, which are involved in FACs. MHD waves sometimes give rise to resonance structures, which are a cause of low-frequency magnetic oscillations.

Thus the ground magnetic field contains multiple components of magnetic fields transmitted by the various mechanisms and paths. The spatial distributions of the features of the magnetic variation, such as polarization, amplitude, and phase and time delays, provide information for understanding a full picture of propagation of the magnetic disturbance.

1.2 Equatorial enhancement of Magnetic Disturbances

1.2.1 Observations

The magnetic equator, which is the line where the magnetic inclination is zero, is recognized as a special region in the ionospheric electrodynamics. One of the most unique phenomena at the magnetic equator shows the equatorial electrojet (EEJ) that is stronger daily variation of magnetic field than at low-to-middle latitudes (see a review by *Forbes* (1981)).

Not only EEJ but also most of disturbance originating from the magnetosphere exhibits the enhancement of their amplitude at the magnetic equator.

Ferraro and Unthank (1951) statistically examined local time dependences of the H amplitude of sudden commencements (SCs) and sudden impulses (SIs). They found that the local time dependence at Huancayo at the magnetic equator differed from those at the low- and middle- latitude stations; the amplitude maximum occurred around 12 h LT (local time) at Huancayo (GMLat$= -0.3°$) while at the other station the amplitude maximum occurred in premidnight. *Sugiura* (1953) showed that the local time dependence of the amplitude ratio between Cheltenham (GMLat$=50.1°$) and Huancayo had a

peak at 10 h LT, and the peak value was about 6. This enhancement of SCs and SIs at the dayside magnetic equator have been confirmed by subsequent researches (*Forbush and Vestine*, 1955; *Maeda and Yamamoto*, 1960; *Matsushita*, 1960). (*Araki*, 1977) exhibited that onsets of the SCs in high to equatorial dayside region are almost simultaneous when the observed types of SCs (SC* that accompanies with the preliminary reversal impulse or pure SC) were same among stations.*Nishida* (1968) investigated the DP2 event observed simultaneously over the globe. They found that DP2 fluctuations were very similar in all latitude with little time delay. *Mene et al.* (2011) statistically derived the local time distribution of the amplitude ratio of DP2s observed between equatorial latitudes and low latitudes, and showed that the enhancement ratio had a peak near 12 LT. The longitudinal dependence showed that the enhancement ratio at the American sector (about 8) is larger than those at the African and Asian sectors (about 3−6).

The equatorial enhancement is also shown in geomagnetic pulsations. *Yanagihara and Shimizu* (1966) found that the amplitude of dayside Pi2 is enhanced near the magnetic equator although the source of Pi2 is believed to be located on the nightside. *Trivedi et al.* (1997) showed the latitudinal profile of power of Pc5 pulsations in the high-to-equatorial latitudes, and found that the power occurred peaks at magnetic equator and high latitudes. *Sarma and Sastry* (1995) investigated the enhancement ratio of Pc pulsation with a period of less than 20 s and compared to other longer period phenomena. Figure 1.1 shows local time dependence of the enhancement ratios of various phenomena. The longer period phenomena (Daily variation, SC, Pi2, Pc3, and Pc4) show 2−3 times larger enhancement on dayside in the same manner. On the other hand, shorter period pulsation exhibited no enhancement on the dayside, but a small enhancement appears on the dusk side.

1.2.2 Theoretical and Numerical Models

The cause of enhanced magnetic variations itself is explained by enhanced ionospheric current due to Cowling effect, which is theoretically established by *Hirono* (1950a,b, 1952).

Figure 1.2 shows a picture of the Cowling effect at the magnetic equator. It is assumed that the initial electric field is directed eastward in the highly conducting ionospheric layer (typically E layer). Upper and lower sides of this layer have a very low conductivity.
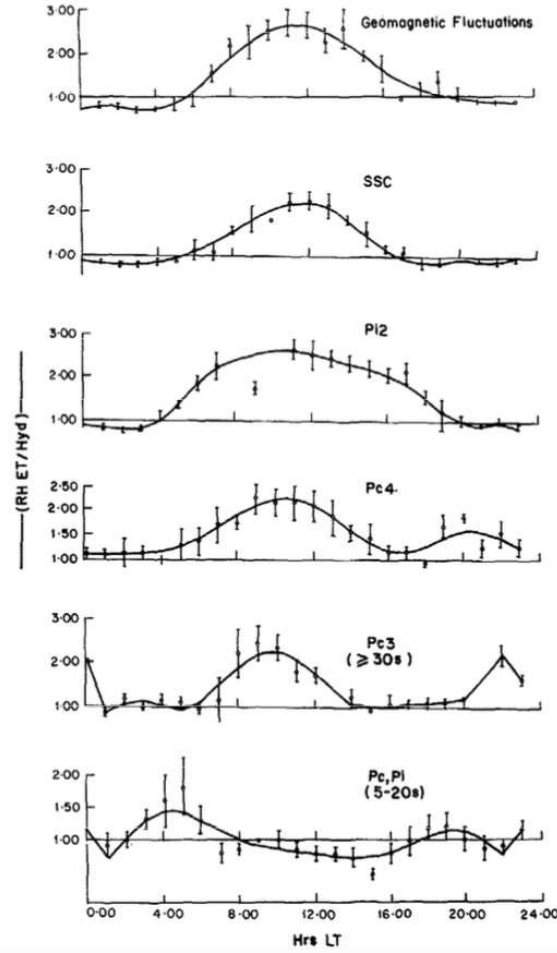
FIGURE 1.1: local time dependence of the enhancement ratios of various phenomena
(*Sarma and Sastry*, 1995).

The initial electric field drives the eastward Pedersen current and the downward Hall current. The downward Hall current creates polarization charges at the boundaries of the conducting layer because weak currents flow outside of the conducting layer. Thus the secondary upward electric field generated by the polarization charges. The secondary electric field drives the secondary upward Pedersen current and the secondary eastward Hall current. The secondary Pedersen current cancels out the primary Hall current, ensuring current continuity of vertical direction. The secondary Hall current flows in the same direction to the primary Pedersen current, enhancing zonal currents. Although the enhancement is caused by the vertical secondary electric field, this effect is usually treated as the enhancement of the conductivity. This enhanced conductivity is called Cowling conductivity:
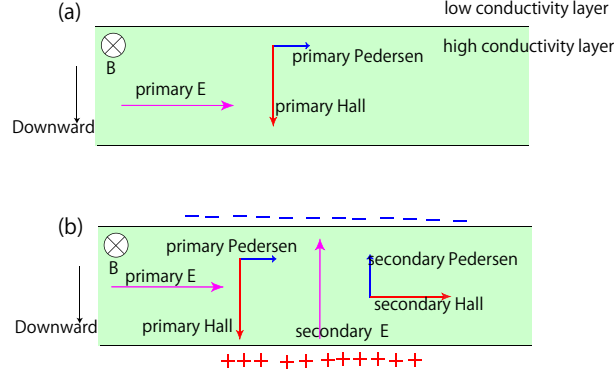
FIGURE 1.2: A picture of the Cowling effect at the magnetic equator.

$$\sigma_C = \sigma_P + \frac{\sigma_H^2}{\sigma_P} \tag{1.4}$$

where σ_P and σ_H are Pedersen conductivity and Hall conductivity. The ratio of Cowling current ($J_C = \sigma_C E$) to the primary Pedersen current ($J1_P = \sigma_P E$) is determined by the ratio of the Hall conductivity to the Pedersen conductivity. $J_C/J1_P$ is 5-17 for the typical σ_H/σ_P of $2-4$ (*Baumjohann and Treumann*, 2012).

Similar magnetic variations from the polar region to the equatorial region and the latitudinal amplitude profile imply that the these variations are produced by the global ionospheric current system driven by the electric field transmitted to the polar ionosphere via FACs. The fact that time lags of SCs and DP2s between polar and equatorial regions are very small ($\leq$10 s) means that the electric field is instantaneously distributed toward the equatorial region.

Kikuchi and Araki (1979a) analytically examined the transient response of the step-like disturbance in the ionosphere. In the F-region, which can be assumed to be an anisotropic metallic medium, the electric field is transmitted by the diffusion mode. However, it takes about 1 h to start the increase the electric field in the equator when the source is located in the polar region. On the other hand, in the F-region of upper 500 km, the electric field can propagate as MHD waves. The Alfveń speed in the F-region ionosphere is typically $1000-10000$ km/s (e.g., *Jacobs and Watanabe*, 1962), and the MHD wave in the ionosphere may be possible for nearly instantaneous transmission although the speed is highly variable with the altitude and solar radiation flux. Another physical mechanism for the efficient and instantaneous transmission of electric fields is

proposed by *Kikuchi and Araki* (1979b). They suggested that the electric field carried by the TM_0 mode wave in the atmospheric wave guide at the speed of light (Figure 1.3).
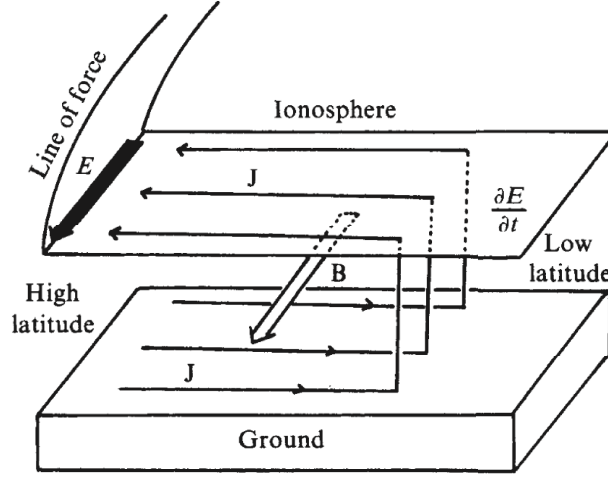
FIGURE 1.3: The picture of the TM_0 mode wave model. (*Kikuchi et al.*, 1978)

The global ionospheric current system produced by FACs has been reproduced by numerical calculations (*Tsunomura and Araki*, 1984; *Tsunomura*, 1999). The method of calculating the global ionospheric current distribution in these studies is based on the electrostatic approximation, the current continuity, and the Ohm's law. In their model, the ionosphere is assumed to be the two-dimensional thin spherical shell, so the effect of the vertical polarization electric field cannot be reproduced. Instead, they modified the conductivity near the magnetic equator considering the Cowling effect. The distribution of the ionospheric current showed that the middle-to-low latitude ionospheric current flowed in and out the equatorial region. The equatorial enhancement in the H component is successfully reproduced (Figure 4 in *Tsunomura* (1999)).

Although the propagation of electric field and structure of the ionospheric current have been discussed, it is still unclear how the polar-to-equatorial ionospheric current system is formed. *Kikuchi et al.* (1996) proposed that the equatorial Cowling current is directly connected to ionospheric footprints of DP2-associated FACs by Pedersen current. *Kikuchi et al.* (2003) and *Hashimoto et al.* (2011) argued that during the substorm the counterelectrojet, which flows in an opposite direction to an equatorial electrojet, is caused by the amplified Pedersen current driven by the westward electric field penetrated from the region-2 FACs. However, the Pedersen current at low-to-high latitude connecting the FACs to the equatorial ionospheric current may not be strong to provide

enough current to the equatorial region because the conductivity in the low-to-high lat-itude is not high compared to that in the equatorial region. Recently, *Yoshikawa et al.* (2012) suggested that the Cowling effect at the dawn and dusk terminators contributes to the closure of the polar-to-equatorial ionospheric current system.

Chapter 2

Propagation of Pi2 Pulsation

2.1 General Introduction of Pi2 Pulsation

The geomagnetic pulsation, which is also known as the ULF (Ultra-Low Frequency) wave, is low-frequency oscillations of the geomagnetic field. Geomagnetic pulsations are classified by a waveform feature and a period (table 2.1) (*Jacobs et al.*, 1964). Pc-type pulsations are regular and long-duration oscillations while Pi-type pulsations are irregular and short-duration oscillations. The number following the waveform-type symbol (Pc or Pi) expresses the classification by period, in which a larger number has a larger period. Pi2 pulsations, which are studied by this thesis, are defined as the Pi-type pulsation with a period of $40-150$ s. Note that this classification does not always have a physical meaning.

Type		Period range (sec)
	Pc 1	$0.2- 5$
	Pc 2	$5- 10$
Continuous pulsations	Pc 3	$10- 45$
	Pc 4	$45-150$
	Pc 5	$150- 600$
Irregular pulsations	Pi 1	$1- 40$
	Pi 2	$40-150$

TABLE 2.1: The classification of geomagnetic pulsations

Pi2 pulsations are typically observed on the nightside accompanying the onset of the substorm expansion phase, pseudobreakups, poleward boundary intensifications or auroral streamers (e.g., *Saito et al.*, 1976; *Sakurai and Saito*, 1976; *Yeoman et al.*, 1994;

Lyons et al., 1999; *Liou et al.*, 2000; *Voronkov et al.*, 2003; *Nishimura et al.*, 2012).
Pi2 pulsations have been often discussed in the terms of the triggering mechanism of substorm, which is one of the most puzzling problem of the upper-atmospheric physics. Relations between Pi2 and other substorm phenomena have been studied not only for understanding of the Pi2 itself but also for understanding of the substorm onset process.

It can be said that Pi2 pulsations are useful natural signals to understand the propagation of the disturbance in magnetospheric and ionospheric plasmas. The Pi2 pulsation shows distinctive and clear variations in the magnetic field, and they can be relatively frequently observed (several times per day) in a wide region compared with other phenomena. The association with nightside auroral activities implies that the source of Pi2 is located in the nightside magnetosphere. The spatial distributions of amplitude and propagation delay also supported that the source (or energy source) of Pi2 is localized in the magnetotail region (e.g., *Uozumi et al.*, 2007; *Chi et al.*, 2009; *Keiling et al.*, 2014). *Uozumi et al.* (2007) concluded that the averaged location of the source region is 22.5 h MLT (magnetic local time) and 10 R_E using the spatial distribution of delay times and the numerical propagation model.

Pi2 magnetic signals are probably transmitted from the source region to the nightside ground by MHD waves, FACs, and ionospheric currents. In the low-latitude nightside region, Pi2 pulsations or the impulse triggering the plasmaspheric resonance mainly propagate as the fast mode wave in the magnetosphere (e.g., *Yumoto et al.*, 1989; *Takahashi et al.*, 1995; *Kepko and Kivelson*, 1999; *Takahashi et al.*, 2003; *Imajo et al.*, 2014). In the middle-latitude region, it is possible that Pi2 pulsations are transmitted as the fast mode wave in common with low latitudes, the Alfvén wave driven by fast mode waves (e.g., *Kepko et al.*, 2001; *Uozumi et al.*, 2004), and oscillations of wedge-like FACs (e.g., *Lester et al.*, 1983; *Uozumi et al.*, 2009). In the high-latitude nightside region, it is considered that Pi2 pulsations are observed as magnetic fluctuations produced by FACs and ionospheric currents (e.g., *Wilhelm et al.*, 1977; *Samson*, 1982; *Olson*, 1999). Pi2 pulsations are even observed in low-latitude and equatorial regions on the dayside ground (e.g., *Yanagihara and Shimizu*, 1966; *Kitamura et al.*, 1988; *Sutcliffe and Yumoto*, 1989), indicating that they can propagate to the dayside ground from the nightside magnetotail region.

Although generation mechanisms of Pi2 frequency are not a main subject of this study,

I briefly mention models of Pi2 generation and their complexity because generation mechanisms are limited by propagation mechanisms. Various generation models have been proposed, but no single model can explain all properties of Pi2. Figure 2.1 shows existing models of Pi2 generation and their possible relation to various regions *Keiling and Takahashi* (2011). More than one possible mechanisms can exist simultaneously, and related regions vary with models. This complexity makes it difficult to achieve consensus on physical and morphological understanding of Pi2 (See a review by *Keiling and Takahashi* (2011) for more detail).
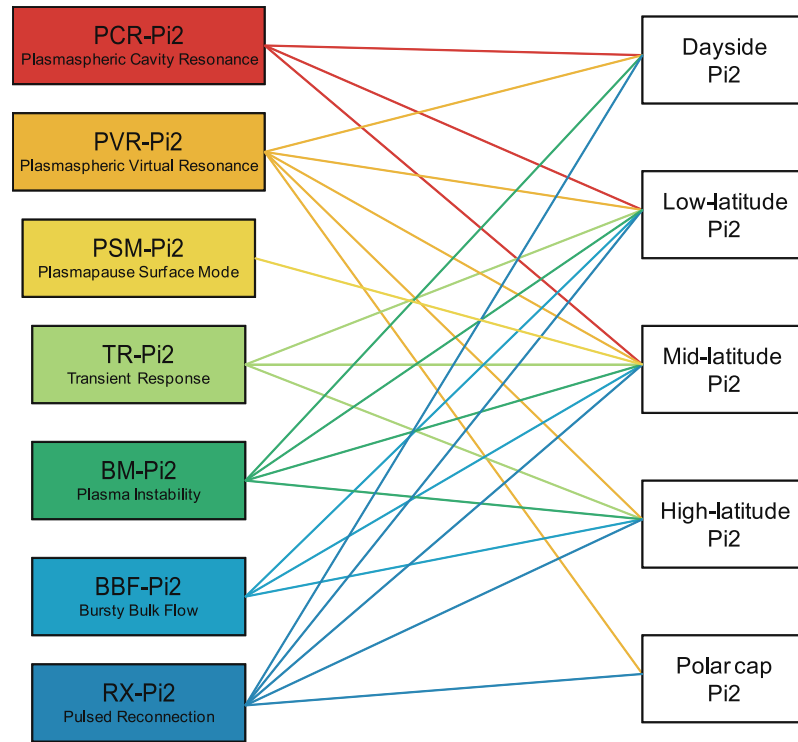
FIGURE 2.1: The diagram of existing models of Pi2 generation and their relation to various regions. (*Keiling and Takahashi*, 2011)

2.2 Nightside Pi2 Pulsations

2.2.1 Nightside Pi2 Pulsations as Electric Current Fluctuations

Nightside Pi2 pulsations, especially in the auroral region, have been discussed in terms of current fluctuations of the substorm current system. *Boström* (1972) first proposed this association by a theoretical consideration. *Wilhelm et al.* (1977) suggested that their observations of localized features of Pi2 pulsations near the auroral electrojet can be

explained by not the MHD-wave propagation but fluctuations of the auroral electrojet (for H fluctuations) and FACs (for D fluctuations).

Equivalent currents associated with Pi2 have been studied from the perspective of the relation to the substorm current system. *Pashin et al.* (1982) analyzed equivalent currents associated with Pi2 fluctuations in the region of the substorm westward electrojet. The equivalent current vectors exhibited a two-vortices pattern, which differed from the equivalent current structure associated with the substorm current. *Lester et al.* (1985) performed a similar analysis and reproduced their observational result using a model governed by the field line resonance.

The substorm current wedge (SCW) is the three dimensional large-scale substorm current system localized in the midnight sector. Figure 2.2 is a traditional picture of SCW that consist a pair of upward and downward FACs and westward ionospheric closure current (*McPherron et al.*, 1973). The SCW has been believed to be set up by the sudden divergence of the cross tail current (current disruption (e.g., *Lui*, 1996)), however, causes of the divergence of the current are not fully understood. The upward and downward FACs of the SCW current system produce the magnetic field in the middle-to-low latitude. As shown in the longitudinal variation in Figure 2.2, the H component is positive and maximized at the central meridian of SCW, while the D component changes the sense from positive to negative at the central meridian of SCW.

Lester et al. (1983) and *Lester et al.* (1984) demonstrated that the longitudinal variation of azimuthal angles of Pi2 in the middle latitude was similar to that of the magnetic bay caused by the SCW. The major axes of Pi2 pulsations were directed in the particular meridian in the higher latitude region. However, the centers of the SCW and Pi2 occurred at the same meridian for only ∼65% of their events (the center of Pi2 is defined as the meridian where the sense of an azimuth angle changes). This suggests that the Pi2 is not always the oscillating component of the substorm current system, and may have a different configuration from the SCW.

Some researchers have been studied relations between Pi2 magnetic oscillations and other quantities related to the current. *Keiling et al.* (2008) showed the substorm event that ground Pi2, photon flux observed by the POLAR satellite, and ion energy flux in the near-Earth plasma sheet were one-to-one correlated. They proposed that a local plasma instability (such as ballooning mode) caused the wave-like structure in the
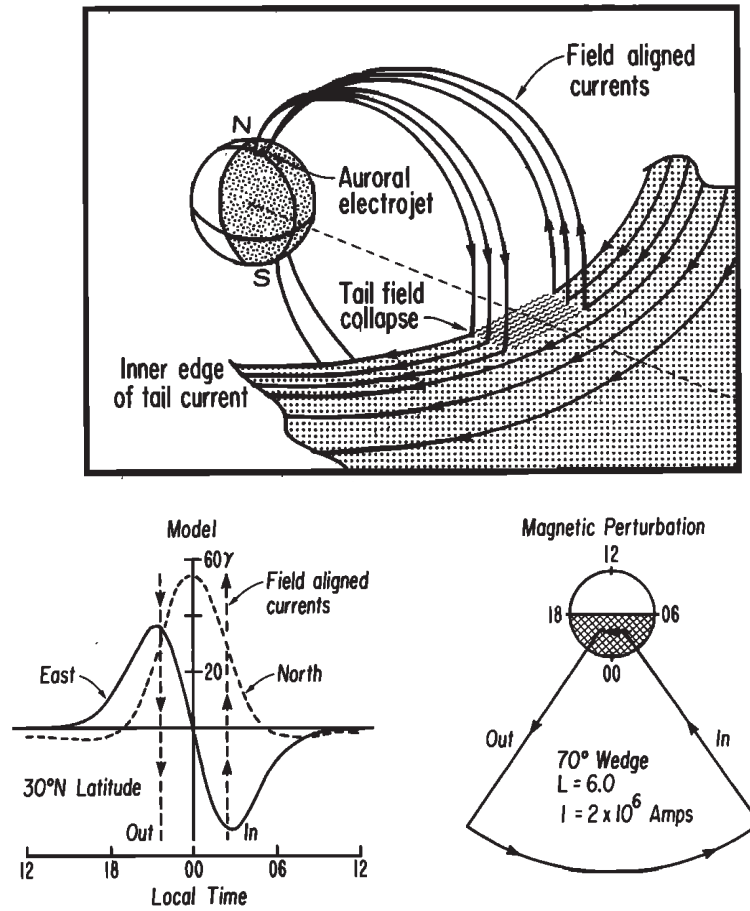
FIGURE 2.2: Pictures of the original SCW model. (*McPherron et al.*, 1973)

plasma sheet and oscillating FACs which drive ground Pi2 oscillations. *Uozumi et al.* (2011) found that the time derivative of the height integrated auroral kilometric radiation (AKR) synchronized with D component ground Pi2s. They suggested that D component ground Pi2s were generated by the oscillating SCW-like FACs because the AKR were related to the FACs. *Nishimura et al.* (2012) showed that each Pi2 pulse in the middle-to-equatorial region was coincident with each auroral intensification, and their amplitudes were correlated with the auroral intensity. These results indicated that the Pi2 was related to oscillating FACs, which cause the quasi-periodic variation of the auroral intensity. *Panov et al.* (2013) demonstrated that the oscillating component of

magnetospheric perpendicular currents calculated from plasma pressure and bulk velocity was well correlated with the oscillating component of FACs deduced from magnetic data shifted by ~ 50 s forward.

2.2.2   Nightside Pi2 Pulsation as MHD Waves

It is accepted that some parts of compressional component Pi2s observed on the low-latitude nightside are produced by fast mode waves. There are two types of mechanisms that explain the generation of fast mode waves associated with Pi2.

One is the plasmaspheric resonance which includes the plasmaspheric cavity resonance (PCR) (e.g., *Saito and Matsushita*, 1968) and the plasmaspheric virtual resonance (PVR) (e.g., *Lee and Takahashi*, 2006). The PCR is a model that an impulsive fast mode wave generated in the magnetotail is trapped between the plasmapause as an outer boundary and the ionosphere as an inner boundary. The trapped fast mode wave is resonated and radial standing harmonic waves are generated. The frequencies of lower-order harmonics are approximately consistent with the Pi2 frequency band (e.g., *Yeoman and Orr*, 1989; *Lin et al.*, 1991; *Itonaga et al.*, 1992). The PVR is similar to PCR, but the standing wave structure of PVR is extended beyond the plasmapause. In the case of PCR, the plasmasphere is treated as a perfect reflector, while in the case of PVR, the plasmasphere is not a perfect reflector and some energy escapes beyond the plasmasphere. The strong evidence of the existence of plasmaspheric resonance is the phase relation of the electric field and magnetic field in the magnetosphere. The radial standing fast waves do not transport energy in the radial direction, which means that the time-averaged radial Pointing flux is zero. Many previous studies have shown that azimuthal electric field oscillations are delayed by 90° against compressional magnetic field oscillations in the low-latitude magnetosphere (*Takahashi et al.*, 2001, 2003; *Collier et al.*, 2006; *Kwon et al.*, 2012; *Ghamry et al.*, 2015).

The other is the direct driven possess. In this process, the source periodically perturbed directly drives the Pi2 wave that propagates as MHD waves. This concept has been developed by associating Pi2 magnetic oscillations with oscillations in other physical value (e.g., flow velocity, plasma pressure, ion energy flux) near the possible source region. Also the time delay observed between separated observation points is explained by the propagating wave rather than standing wave (*Kepko and Kivelson*, 1999; *Uozumi*

et al., 2000, 2004; *Keiling et al.*, 2008; *Uozumi et al.*, 2009; *Chi et al.*, 2009; *Uozumi et al.*, 2011; *Murphy et al.*, 2011; *Imajo et al.*, 2014). The possible periodically perturbed sources that have been considered are periodic BBF braking (e.g., *Kepko and Kivelson*, 1999; *Kepko et al.*, 2001; *Hsu et al.*, 2012), periodic reconnection (*Murphy et al.*, 2011), plasma instability (*Keiling et al.*, 2008; *Keiling*, 2012), and overshoots and bounces of BBF (*Panov et al.*, 2010). The direct driven process is often associated with not only generation of periodic MHD waves but also generation of the oscillating wedge-like current system.

2.3 Dayside Pi2 Pulsations

The number of studies of the dayside Pi2 pulsations is very small compared to that of the nightside Pi2. One reason may be that the dayside Pi2 pulsation is relatively difficult to be detected due to the small amplitude and large dayside background variation. Another reason may be that it was not believed that studies of dayside Pi2 provides the insight to the understanding the onset possess of the substorm. However, I argue that studies of dayside Pi2s have significance in understanding the physical process and the path of the disturbance propagation from the nightside magnetosphere to the dayside ground. In this section, I review previous studies of dayside Pi2.

Yanagihara and Shimizu (1966) first reported Pi2 pulsations on the dayside ground. They found that the amplitude of dayside Pi2 is enhanced near the magnetic equator, similarly to other disturbances. The important implication shortly mentioned in their paper is that the equatorial dayside Pi2 may be related to an ionospheric current because the conductivity at the magnetic equator is enhanced by the Cowling effect.

Stuart and Barsczus (1980) indicated that dayside Pi2 rarely observed at the middle-latitude station Eskdamuir (GMlat=58.5). They showed that the period of the low-latitude Pi2 tended to be shorter than nightside Pi2s. Contrary to their results, subsequent studies showed that spectra of nightside Pi2 were similar to that of dayside Pi2 in the low-latitude region (*Sutcliffe and Yumoto*, 1989, 1991; *Itonaga et al.*, 1992; *Nosé et al.*, 2006). *Kitamura et al.* (1988) found that the phase difference of the H component of Pi2 at different stations was much less than 1/10 of the period despite a large longitudinal separation (90°) of the stations. They also found that the phase difference

of the D component at different stations is variable, but a systematic pattern is not clear. The small phase difference and similar spectra of H oscillations have led to the view that dayside Pi2s are a consequence of the plasmaspheric cavity mode with the near-zero azimuthal wavenumber (m number).

Shinohara et al. (1997) reported latitudinal variations of amplitude and phase of H component middle-to-low latitude dayside Pi2. They found that the phase of equatorial Pi2s was delayed by $\sim 30°$ on average relative to that of Pi2s at the off-dip equator. They applied the model of transmission of polar electric field (*Kikuchi and Araki*, 1979b) to the dayside Pi2; the electric field associated with Pi2s in the magnetosphere propagates to the polar ionosphere, and is instantaneously transmitted to the dayside low-latitude and equatorial ionosphere. *Shinohara et al.* (1998) tried to explain the phase delay at the dip equator by inductive effects. They estimated the inductance and resistance of the ionosphere-ground current circuit at the magnetic equator and low latitudes. From their estimation, the phase delay at low latitudes is estimated to be $\sim 5°$ while the phase delay at the dip equator, where the conductivity was assumed to be one order larger than that of low latitudes, is calculated to be $\sim 35°$.

Pi2 pulsations in the upper ionosphere have been investigated using low-altitude satellites. *Han et al.* (2004) reported that the H component of Pi2s observed by the Ørsted satellite in the dayside F-region ionosphere is in antiphase with low-latitude Pi2s observed by ground magnetometers. They suggested that zonal ionospheric currents between the ground and the satellite drove Pi2 magnetic oscillations. On the other hand, *Sutcliffe and Lühr* (2010) argued that Pi2 oscillations were not identified by the CHAMP satellite in the dayside F-region ionosphere even if Pi2s were identified on the dayside ground.

Satellite observations on the dayside magnetosphere showed Pi2 pulsations could not be clearly identified in this region (*Takahashi et al.*, 1995; *Cao et al.*, 2008; *Kwon et al.*, 2012). These results indicate that the fast mode wave associated with Pi2 fully attenuates on the dayside when they propagate sunward in the magnetosphere. In the dawn and dusk regions which are the transition regions between dark and sunlit regions, it has been reported that Pi2 pulsations in the dawn side magnetosphere (before 0600 MLT) tended to have high coherence with ground Pi2s while Pi2s in the dusk side magnetosphere (after 1800 MLT) had low coherence (*Kim et al.*, 2010; *Kwon et al.*, 2012). *Nosé*

et al. (2003) investigated a Pi2 event observed when latitudinally aligned ground stations ($L = 1.45 - 12.6$) and the ETS-VI satellite were located in the magnetic local time between 6.5 and 9.5 h. The ETS-VI satellite located above the geomagnetic equator at $L = 6.3$ and MLT = 6.6 h observed a Pi2 pulsation that had a similar waveform as ground Pi2 pulsations. There was no phase delay between low-latitude X/H component Pi2 pulsations observed around 7 h MLT, 2 h MLT, and 15 h MLT.

2.4 The Problems of Previous Studies and the Approaches of This Study

Although there are implications that the dayside Pi2 is a magnetic fluctuation produced by the ionospheric current, this interpretation is not conclusive nor established in a quantitative manner. If the ionospheric current is important on the dayside, the conductivity distribution should significantly affect features of Pi2. This effect can be tested by examining the Pi2 at the region of a strong gradient of conductivity. The dawn and dusk terminators, which are a boundary between sunlit and dark regions, is a typical location of a strong conductivity gradient. However, Pi2 pulsations observed in the dawn and dusk regions are poorly understood. To the best of my knowledge, only *Saka et al.* (1980) studied the terminator effect on the Pi2 pulsation before the our published work in *Imajo et al.* (2015). *Saka et al.* (1980) observed Pi2 and Pc4 period range pulsations at the single station ASO (GMLat= 22°) near the dawn terminator. They found that an increase in the D-to-H amplitude ratio occurred simultaneously with the E layer ionization at sunrise. They suggested that an increase of the Hall and Pedersen conductivities at the dawn terminator changed the current pattern in the ionosphere, which changed the polarization of pulsations. A problem of their study is that since they compared different events (a pre-sunrise event and post-sunrise event), it was possible that the results were affected by differences between individual events. Today, we can use wide and dense magnetometer networks. I examine Pi2 pulsations observed simultaneously at multiple low-latitude stations around the dawn and dusk terminators. This study will clarify the relation between Pi2 and the location of the terminator. The analysis will be presented in chapter 3.

Although the TM$_0$ mode may explain how the initial electric field propagates to the equator region, the structure of the current closure including the equatorial Cowling current is still an open question. There is no detailed analysis of the spatial distributions of amplitude, phase, and polarization of the dayside Pi2 in the middle-to-equatorial latitude. In particular, previous studies did not carefully compare Pi2 pulsations between in the prenoon sector and in the postnoon sector. I analyze three Pi2 events using at least 36 magnetometers in the dayside middle-to-equatorial latitude (geomagnetic latitude lower than 60° and the sunlit region at 100 km in altitude). I make equivalent current distributions, which are useful approach to visualize an ionospheric current structure if the magnetic effect of ionospheric current is dominant. Also, to investigate averaged features of the local time distribution of dayside Pi2, I statistically analyze dayside Pi2s simultaneously observed in the prenoon, noon, and postnoon secotors. The analysis will be presented in chapter 4.

Although the present observational results will imply that the dayside Pi2 is associated with oscillating ionospheric current, there has been no quantitative current system model comparable to observed dayside Pi2s. In this thesis, I calculate the ground magnetic field produced by the three-dimensional current system consisting of FACs localized in the nightside auroral region, the magnetospheric azimuthal current (partial ring current), and ionospheric current produced by the FACs. The ionospheric current was derived by numerically solving the global electrostatic potential distribution. The numerical simulation will be presented in chapter 5.

The physical process of the formation of the global ionospheric current system produced by nightside FACs has not been discussed. I try to explain the formation process and the asymmetry structure of the current system in the view of the basic nature of the ionospheric current. The global Cowling channel model will be applied to the case of the Pi2 pulsations. The discussion will be presented in chapter 6.

Chapter 3

Solar Terminator Effects on Pi2 Pulsations

3.1 Data descriptions

I use the geomagnetic field data from MAGDAS/CPMN (MAGnetic Data Acquisition System / Circum-pan Pacific Magnetometer Network (*Yumoto and the MAGDAS Group*, 2006, 2007) and INTERMAGNET stations. The station code, the coordinates and LT of each station at 21:50 UT (universal time) are listed in Table 3.1. All the magnetic field data have 1 s time resolution. MAGDAS/CPMN data are expressed in the geomagnetic coordinates (HDZ coordinates). INTERMAGNET data are expressed in geographic coordinates (XYZ coordinates), and I converted X (geographic north) and Y (geographic east) components to H (geomagnetic north) and D (geomagnetic east) components by rotating X and Y to the daily averaged magnetic declination.

3.2 Analysis Method

3.2.1 Procedure of Event selection

I use both automatic detection and visual inspection for selection of Pi2 events. In order to find Pi2-like wave packets, the original data from ASB were processed into time-series data of Pi2 wave energy *Uozumi et al.* (2000) that is an envelope of $\Delta H^2 + \Delta D^2$ (where

Station code	Geographic Latitude	Geographic Longitude	Geomagnetic Latitude	Geomagnetic Longitude	L	LT [hour] at 21:50 UT
		MAGDAS/CPMN				
HVD	48.01	91.67	43.51	164.05	1.90	3.9
PPI	42.98	131.73	36.27	203.74	1.56	6.6
PTK	52.94	158.25	46.17	226.02	2.12	8.4
ASB	43.46	142.17	36.43	213.39	1.54	7.3
AMA	28.17	129.33	21.11	200.88	1.15	6.5
DAW	-12.41	130.92	-21.91	202.81	1.16	6.5
TWV	-19.63	146.86	-28.73	220.30	1.30	7.6
		INTERMAGNET				
LZH	36.10	103.84	30.21	175.91	1.34	4.8
KAK	36.23	140.19	27.47	209.23	1.26	7.2
GUA	13.59	144.87	5.30	215.64	1.03	7.4
HON	21.32	202.00	21.67	269.52	1.16	11.3
AMS	-37.80	77.57	-49.10	138.34	2.33	3.0
LRM	-22.22	114.10	-33.57	185.18	1.44	5.4
TUC	32.17	249.27	39.84	314.19	1.78	14.5
BSL	30.35	270.37	41.50	339.93	1.70	15.6
SJG	18.11	293.85	28.79	9.83	1.30	17.4
CLF	48.02	2.27	43.67	79.68	1.91	22.0
TAM	22.79	5.53	9.22	78.37	1.03	22.2

TABLE 3.1: The geographic and geomagnetic location of each station.

ΔH and ΔD are bandpass-filtered H and D, respectively, in the period range from 40 to 150 sec). The use of both the H and D components allows us to evaluate the amplitude of Pi2 without depending on polarization changes. Isolated Pi2 wave packets are automatically detected by the following criteria:

(1) A peak in the wave enegy must exceed 0.0625 nT^2. The time of the peak is defined as the event time (T_{max}).

(2) The wave energy at T_{max} must be a maximum in the interval from 10 min before T_{max} to 10 min after T_{max}.

(3) To evaluate the amplitude of the background disturbance against that of Pi2s, I examine the wave energy in the interval of $T_{max} - 7$ min to $T_{max} - 2$ min. The averaged wave energy in this interval must be lower than 5% of the wave energy at the T_{max}.

The events including following types of background variations are removed by visual inspection: (1) Spike-like and step-like artificial noises (2) Step-like variation of SCs and SIs (3) Pc4-like continuous waves. However, it is still difficult to distinguish between Pi2 and Pc4 on the dayside in some cases. In such cases, I refer to the magnetic data from the nightside station (TAM for dawn side event events and TUC for dusk side events) and remove events that show no clear signature of Pi2 in nightside data.

3.2.2 Calculation of Phase Lag and Amplitude

I calculate the phase lag between two Pi2 waves using a cross phase analysis. A squared coherence (C_{xy}^2) and a phase lag (θ_{xy}) as functions of frequency f can be written as

$$C_{xy}(f)^2 \quad = \quad \frac{|S_{xy}(f)|^2}{S_{xx}(f)S_{yy}(f)} \tag{3.1}$$

$$\theta_{xy}(f) \quad = \quad \arctan \frac{\Im(S_{xy}(f))}{\Re(S_{xy}(f))} \tag{3.2}$$

where $S_{xx}(f)$ and $S_{yy}(f)$ are power spectra of each data and $S_{xy}(f)$ is a cross spectrum of two data. Before calculating spectra, I apply the Butterworth bandpass filter with a range of $10-300$ s to original data for reducing the background trend and the high-frequency noise. I calculate these spectra using Welch's modified periodogram method (*Welch*, 1967). The spectral components are calculated in the interval of 3 min before and 7 min after T_{max} (600 samples). The examined interval are divided into 5 segments of 500 samples (the length of overlap is 480 samples) and are applied. I apply a Hann window to each data segment and calculated modified periodograms using Fourier transform. Smoothed spectra are given by averaging the modified periodograms of 5 segments. The phase lag and squared coherence of Pi2 are determined at the dominant frequency (f_d), which is the maximum peak of $S_{xx}(f)$ (or $S_{yy}(f)$) in a range of frequencies between 6 and 22 mHz. Hence, the phase lag and squared coherence between two Pi2 waves are given as $\theta_{xy}(f_d)$ and $C_{xy}(f_d)^2$, respectively. The accuracy of phase lag is ensured only if coherence is substantially high. To reduce the error of the phase lag, I use $\theta_{xy}(f_d)$ whose $C_{xy}(f_d)^2$ is greater than 0.95 for the analysis.

An example of application of this cross phase analysis is shown in Figure 3.1 ($20:09:02-20:19:02$ UT 24 August 2012 event). One can see that the waveforms exhibit $180°$ phase lag from bandpass-filtered data with a range of $10-300$ s (a). The dominant frequency (f_d) shown by the vertical line is 12 mHz (b). $C_{xy}(f_d)^2$ is 0.99 (c), so $\theta_{xy}(f_d)$ is reliable. $\theta_{xy}(f_d)$ is -175.9° (d), which is consistent with the phase lag visually determined from the waveforms.
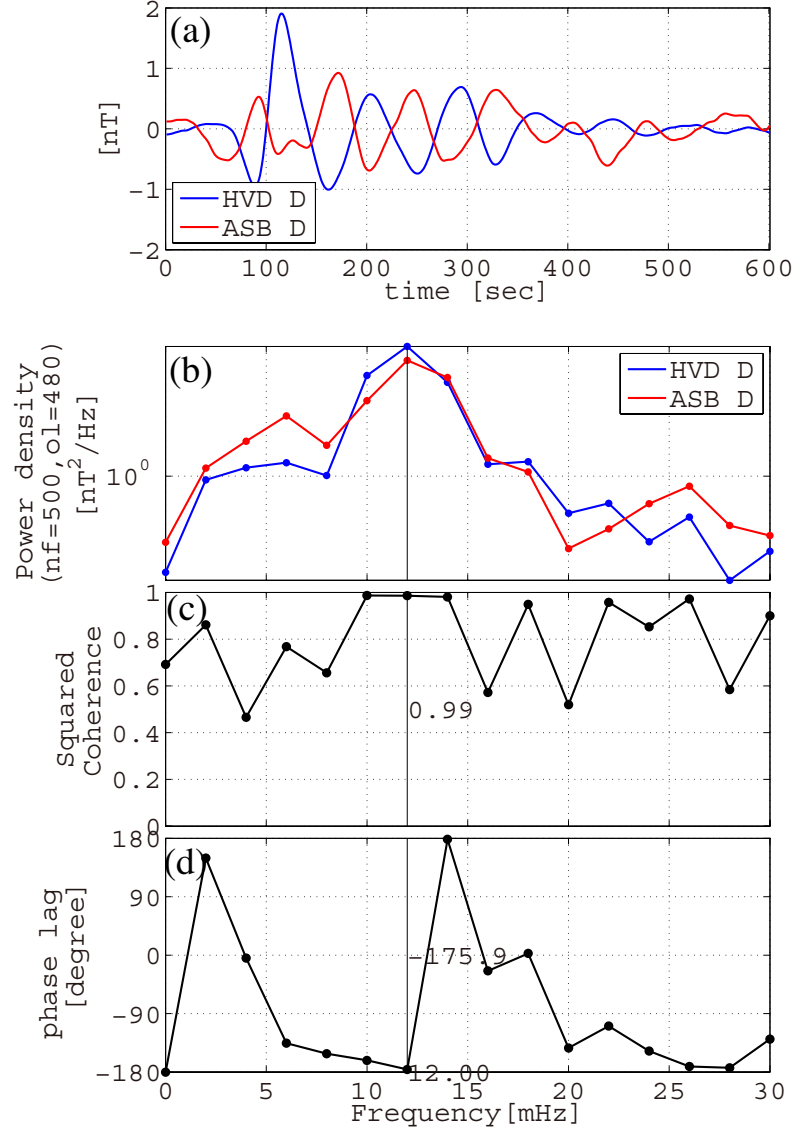
FIGURE 3.1: An example of application of the cross phase analysis ($20:09:02-20:19:02$ UT 24 August 2012 event). (a) Analyzed data that are bandpass-filtered with a period range of $10-300$ s. (b) Power spectrum density ($S_{xx}(f)$,$S_{yy}(f)$). (c) Squared coherence ($C_{xy}(f)$). (d) Phase lag ($\theta_{xy}(f)$).

3.2.3 Sunrise and Sunset Reference Times

In this thesis, sunrise and sunset are defined as the times when the center of the Sun appears above the horizon at dawn and dusk, respectively. The solar zenith angle at sunrise/sunset (χ_h) is $\pi/2$ at the ground level, but this exceeds $\pi/2$ at a higher altitude. The solar zenith angle at sunrise/sunset can be written as

$$\chi_h = \pi - \arcsin\left(\frac{R_E}{R_E + z}\right) \qquad \left(\frac{\pi}{2} \leq \chi_h \leq \pi\right) \tag{3.3}$$

where z and R_E are altitude and the radius of the solid Earth (see Figure 3.2 for the geometry). The sunrise time is the time when the solar zenith angle equals to χ_h and its time derivative is positive, while the sunset time is the time when the solar zenith angle equals to χ_h and its time derivative is negative. In this thesis, sunrise/sunset time is expressed by local time. I use the open source program in Air-sea toolbox for MATLAB (http://woodshole.er.usgs.gov/operations/sea-mat/air_sea-html/index.html) to calculate the solar zenith angle.
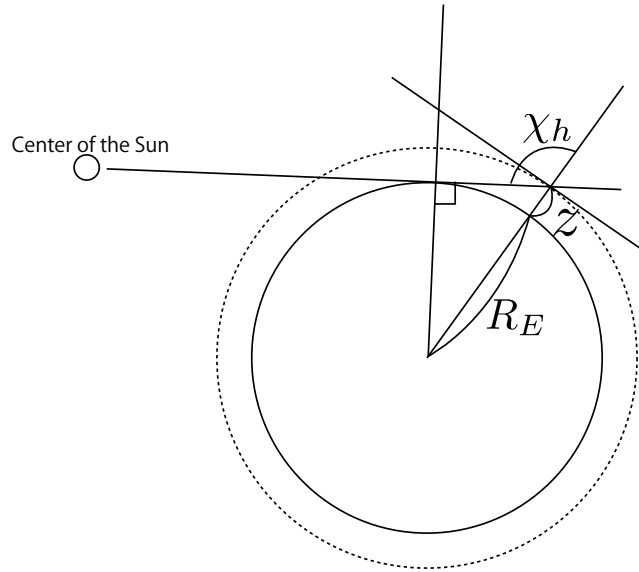
FIGURE 3.2: Geometry of center of the Sun, the Earth, sunrise/sunset location at the altitude of z. χ_h is the solar zenith angle at sunrise/sunset.

Figure 3.3 is the seasonal variations in the sunrise and sunset times at each location at 0, 100, and 200 km in altitude at PTK, ASB, and GUA. The sunrise time is earlier and the sunset time is delayed with increasing in altitude. For example, sunrise times at 100 and 200 km in altitude at ASB are ∼1 and ∼1.5 h, respectively, earlier than the sunrise time at 0 km. The difference in the sunrise/sunset time between summer and winter increases with increasing latitude. At 100 km in altitude the difference of the sunrise time at GUA is 1 h while the difference of the sunrise time at PTK is 5.2 h.

The terminator (or terminator line) is the line connecting the points of sunrise and sunset at a specific time. Figure 3.4 illustrates the terminators at the three different altitudes. On the ground (0 km in altitude), the area of the sunlit region equals to the area of the dark region. With increasing altitude, the sunlit region become larger than the dark region.
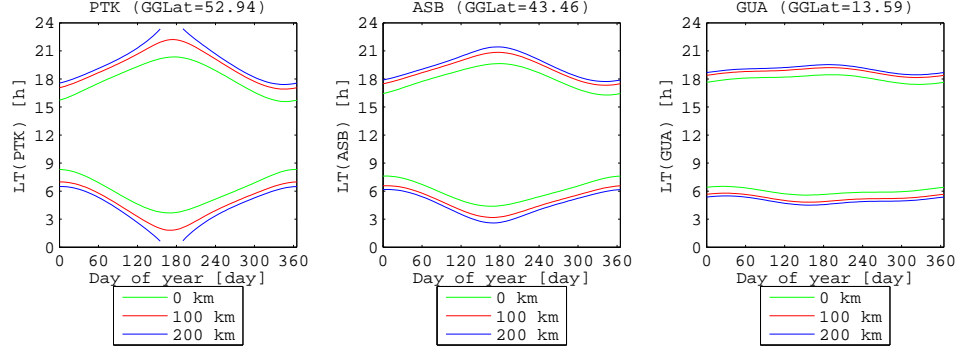
FIGURE 3.3: The seasonal variations in sunrise and sunset times at each location at 0, 100, and 200 km in altitude at PTK, ASB, and GUA.
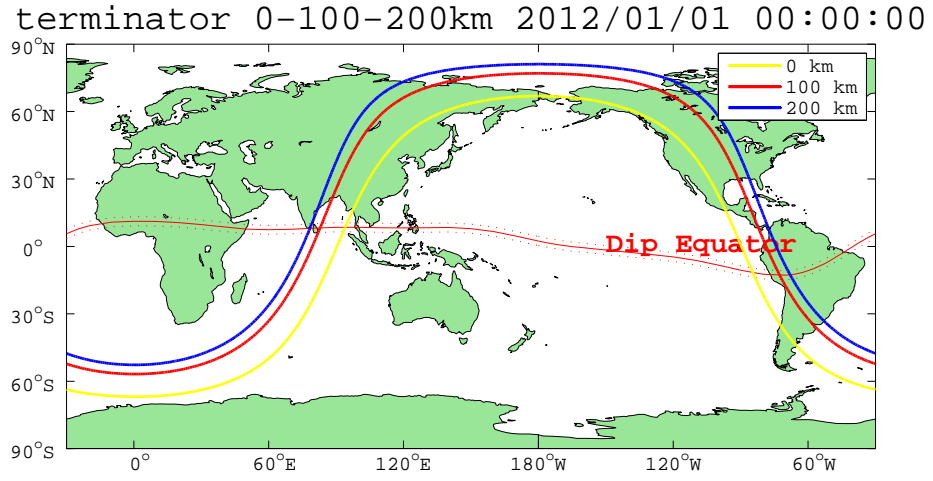
FIGURE 3.4: The terminators at the three different altitudes (0 ,100, and 200 km) on 1 January 2012 at 0000UT

If features of Pi2 are controlled by the location of the terminator, these will vary according to relative locations of stations to the terminator. I adopt sunrise/sunset reference times ($\Delta T_{sr}(\text{STN})/\Delta \text{T}_{\text{ss}}(\text{STN})$) [h] as measures of the relative location of a station STN (code of a station) to the dawn/dusk terminator. The sunrise/sunset reference times are defined here as the difference between the sunrise/sunset time in UT at each station ($T_{sr}(\text{STN})$ and $T_{ss}(\text{STN})$) at 100 km in altitude, where the highly conducting E region is located, and an event time (T_{Pi2}):

$$\Delta T_{sr}(\text{STN}) = T_{Pi2} - T_{sr}(\text{STN})$$
$$\Delta T_{ss}(\text{STN}) = T_{Pi2} - T_{ss}(\text{STN}) \tag{3.4}$$

For ΔT_{sr}(STN), negative values indicate that the station is in darkness while positive values indicate that the station is in sunlight. For ΔT_{ss}(STN), negative values indicate that the station is in sunlight while positive values indicate that the station is in darkness.

3.3 Case Studies

3.3.1 16 September 2011 Event

In this section, I investigate a Pi2 event, which occurred at 21:50 UT on 16 September 2011. Figure 3.5 is the map of the stations and the terminators at 0, 100 and 200 km in altitude at 21:50 UT. The event is associated with the onset of a small substorm with the AL index reaching a minimum value of -120 nT at 22:00 UT as shown in Figure 3.6a. Figure 3.6b and c show H and D component magnetic variations, respectively, at the stations on the dawn side and the HON station near noon. The H component oscillations are nearly in phase, which is consistent with results of previous reports (e.g., *Sutcliffe and Yumoto*, 1991; *Nosé et al.*, 2003, 2006). The H amplitude in darkness (HVD, LZH, and AMS) is larger than the H amplitude in sunlight, although the amplitude near noon (HON) is larger than the stations in the sunlit morning (e.g., PPI and ASB). On the other hand, the D component oscillations show different phases and amplitudes from the H component. The oscillations in the D component show a phase reversal around the dawn terminator. The phase reversal occurred between LZH and AMA in the Northern Hemisphere and between LRM and DAW in the Southern Hemisphere. In both darkness and sunlight, D oscillations in the Northern Hemisphere are in antiphase with D oscillations in the Southern Hemisphere. The amplitude of the D component was greater than that of the H component except for HON, which was located near noon.

I also investigate Pi2s on the dusk side for this event, when the dusk terminator was located over the Atlantic. Figure 3.7 shows H and D component magnetic variations from northern Hemisphere stations on the dusk side and the HVD station in the postmidnight sector as a reference station. Unlike the dawn side, the amplitude of the H component is larger than the D component. The D component amplitude at the SJG station, the nearest station from the dusk terminator, is relatively small. The H component oscillations are nearly in phase as I found in the dawn side magnetic data. The oscillations in
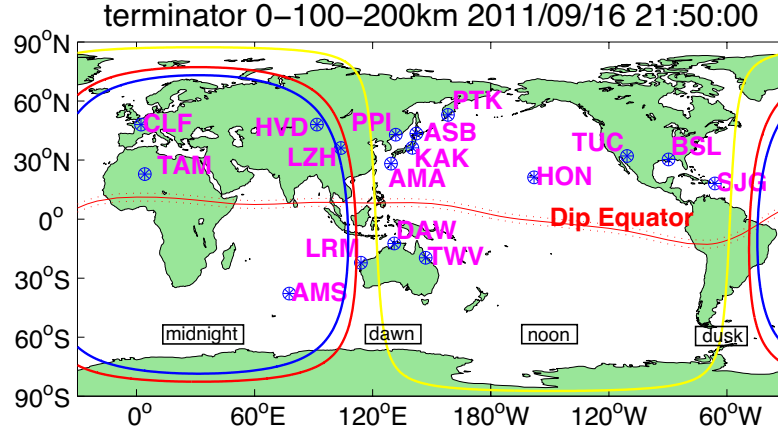
FIGURE 3.5: Map of stations and the terminator at 21:50 UT on 16 September 2011. The solid curves are the locations of the terminator at three different altitudes: 0 km (yellow), 100 km (red) and 200 km (blue).

the D component show a phase reversal between the BSL and CLF stations. This phase reversal should be distinguished from the D component phase reversal around midnight as reported by previous studies (*Lester et al.*, 1983; *Li et al.*, 1998); in this event the midnight phase reversal occurred between CLF in the premidnight sector and HVD in the postnidnight sector.

3.3.1.1   Other Examples

Figure 3.8 shows 12 typical events that exhibit D component phase reversal near the dawn terminator. The figure includes AL index and H and D bandpass-filtered magnetic fields at HVD on the nightside and ASB on the dayside for each event. Although D oscillations show small phase shift from a 180° phase lag, the oscillations are in nearly antiphase. H oscillations have relatively a small phase lag compared to the D component, or the oscillation is very small and ambiguous. Events b, d, e, f, i, and k show a start of decreasing in AL index at the onset of Pi2 pulsations, while events a, c, g, h, j, and m do not show this evidence. This indicates that the phase reversal near the dawn terminator is also observed with psedobreakups.

Figure 3.9 show 8 typical events that exhibit the D component phase reversal near the dusk terminator in the same format as Figure 3.8. Compared to dawn side events, it is difficult to find clear examples since the amplitude of the D component at HVD on the dayside tends to be very small. H oscillations are synchronized with each other with
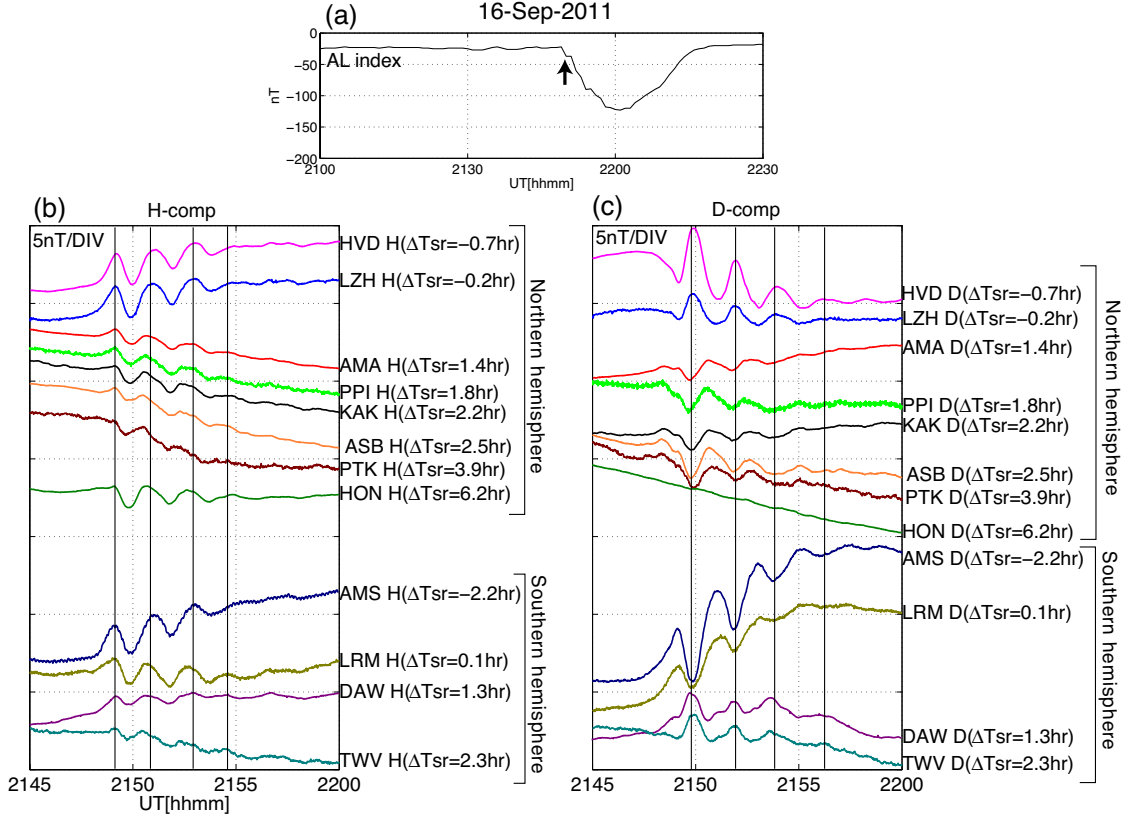
FIGURE 3.6: (a) *AL* index, the (b) *H*-component and (c) *D*-component magnetic variations around the dawn terminator at 21:50 UT on 16 September 2011. The arrow in (a) indicates the timing of the Pi2 event. ΔTsr is the time difference between the sunrise time defined at 100 km in altitude and the event time, where negative values indicate that a station was in darkness while positive values indicate that a station was in sunlight.

a small phase lag (within $\pm 30°$) for each event. Although D oscillations show small phase shift from a $180°$ phase lag, the oscillations are in nearly antiphase. At ASB on the nightside, the D amplitude is comparable to the H amplitude or larger than the H amplitude. On the other hand, the D amplitude at HVD is smaller than the H amplitude. Events c, d, and e show a start of decreasing in AL index at the onset of Pi2 pulsations, while events a, b, f, g, and h do not show this evidence. This indicates that the phase reversal near the dusk terminator is observed regardless of a development of a westward electrojet.
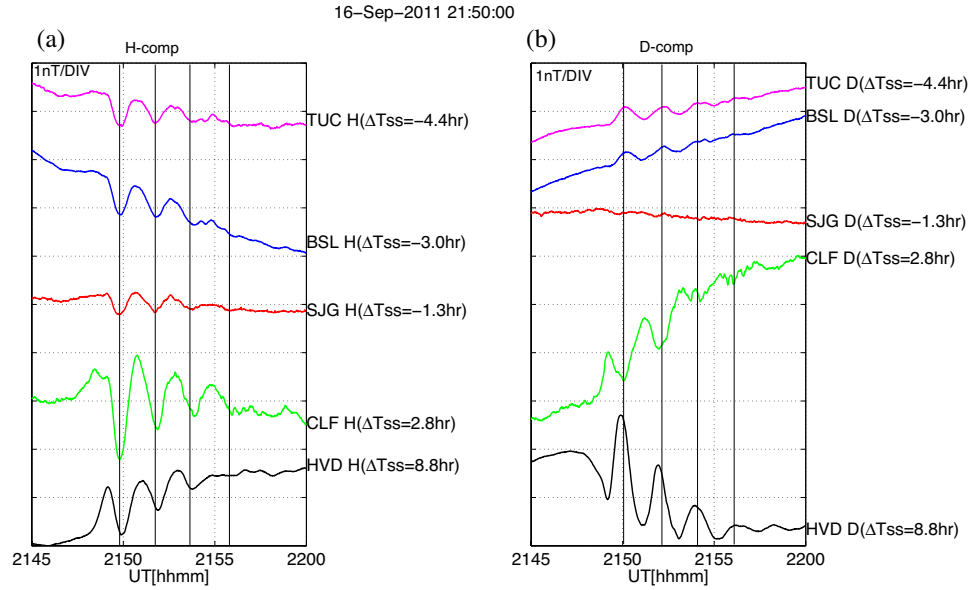
FIGURE 3.7: The (a) H component and (b) D component magnetic variations on the dusk side around 21:50 UT on 16 September 2011. ΔTss is the time difference between the sunset time defined at 100 km in altitude and the event time, where negative values indicate that a station was in sunlight while positive values indicate that a station was in darkness.

3.4 Statistical Studies

In this statistical analysis I use the five stations separated in latitude along the same meridian (PTK, ASB, KAK, CBI, and GUA). The HVD station is used as a reference station for examining the change of phase.

3.4.1 Pi2 around the Dawn Terminator

Pi2 events are selected during the period from 1 November 2011 to 31 October 2012, when the quantity of data available is large, between 01:00 and 09:00 LT at ASB. I selected a total of 213 Pi2 events from ASB data in this interval using the procedure presented in section 3.1.

Figure 3.10 is the LT distribution of the selected events. As is well known, Pi2 pulsations are more detectable on nightside than on dayside, indicating that the source of Pi2 is located near the midnight. Figure 3.11 is the seasonal distribution of the selected events. A peak of occurrence appears in the spring season and August.
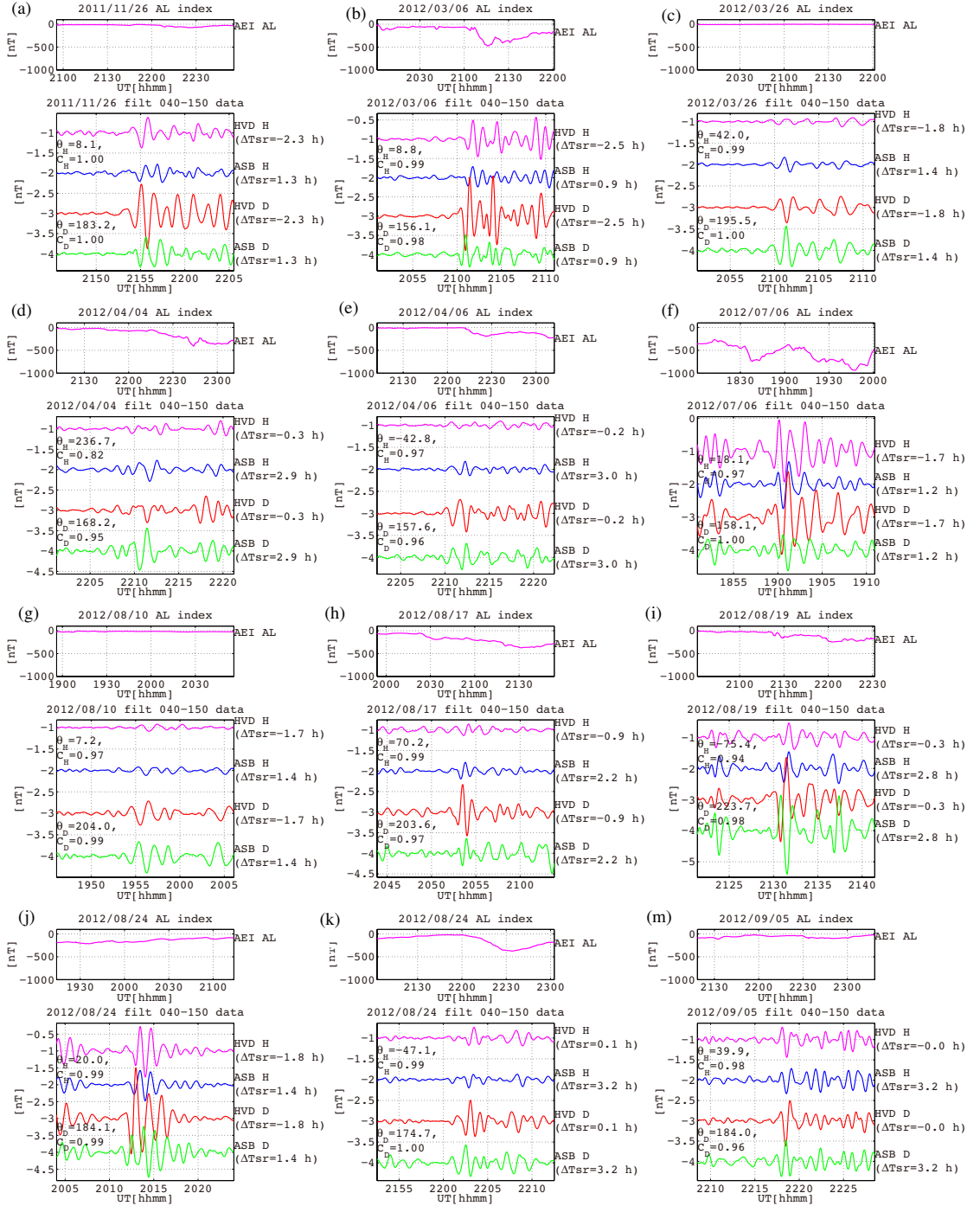
FIGURE 3.8: *AL* index and *H* and *D* component bandpass-filtered magnetic fields at HVD and ASB near the dawn terminator for 12 events. $\theta_{H,D}$ and $C_{H,D}$ are phase lag and squared coherence, respectively, where subscripts show a vector component.
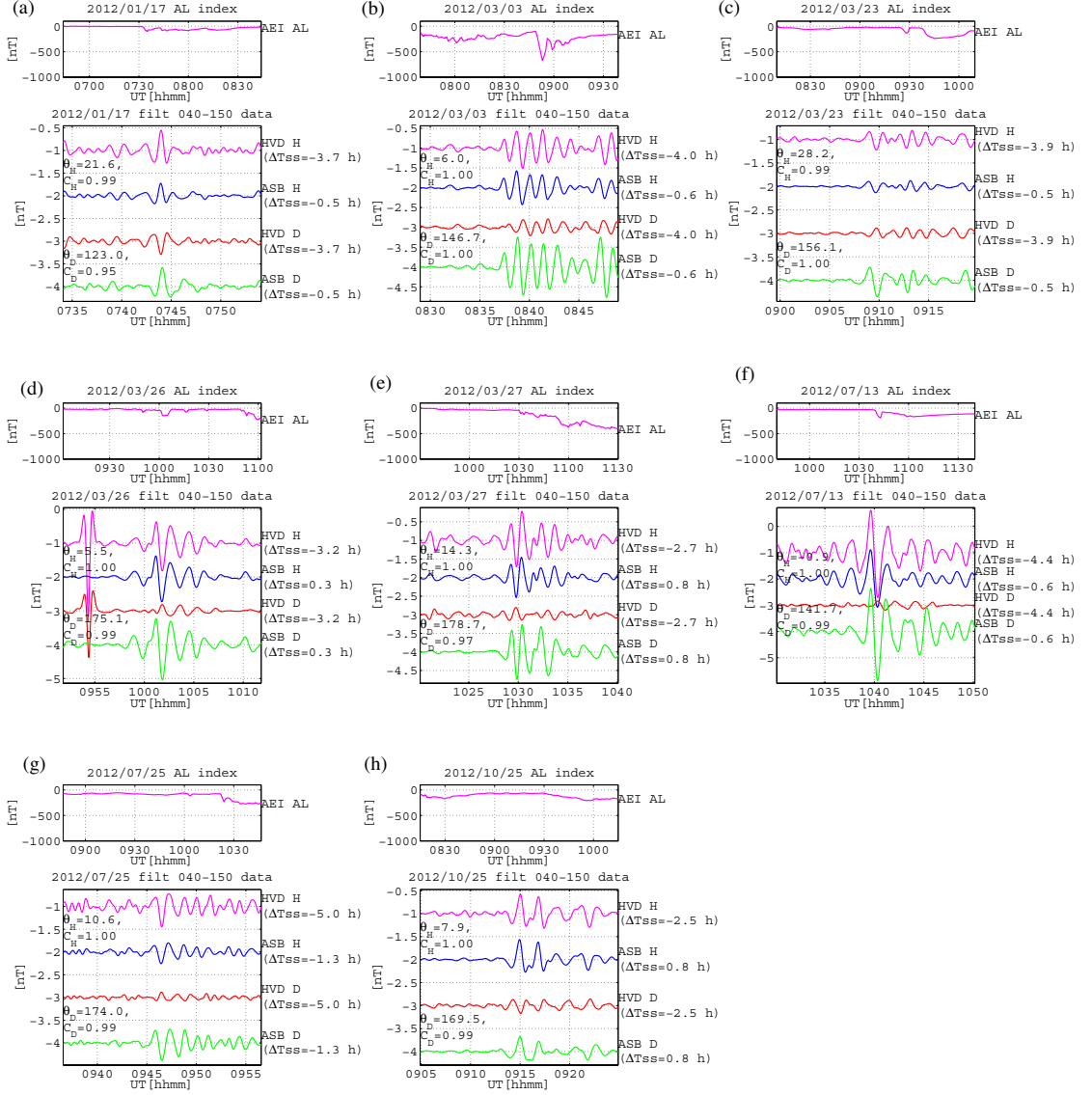
FIGURE 3.9: *AL* index and *H* and *D* component bandpass-filtered magnetic fields at HVD and ASB near the dusk terminator for 8 events in the same format as Figure 3.8

Figure 3.12 presents the LT and ΔT_{sr} dependences of the phase lag of the H component between HVD and the five examined stations. Positive values indicate that the phase of reference data (HVD H) is delayed with respect to the examined data. Red and cyan vertical lines show sunrise times at the summer solstice and the winter solstice, respectively. It is clear that most phase lags are near 0° for all LT and ΔT_{sr} except for PTK. The phase lag of PTK H is more scattered, but the phase of HVD tends to be delayed from that of PTK.

Figure 3.13 shows the LT and ΔT_{sr} dependences of the phase lag of the D component between HVD and the five examined stations. The phase lags at ASB, KAK, and
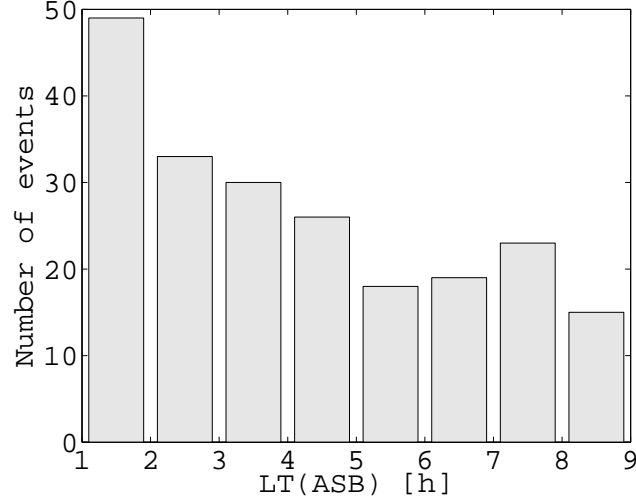
FIGURE 3.10: Event occurrence against LT for 213 dawn side Pi2 events.
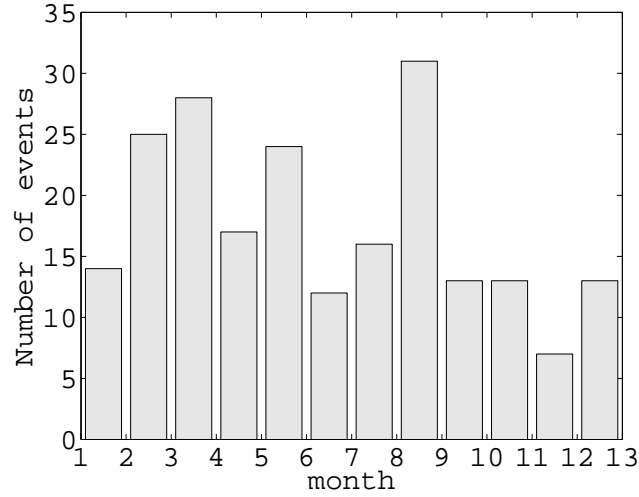
FIGURE 3.11: Event occurrence against month for 213 dawn side Pi2 events.

CBI show a clear jump from $\sim 0°$ to $\sim 180°$ near $\Delta T_{sr} = 0.5 - 1$ while there is no clear systematic change of the phase with LT. These results indicate that the phase reversal of the D component is related to the location of the dawn terminator rather than to the local time. Except for PTK, the phase lags for $\Delta T_{sr} \leq -1$ tend to be more scattered, and this may be attributable to a smearing of the phase reversal around the midnight. The LT and ΔT_{sr} dependences at GUA is similar because of the small yearly variation of sunrise time. Although the the phase lag for $\Delta T_{sr}(\text{GUA}) \leq 1$ tends to be scattered, this is near $180°$ for $\Delta T_{sr}(\text{GUA}) \geq 1$. The phase lag at PTK is near $180°$ for $\Delta T_{sr}(\text{PTK}) \leq -1$. Since the local time at PTK for $\Delta T_{sr}(\text{PTK}) \leq -1$ is near the midnight in the summer season, these antiphase relations may be caused by the midnight
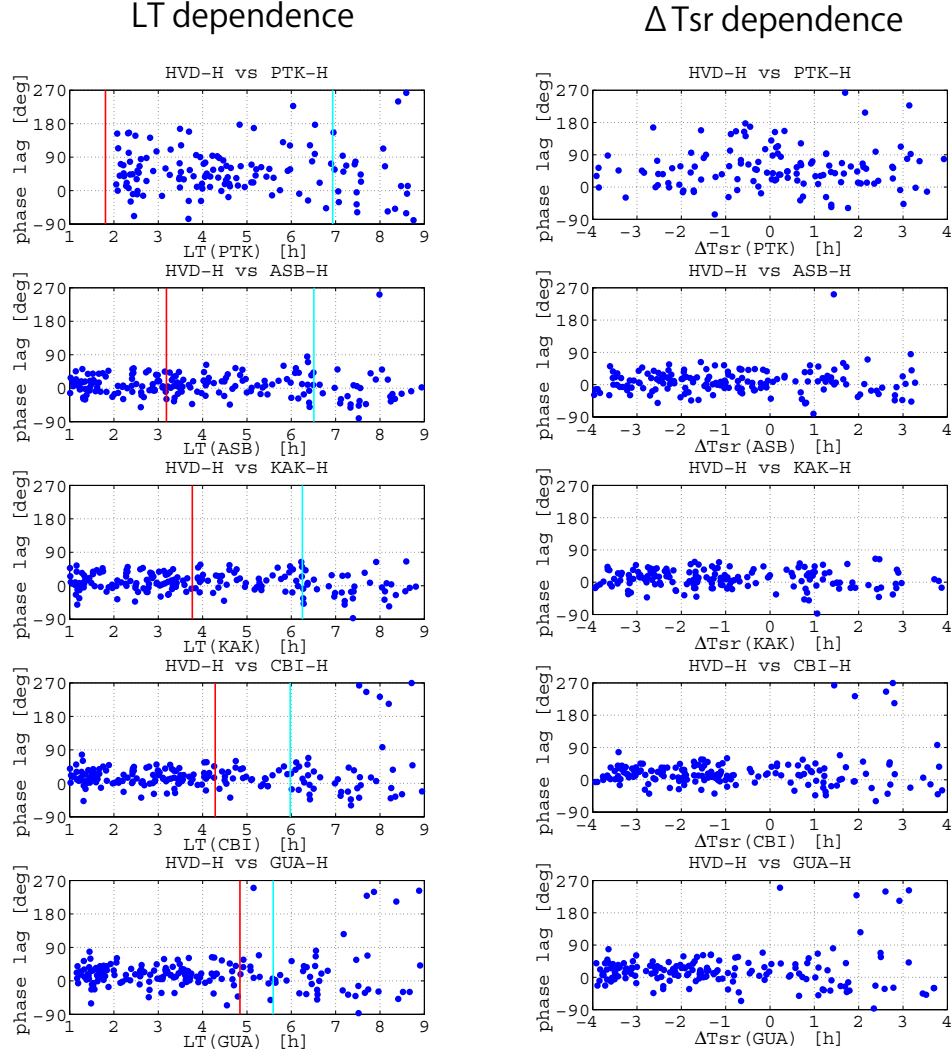
FIGURE 3.12: The ΔT_{sr} and LT dependences of the phase lag of the H component between HVD and the five examined stations. Positive values indicate that phase of examined data is delayed by reference data. Red and cyan vertical lines show sunrise times at the summer solstice and the winter solstice, respectively.

phase reversal.

I statistically examine the events when the phase reversal region ($0.5 \leq \Delta T_{sr} \leq 1$) was located between HVD and each examined station. I selected events that satisfy $\Delta T_{sr}(\text{HVD}) \leq 0$ and $1 \leq \Delta T_{sr}(\text{ESTN})$, where ESTN is the station code of examined stations. The geometry of the stations and the terminator in this situation is shown in Figure 3.14. Figure 3.15 is the distribution of the phase lag of the D component between HVD and the five examined stations. The phase lags are clearly distributed around 180° (antiphase relation). Table 3.2 is the parentage of antiphase relation events. I use two criteria of the antiphase relation, $180 \pm 45°$ and $180 \pm 90°$. The percentage of antiphase
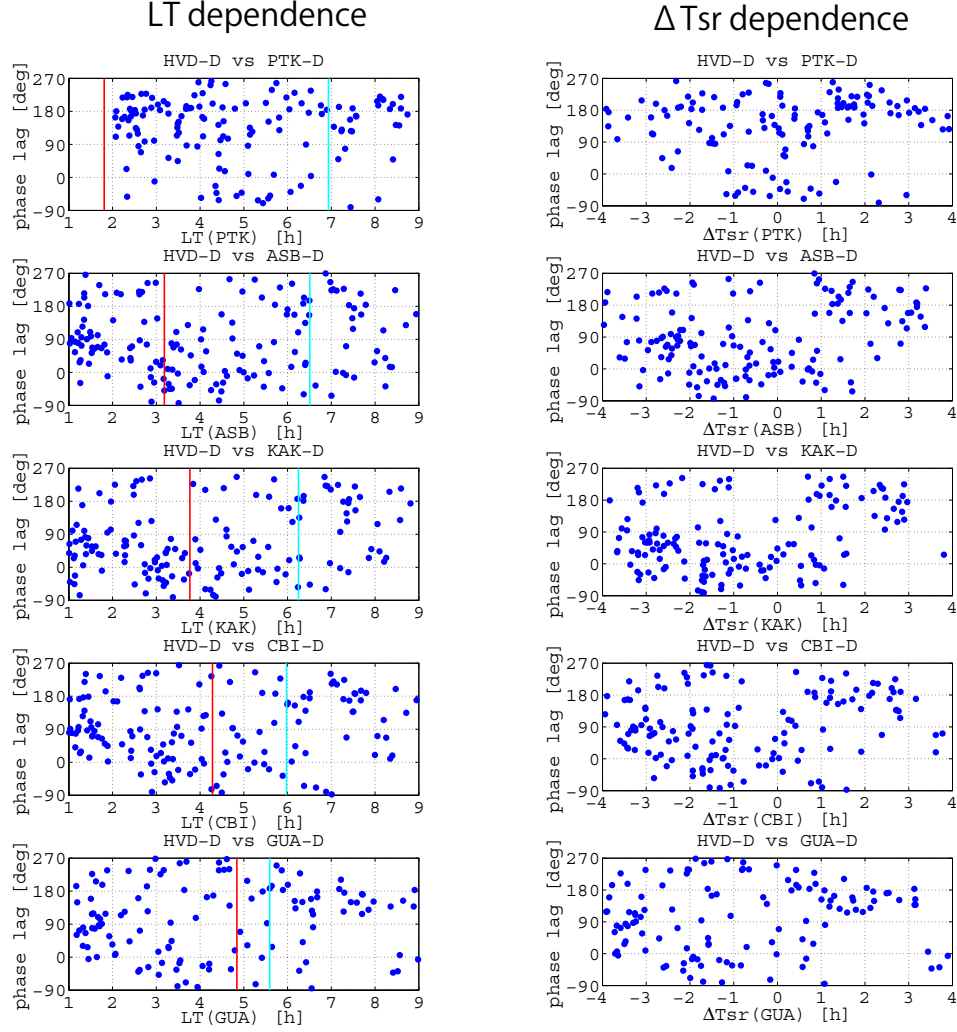
FIGURE 3.13: The ΔT_{sr} and LT dependences of the phase lag of the D component between HVD and the five examined stations in the same format as Figure 3.12.

events is up to 58% for $180 \pm 45°$ and 81% for $180 \pm 90°$, indicating that the D phase reversal around the dawn terminator is a general feature.

I analyze amplitude characteristics of Pi2 around the dawn terminator. The amplitude is simply determined by a maximum perturbation of the bandpass-filtered data with a period of $40-150$ s. Figure 3.16 shows the LT and ΔT_{sr} dependences of H and D amplitudes and the D-to-H amplitude ratio. The H amplitude at ASB, KAK, and CBI tends to decrease toward noon, although the H amplitude at GUA increases toward noon on the dayside. The variation of the H amplitude at PTK differs from others; a clear minimum appears at $LT = 3-4$. The D amplitudes increase with latitude on both nightside and dayside. Although Pi2s are believed to have a larger amplitude on the nightside than on the dayside, the D amplitude on the dawn side increases toward noon.
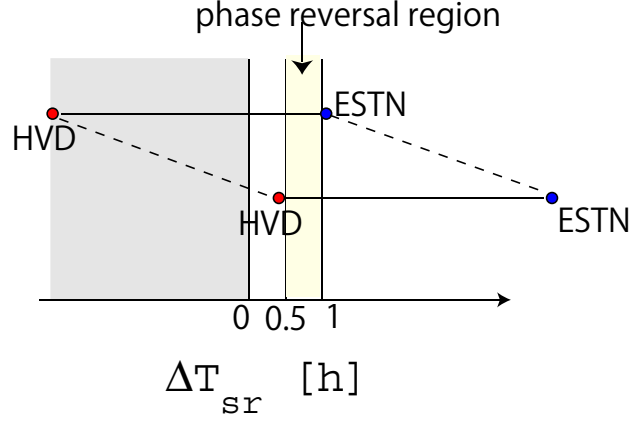
FIGURE 3.14: Relative locations of HVD and a examined station (ESTN) to the dawn terminator when $\Delta T_{sr}(\text{HVD}) \leq 0.5$ and $1 \leq \Delta T_{sr}(\text{ESTN})$ are satisfied.

The D-to-H amplitude ratio starts to increase at LT $= 5$ and $\Delta T_{sr} = 0$, although the increase with ΔT_{sr} is more drastic than with LT except for PTK. The D-to-H amplitude ratio of $1 \leq \Delta T_{sr} \leq 2$ at ASB is 2.2 while that of $-2 \leq \Delta T_{sr} \leq -1$ is 0.9, indicating that dawn side Pi2 in sunlight were more polarized in the azimuthal direction than in darkness.

station	$180 \pm 45°$	$180 \pm 90°$
PTK	68%	88%
ASB	58%	81%
KAK	63%	83%
CBI	68%	81%
GUA	69%	92%

TABLE 3.2: The percentage of antiphase events when the dawn phase reversal region located between HVD and each examined station.

3.4.2 Pi2 around the Dusk Terminator

Pi2 events are selected during the same period as the previous analysis between 13:00 and 21:00 LT at ASB. I selected a total of 167 Pi2 events from ASB data in this interval using the procedure presented in section 3.1.

Figure 3.17 and Figure 3.18 are event occurrences against LT and month, respectively, for 167 dusk side Pi2 events. The event occurrence increases towards midnight. The peaks in occurrence in spring and fall are probably due to seasonal variation of the magnetic activity (e.g., *Ellis*, 1899; *Russell and McPherron*, 1973).
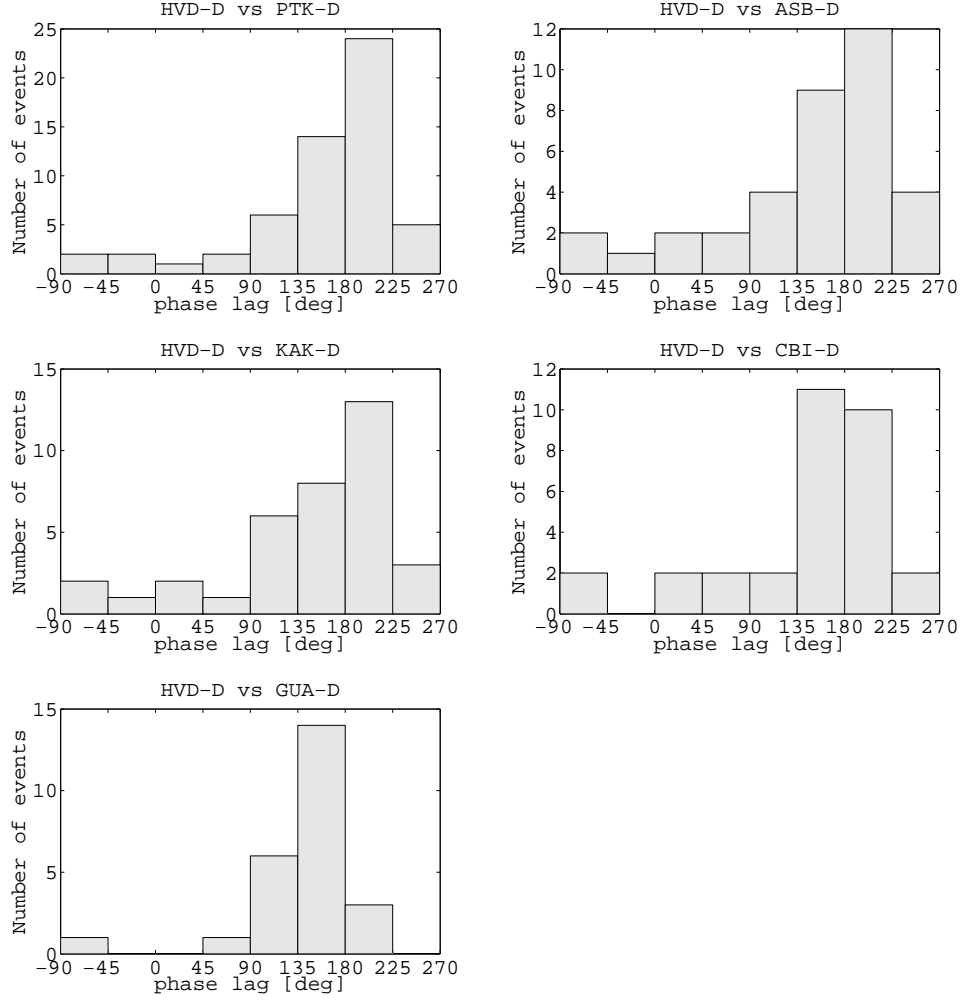
FIGURE 3.15: The distributions of the phase lags of the D component between HVD and the five examined stations when the phase reversal region near the dawn terminator located between HVD and each examined station.

Figure 3.19 illustrates the LT and ΔT_{ss} dependences of the phase lag of the H component between HVD and the five examined stations. It is clear that most phase lags are near $0°$ for all LT and ΔT_{ss} and for all stations except for PTK. The phase lag of PTK H is more scattered, but the phase of HVD tends to be delayed from that of PTK.

Figure 3.20 is LT and ΔT_{ss} dependences of phase lag of the D component between HVD and the five examined stations. There is no clear systematic change of the phase with LT for all stations. It seems that the phase lags at ASB, KAK, and CBI show a jump from $\sim 0°$ to $\sim 180°$ near $\Delta T_{ss} = -2 \sim -1$, although these are not so clear compared with the phase jump on the dawn side. The phase lag after the reversal tends to gradually decrease to $\sim 45°$ with ΔT_{ss}. For PTK and GUA, there is no clear systematic change in the phase.
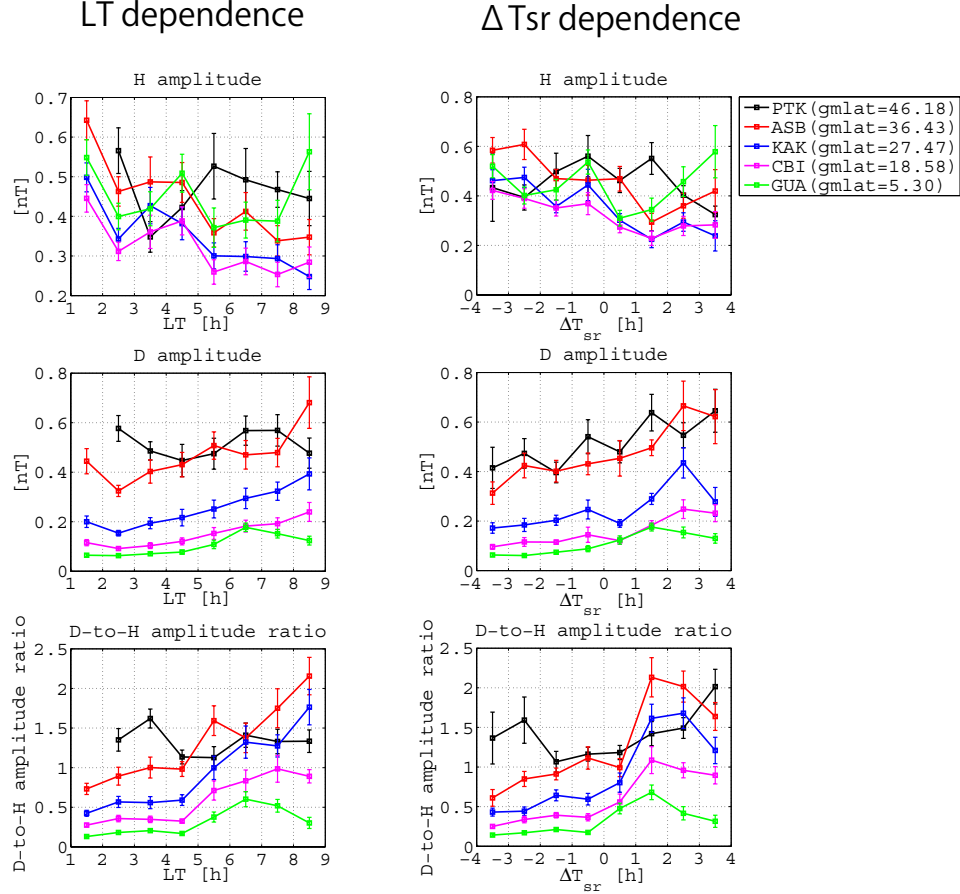
FIGURE 3.16: LT dependences of (a) H amplitude, (c) D amplitude, and (e) D-to-H amplitude ratio and ΔT_{sr} dependences of (b) H amplitude, (d) D amplitude, and (f) D-to-H amplitude ratio. Error bars denote the standard errors of the mean.

I statistically examine the event when the phase reversal region $(-2 \leq \Delta T_{ss} \leq -1)$ was located between the HVD and each examined station in a same manner as Figure 3.14. Figure 3.21 is the distribution of the phase lag of the D component between HVD and the five examined stations. Table 3.3 is percentage of antiphase relation event. The percentage of antiphase events is up to 31% for $180 \pm 45°$ and 68% for $180 \pm 90°$. The phase lags tends to be distributed around $180°$ rather than 0 although the tendency is weaker than the case of the dawn side.

Figure 3.22 shows the LT and ΔT_{ss} dependences of H and D amplitudes and D-to-H amplitude ratio. The H amplitude is largest at PTK and its variation differs from other stations. The D amplitude increases with latitude on both nightside and dayside and starts to increase at LT = 17 toward midnight. The D-to-H amplitude ratio except for PTK increases with latitude. Peaks of D-to-H amplitude ratio occur at LT = 19 and
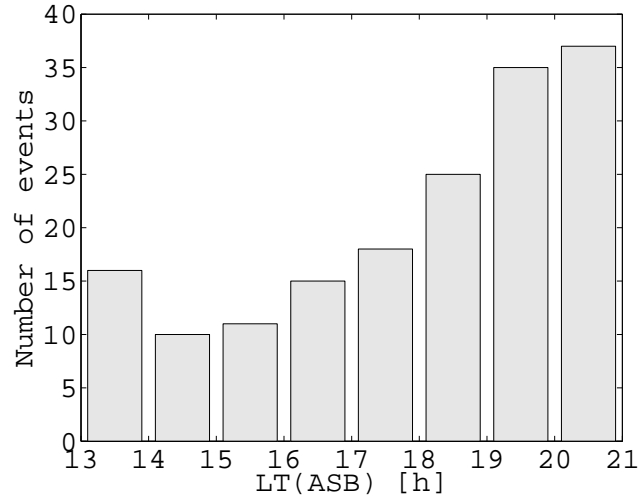
FIGURE 3.17: Event occurrence against LT for 167 dusk side Pi2 events.
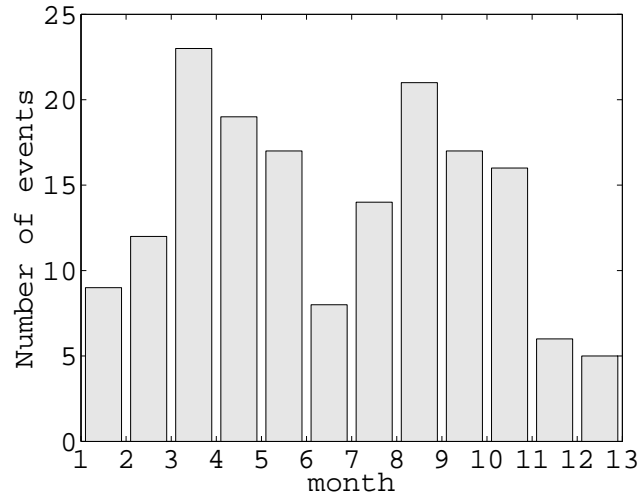
FIGURE 3.18: Event occurrence against month for 167 dusk side Pi2 events.

$\Delta T_{ss} = 0$. This differs from the D-to-H amplitude ratio on the dawn side, whose peak occurs at few hours toward noon from the terminator.

3.5 Interpretation of Observation Results

I found the D component phase reversals near the dawn and dusk terminators, which are different from the phase reversal around midnight reported by previous studies. The occurrence of phase reversal related to the dawn terminator was substantially high, while that of the phase reversal related to the dusk terminator was rather lower. These phase reversals are not expected by the existing model of low-to-middle latitude Pi2, such
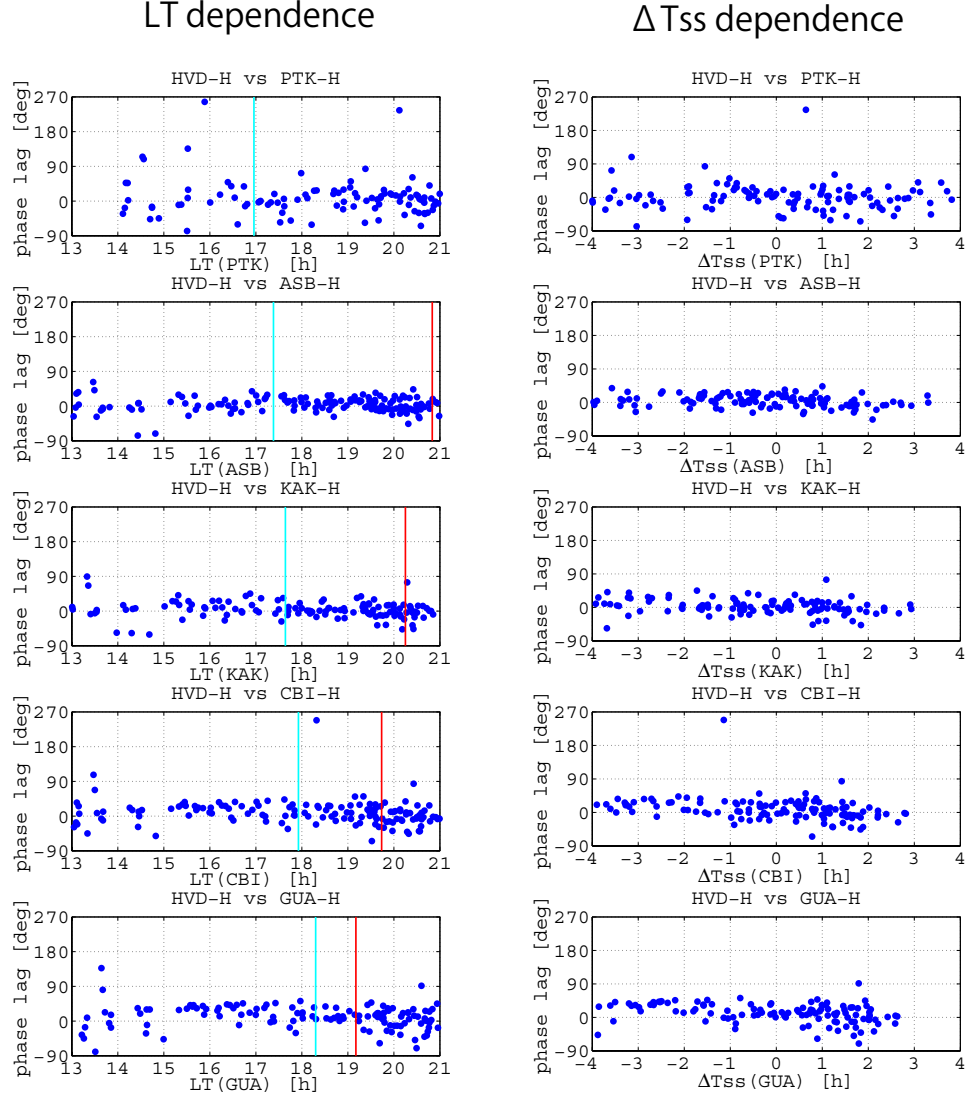
FIGURE 3.19: LT and ΔT_{ss} dependences of phase lag of the H component between HVD and the five examined stations. Positive values indicate that phase of examined data is delayed by the reference data. The red and cyan vertical lines show sunset times at the summer solstice and the winter solstice, respectively.

as the plasmaspheric resonance (e.g., *Allan et al.*, 1996), the direct driven fast wave (e.g., *Kepko and Kivelson*, 1999), and the SCW oscillation (e.g., *Lester et al.*, 1983). If the plasmaspheric resonance is applied, the small phase difference of H oscillations over entire local times indicates that the dominant m number is nearly zero. While the cavity mode with $m = 0$ is decoupled from azimuthal oscillations (D oscillations), cavity modes with $m \geq 1$ have both H and D oscillations and their nodes. The uniform phase structure of the cavity mode with $m \sim 0$ can still be maintained if the amplitude of the $m \sim 0$ mode is larger than the amplitude of $m \geq 1$ modes. However, there is no reason why a node of D oscillations should always be located near the terminators. The direct
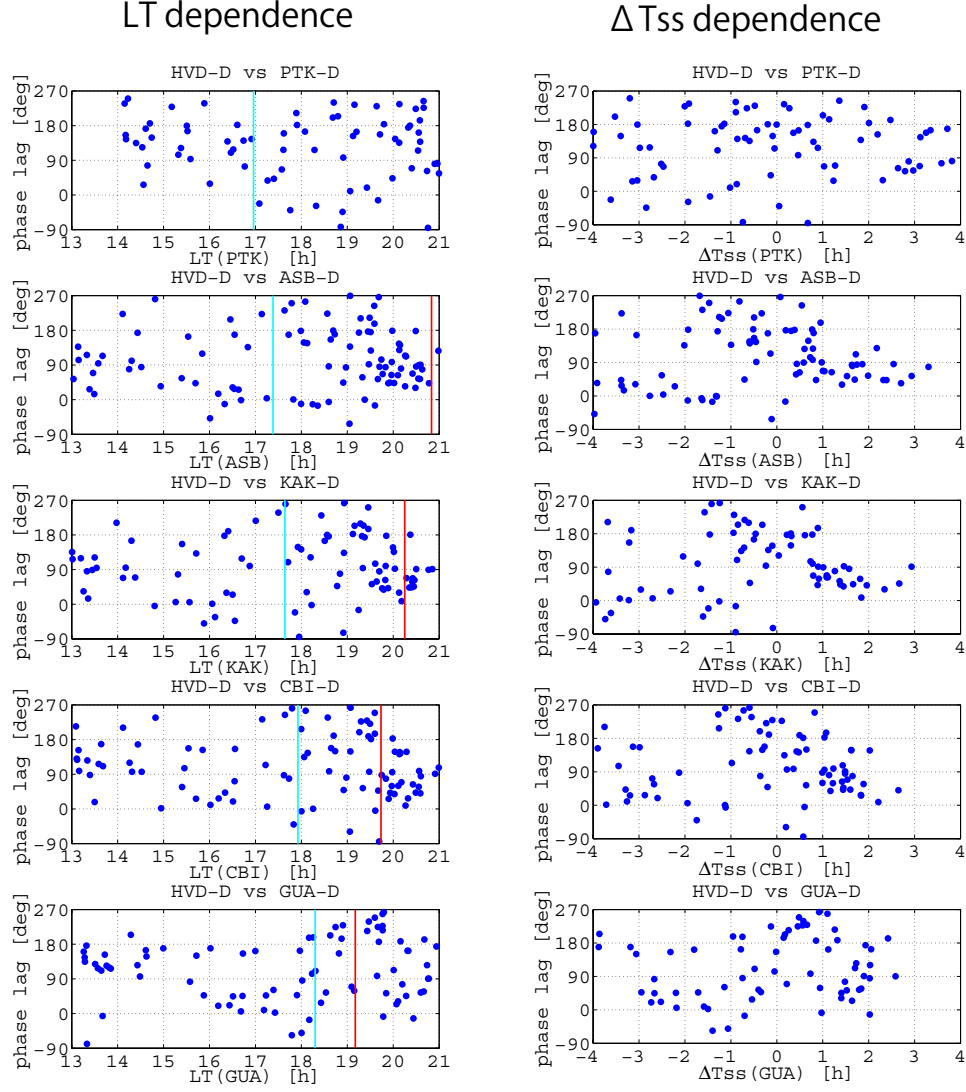
FIGURE 3.20: LT and ΔT_{ss} dependences of the phase lag of the D component between HVD and the five examined stations. Positive values indicate that the phase of examined data is delayed by the reference data HVD D. The red and cyan vertical lines show sunset times at the summer solstice and the winter solstice, respectively.

driven fast mode wave does not have nodal structures, the D phase reversal does not occur except the meridian of the source region. The SCW oscillations cause only a D phase reversal at the central meridian of the SCW.

The D-to-H amplitude ratio starts to increase with sunrise and reach a peak at $1-3$ h after sunrise (or after a phase reversal), which is consistent with the case study by *Saka et al.* (1980). The D-to-H amplitude ratio at ASB exceeded 2, which means morning side Pi2 were polarized in the azimuthal direction. This polarization is different from nightside low-latitude Pi2 that tends to be polarized in the north-south direction (*Takahashi and Liou*, 2004). The fast mode wave is not consistent with large D-to-H
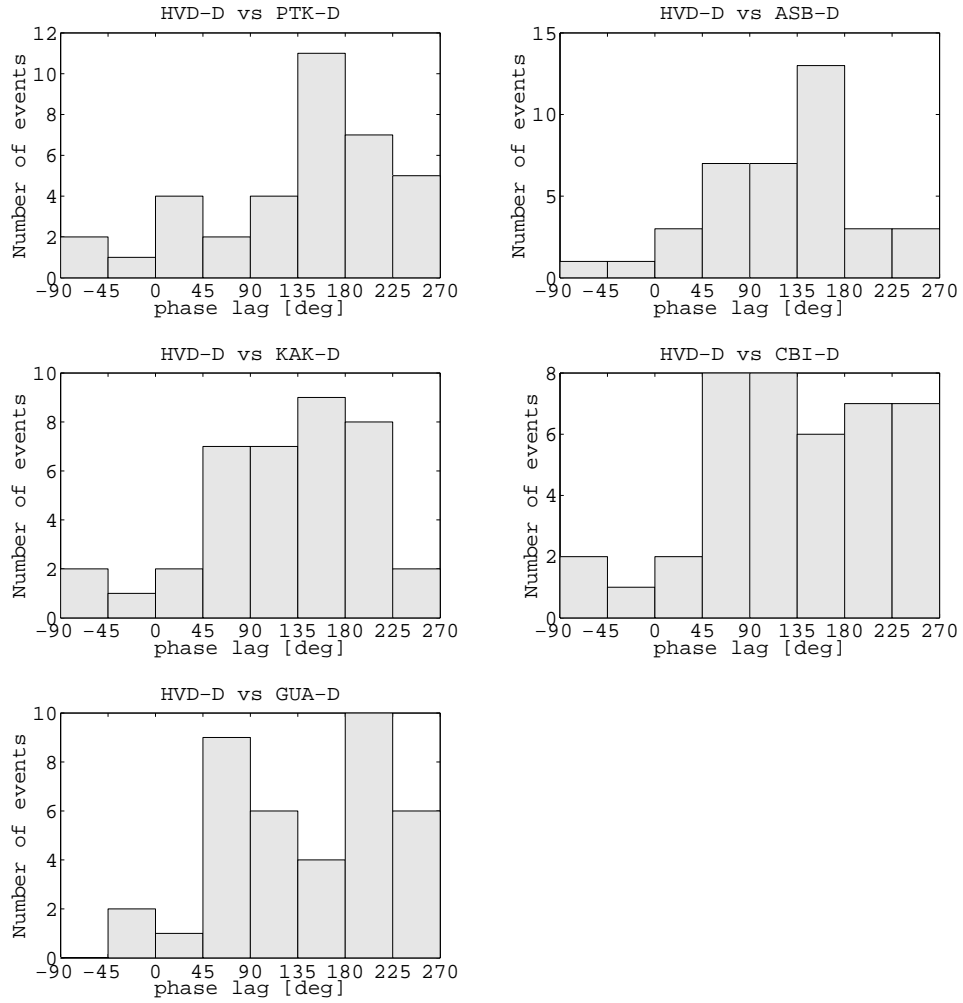
FIGURE 3.21: The distributions of the phase lags of the D component between HVD and the five examined stations when the phase reversal region near the dusk terminator located between HVD and each examined station.

amplitude ratio because the wave produces H magnetic variations but little produces D magnetic variations. Fast mode waves can be converted to Alfvén waves if the radial component of polarization currents and the gradient of the Alfvén velocity are significant (*Itonaga and Yoshikawa*, 1996). However, since the polarization current of the fast mode

station	180 ± 45	180 ± 90
PTK	50%	75%
ASB	42%	68%
KAK	45%	68%
CBI	32%	68%
GUA	37%	68%

TABLE 3.3: The percentage of antiphase events when the phase dusk reversal region ($-2 \leq \Delta T_{ss} \leq -1$) located between HVD and each examined station.
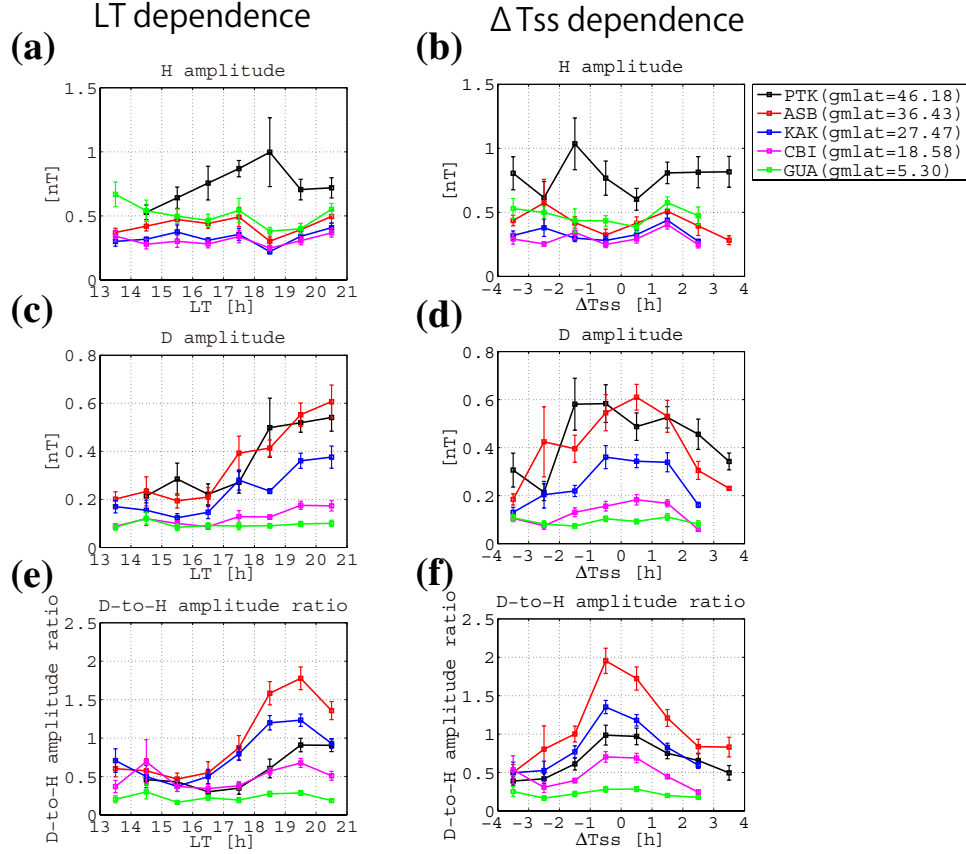
FIGURE 3.22: LT dependences of (a) H amplitude, (c) D amplitude, and (e) D-to-H amplitude ratio and ΔT_{ss} dependences of (b) H amplitude, (d) D amplitude, and (f) D-to-H amplitude ratio.

wave flows in the azimuthal direction in the inner plasmasphere, the mode conversion is not significant in the inner plasmasphere (*Itonaga and Yumoto*, 1998). The D-to-H amplitude ratio around the dusk terminator starts to increase $1-2$ h before sunset and peaks at near sunset. Contrary to the dawn side, the amplitude ratio is larger on the antisunward side from the phase reversal meridian. Differences between dawn and dusk Pi2 will be discussed in chapter 6 with results in chapters 4 and 5.

The D component phase reversals may be explained by considering the configuration of oscillatory FACs and ionospheric currents. I suggest that the meridional component of ionospheric currents is a possible source of the D component geomagnetic perturbation on the sunlit side. If a meridional current on the dark side flows in the opposite direction to the meridional current on the sunlit side, an opposite magnetic perturbation can be produced on the dark side. However, this magnetic perturbation would not be significant because currents are weak in the dark low-latitude ionosphere, where the conductivity is

low. Alternatively, I consider that the oscillatory FAC in the postmidnight sector generates azimuthal Pi2 oscillations in darkness. Figure 3.23 is the schematic configuration of FACs, ionospheric closure currents produced by these FACs and magnetic fluctuations on the ground produced by these currents. The configuration of currents is similar to the current systems for SCs, DP2 or Pc5 pulsations (*Araki*, 1994; *Kikuchi et al.*, 1996; *Motoba et al.*, 2002). The FAC carries current perturbations related to Pi2s from the magnetosphere to the nightside high-latitude ionosphere. The ionospheric current provided by the FAC may be connected to the meridional current near the terminator via the zonal current flowing at the auroral latitude where the conductivity is enhanced by auroral precipitation. In the northern hemisphere, when the perturbation component of the postmidnight FAC flows downward, the meridional current flows southward. The perturbation component of the FAC produces westward magnetic perturbations in the postmidnight sector. On the other hand, the Pi2-related component of the southward meridional current produces eastward magnetic perturbations on the ground. That is, westward and eastward ground magnetic perturbations are produced on the dark and sunlit sides, respectively. In the opposite hemisphere, at this time, the Pi2-related component of the meridional current is northward, and the associated magnetic perturbation is directed westward (not shown here). The azimuthal magnetic perturbations at a certain meridian around the dawn terminator vanish because the magnetic perturbation due to the FAC cancels out the magnetic perturbations due to the meridional ionospheric current. This neutral line, where the azimuthal magnetic perturbations vanish, does not need to be located exactly at the dawn terminator because the location of the neutral line depends on the intensity and the location of both the FAC and the meridional current. The D component phase reversal on the dusk side may also be explained by a similar current system consisting of the premidnight FAC and the postnoon meridional current. However, the meridional component current may be weaker than that of the dawn side.

The middle latitude PTK shows a weaker sunrise/sunset reference time dependences than those at the low-latitude stations. The large yearly variation of the sunrise/sunset time probably causes weak dependences. At the summer solstice, the phase reversals around midnight (cause by FACs) and terminator (caused by a FAC and a meridional current) may be mixed because the sunrise is near midnight ($\sim$1.6 h LT). Also, the polarization of Pi2 is easily influenced by the location of the oscillating FACs with an

increase in the latitude. The middle latitude Pi2 polarization significantly varies from event to event because the location of the FACs may vary.
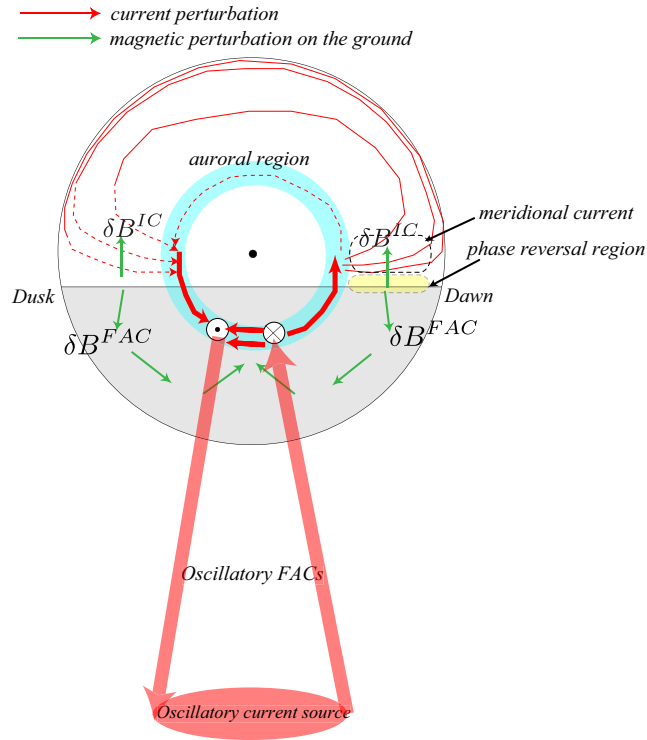
FIGURE 3.23: Schematic diagram of the current system explaining D component magnetic perturbations (*Imajo et al.*, 2015). Green and red arrows indicate magnetic and current perturbations, respectively. Magnetic perturbations produced by FACs are represented by δB^{FAC}, and magnetic perturbations on the ground produced by ionospheric currents are represented by δB^{IC}.

The D component phase reversal and the increase of D-to-H amplitude ratio have been found for also Pc $3-4$ pulsations observed around the dawn terminator although the source of these Pc pulsations are located in the dayside magnetosphere (*Saka et al.*, 1980, 1982; *Tanaka et al.*, 2007). *Tanaka et al.* (2007) showed that the direct incidence of Alfvén waves around the dawn terminator can explain the longitudinal phase variation of Pc3 pulsation. They also suggested that a large scale ionospheric current system produced by the Alfvén wave at higher latitudes is relevant to the D phase reversal at lower latitudes where Alfvén waves are difficult to exist. The equivalent current system (rotational part of ionospheric current system) of such ionospheric current system was numerically simulated by *Alperovich et al.* (1996). Their simulation results showed the change of equivalent currents near the dawn terminator but the feature of the change depends on the season (conductivity distribution) and location of the FAC (incident Alfvén wave).

Previous studies have tried to explain the terminator effect on the geomagnetic pulsations in terms of the change of pattern of the ionospheric current driving pulsations in the conductivity gradient region. On the other hand, in the model for Pi2 pulsation near the terminator proposed in this thesis, the magnetic field produced by nightside FACs much stronger than ground magnetic field produced by the current in the dark ionosphere. I consider that a difference in a dayside source or a nightside source can significantly affect the mechanism of the terminator effects on geomagnetic pulsations. A possible mechanism of the terminator effects on the Pi2 pulsation will be revealed by the numerical calculation in chapter 5.

Chapter 4

Spatial Properties and Equivalent Current Distribution of Dayside Pi2 Pulsation

4.1 Data Descriptions

In this chapter I use ground magnetic data from MAGDAS/CPMN (Magnetic Data Acquisition System/Circum-pan Pacific Magnetometer Network (*Yumoto and the MAGDAS Group*, 2006)), JMA (Japan Meteorological Agency), INTERMAGNET (International Real-time Magnetic Observatory Network (*Kerridge*, 2001)), USGS (U.S. Geological Survey), and McMAC (Mid-continent MAgnetoseismic Chain (*Chi et al.*, 2013)). The magnetic latitude of the used stations is limited to $-60 \sim 60°$ since Pi2 pulsations are not clearly identified in the high-latitude dayside due to large background variations. According to *Shinohara et al.* (1997), during daytime only less than 20% of events showed Pi2 oscillations at the higher latitudes were similar to those at the lower latitudes. The time resolution of all data is 1 s. For the data expressed in geographic coordinates (XYZ coordinates), I converted the coordinate system around the Z-axis by H (geomagnetic north) and D (geomagnetic east) components by rotating X and Y to the daily averaged magnetic declination.

4.2 Method to Derive an Equivalent Current Vector of Pi2

Figure 4.1 shows the diagram of the method to derive an equivalent current vector of Pi2. First I apply a bandpass filter with a period of 40 to 150 s to H and D components of magnetic data from all available stations. These filtered H and D component data are described as ΔH and ΔD, respectively (Figure 4.1a, b). Then I calculate the horizontal amplitude that is defined as $\sqrt{\Delta H^2 + \Delta D^2}$ (Figure 4.1c). The horizontal amplitude corresponds to the radial distance of a hodogram (Figure 4.1d). I examine the equivalent current distributions at the four largest local maxima of the horizontal amplitude (vertical lines in Figure 4.1c). The time of the four largest local maxima is determined from the data at the ASB station as a representative of all stations since the time difference of local maxima among stations is small (This will be shown in the next section). Finally I derive the equivalent current vectors at each time of the local maxima of horizontal amplitude by rotating vectors by 90° clockwise (Figure 4.1d, e). These estimated equivalent current vectors will be drawn on the map in IGRF (International Geomagnetic Reference Field) geomagnetic coordinates.
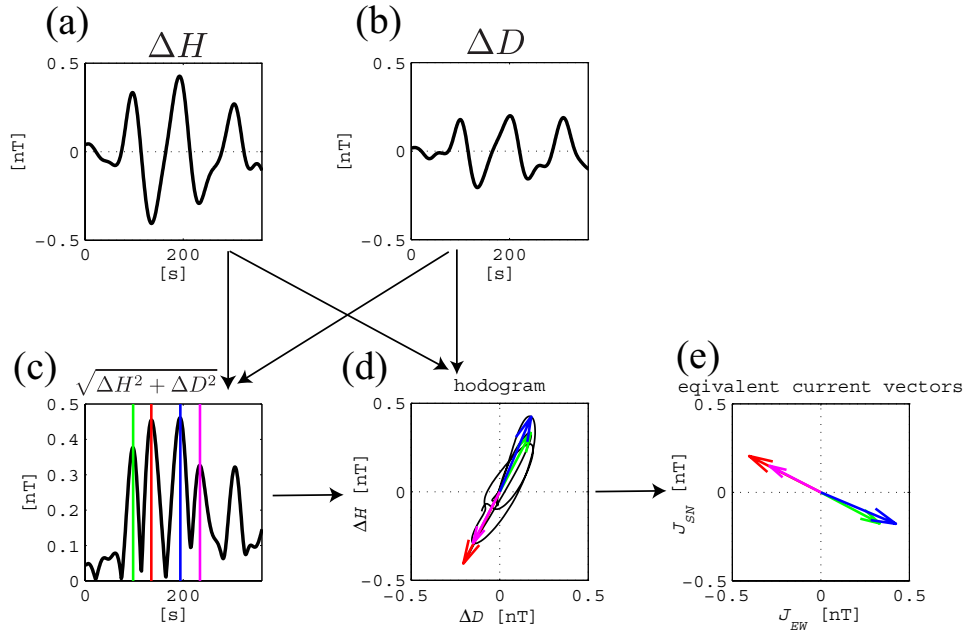
FIGURE 4.1: Examples of (a) H and (b) D component magnetic data that are bandpass-filtered with period of $40-150$ s. (c) Horizontal amplitude that is defined as $\sqrt{\Delta H^2 + \Delta D^2}$. (d) Hodogram with arrows indicating the magnetic vector at the times of four largest local maxima of the horizontal amplitude. (e) Equivalent current vectors of Pi2. The color coding of lines and arrows in (c)-(e) indicates each peak of the horizontal amplitude.

4.3 Case Studies

4.3.1 2310 UT, 02 February 2012 Event

In this section I show a detailed investigation of the Pi2 event occurring at 2310 UT on 2 February 2012. Magnetic data from 41 stations in the sunlit region were available. Figure 4.2 shows AL index and nightside magnetic variations. During this event AL index starts to decrease at 2300 UT on 2 February 2012, and reached -200 nT at 0020 UT on 3 February 2012, indicating that the event was related to a substorm onset. The magnetic data show clear Pi2 oscillations and small magnetic bays.
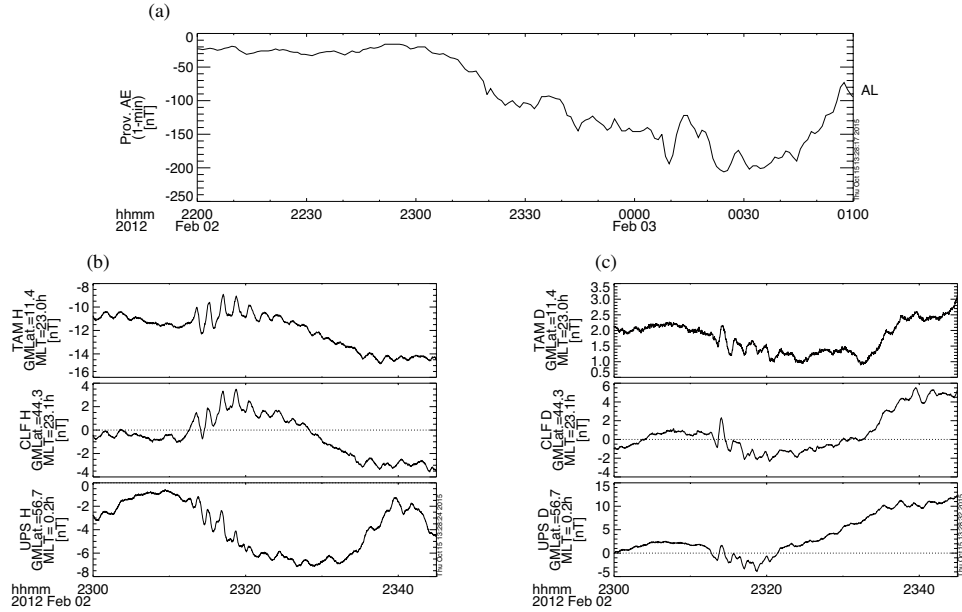
FIGURE 4.2: (a) AL index (b) H and (c) D component variations at the nightside stations.

Figure 4.3 shows ΔH and ΔD observed at longitudinally separated stations in the Northern Hemisphere. Pi2 waveforms can be seen from at least either ΔH or ΔD components for each station. At the prenoon station ASB the oscillation in the H component is not clear while the oscillation in the D component has a large amplitude ($\sim$0.6 nT). At the postnoon station TUC, the H component amplitude ($\sim$ 0.6 nT) is larger than the D component amplitude ($\sim$ 0.2 nT). At the HON station near the noon magnetic meridian, the D oscillation is small while the H oscillation has a large amplitude ($\sim$0.5 nT). The D component shows a phase reversal between ASB and TUC.
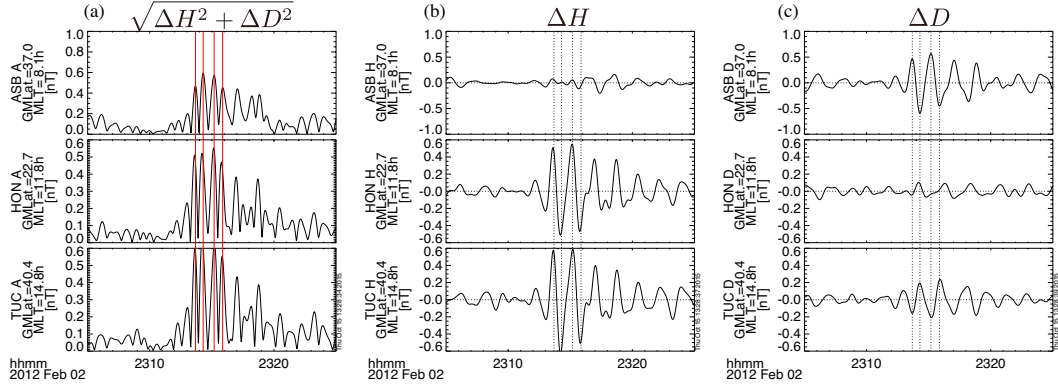
FIGURE 4.3: (a) Horizontal amplitude, (b) H component, and (c) D component magnetic data that are bandpass-filtered with period of $40-150$ s at the longitudinally separated stations. Vertical red lines in (a) show the successive four largest peaks at ASB. Vertical dotted lines in (b) and (c) indicate times of peaks at GUA and ASB, respectively.

Figure 4.4 shows $\sqrt{\Delta H^2 + \Delta D^2}$, ΔH, and ΔD observed at the stations in the prenoon Northern Hemisphere (MLT$= 6.9 - 8.9$ h). The times of the successive four largest local maxima of $\sqrt{\Delta H^2 + \Delta D^2}$ at ASB are indicated by the red vertical bars. Each local maximum is approximately coincident with each peak of $\sqrt{\Delta H^2 + \Delta D^2}$ at other stations. The intervals of local maxima correspond approximately to a half period of the Pi2. The H amplitude is largest at the nearest station of the magnetic equator (DAV), and its latitudinal profile is consistent with *Shinohara et al.* (1997). The amplitude of the D component tends to increase with latitude. The H component oscillations at the latitude from ONW to DAV are nearly in phase. The in phase relation between the magnetic equator and low-latitudes cannot be properly compared to the observation by *Shinohara et al.* (1998) because there is a small number of events during $0600-0800$ LT in their study. The D component at the latitude from MGD to KAG oscillates in phase.

Figure 4.5 shows $\sqrt{\Delta H^2 + \Delta D^2}$, ΔH, and ΔD observed at the stations in the postnoon Northern Hemisphere (MLT$= 14.1-17.7$ h). The McMAC stations (GLYN to SATX) are latitudinally aligned and the USGS stations (FRN to FRD) are longitudinally aligned. The red vertical bars show the same times defined from ASB data in Figure 4.4. The times of local maxima at all the postnoon stations are approximately coincident with the vertical bars, indicating that the local maxima of $\sqrt{\Delta H^2 + \Delta D^2}$ are nearly coincident at almost dayside stations. The H amplitude has a tendency to increase with latitude and MLT. The D amplitude is smaller than the H amplitude at each postnoon station. H component oscillations are nearly in phase. D component oscillations are also nearly in
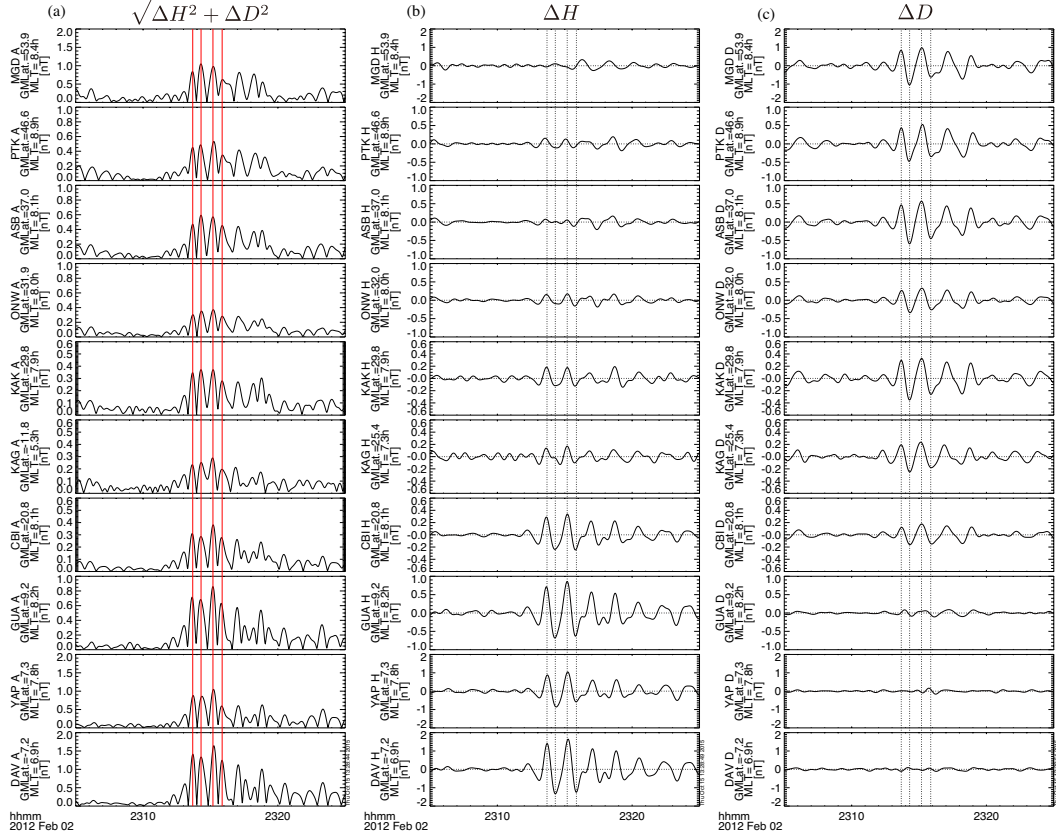
FIGURE 4.4: (a) Horizontal amplitude, (b) H component, and (c) D component magnetic data that are bandpass-filtered with period of $40-150$ s in the prenoon sector. Vertical red lines in (a) show the successive four largest peaks at ASB. Vertical dotted lines in (b) and (c) indicate times of peaks at HON and ASB, respectively.

phase at GLYN, WRTH, and BENN, but the oscillation at BSL is ambigous or disturbed before the Pi2 onset.

Figure 4.6 shows hodograms drawn on a map for $2312-2316$ UT on 2 February 2012. Note that amplitude of each hodogram is scaled by the maximum horizontal amplitude at each station. Most of the hodograms are nearly linearly polarized. In the middle-to-low latitude Northern hemisphere, the major axes in the prenoon sector are oriented in the northwest quadrant, while those in the postnoon sector are oriented in the northeast quadrant. The change of azimuth angles around noon corresponds to in-phase H and antiphase D oscillations across the noon meridian.

The snapshots of the equivalent current distribution associated with the Pi2 are illustrated in Figure 4.7. The time of each snapshot corresponds to each local maximum of $\sqrt{\Delta H^2 + \Delta D^2}$ at ASB represented by the red vertical bars in Figure 4.4 and 4.5. At 23:13:41 UT (Figure 4.7a), the meridional component of equivalent current vectors is
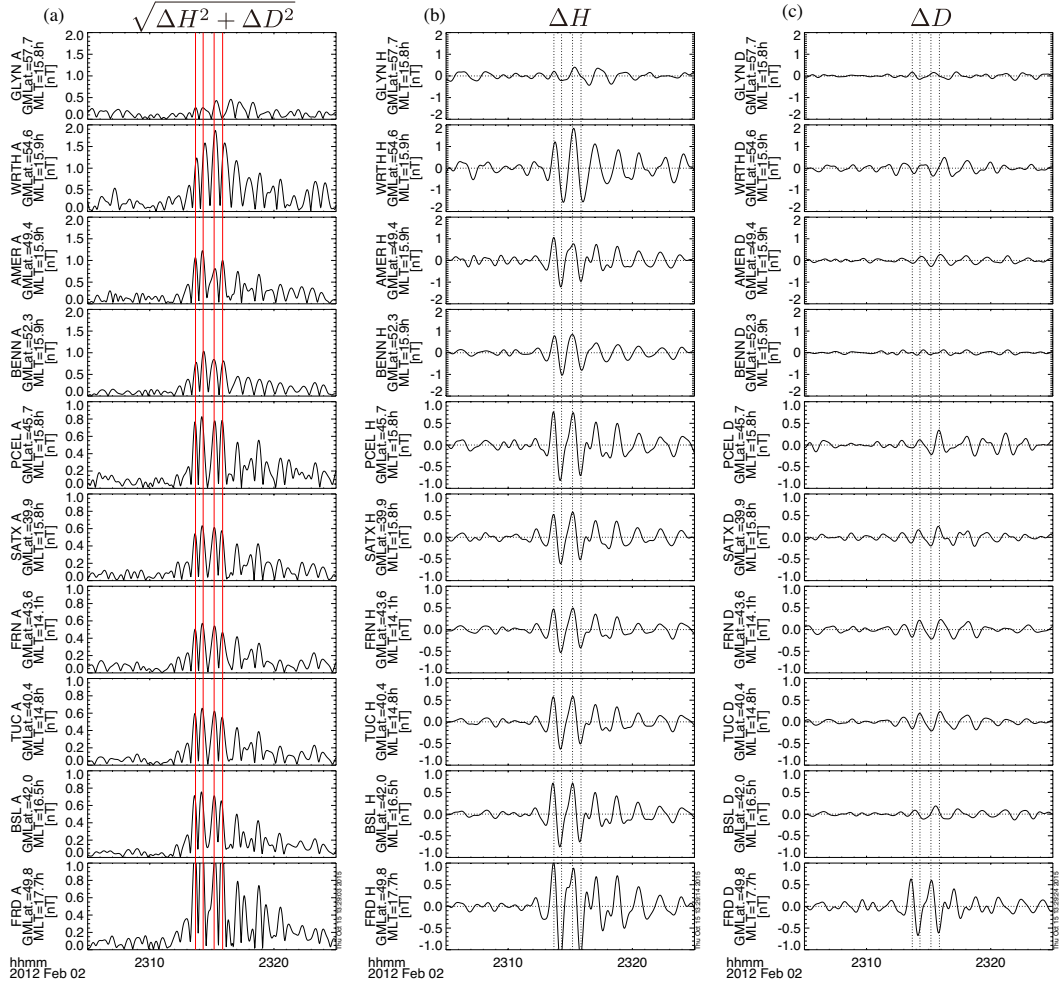
FIGURE 4.5: (a) Horizontal amplitude, (b) H component, and (c) D component magnetic data that are bandpass-filtered with period of $40-150$ s in the postnoon sector. The stations from GLYN to SATX are longitudinally aligned and the stations from FRN to FRD are latitudinally aligned. Vertical red lines in (a) show the successive four largest peaks at ASB shown in Figure 4.4. Vertical dotted lines in (b) and (c) indicate peaks at TUC.

directed equatorward in the prenoon sector and poleward in the postnoon sector. The opposite sense of meridional currents corresponds to the phase reversal of the D component around the noon meridian. The large meridional component of equivalent current vectors in the prenoon sector corresponds to the large D amplitude in this sector. The meridional component decreases with magnetic latitude and vanishes near the magnetic equator, in agreement with the latitudinal profile of the D amplitude. The zonal component of equivalent current vectors is largest near the magnetic equator, corresponding to the equatorial enhancement of H oscillations. The equivalent current distribution shows that the meridional equivalent current flows to connect with eastward equivalent currents in the equatorial region. The meridional component in the prenoon sector
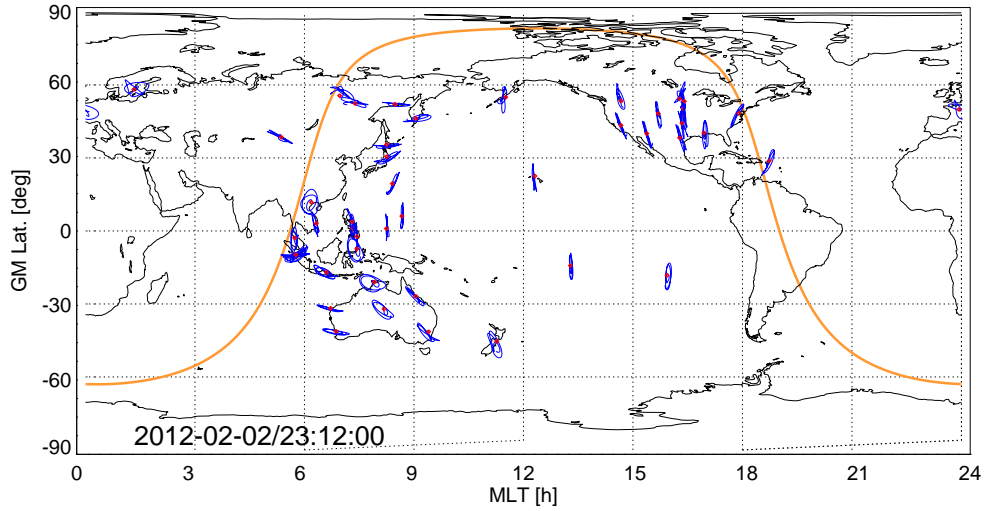
FIGURE 4.6: Hodograms on the map for 2312−2316 UT on 2 February 2012. The amplitude of each hodogram is scaled by the maximum horizontal amplitude at each station.

is larger than in the postnoon sector and the zonal component in the prenoon sector is smaller than in the postnoon sector; the pattern of equivalent currents exhibits a prenoon-postnoon asymmetry. The equivalent current distribution 37 s later at 23:14:18 UT (Figure 4.7b) is similar to the previous one but its flow direction is opposite. The meridional component of equivalent current vectors is directed poleward in the prenoon sector and equatorward in the postnoon sector. The equivalent current distributions at 23:15:11 UT (Figure 4.7c) and 23:15:52 UT (Figure 4.7d) also show a similar pattern but flow directions are opposite to the previous one.

4.3.2 Other Examples

Figures 4.8 and 4.9 show filtered magnetic data from the three dayside stations (ASB, HON, and TUC) and equivalent current distributions during other two Pi2 events occurring at 2335 UT on 2 March 2012 and 2100 UT on 26 March 2012, respectively. The first event was related to a substorm since the AL index started to decrease in concurrence with Pi2 and reached -230 nT, while the second event may not be related to a substorm because of no clear AL decreasing (not shown here). The equivalent
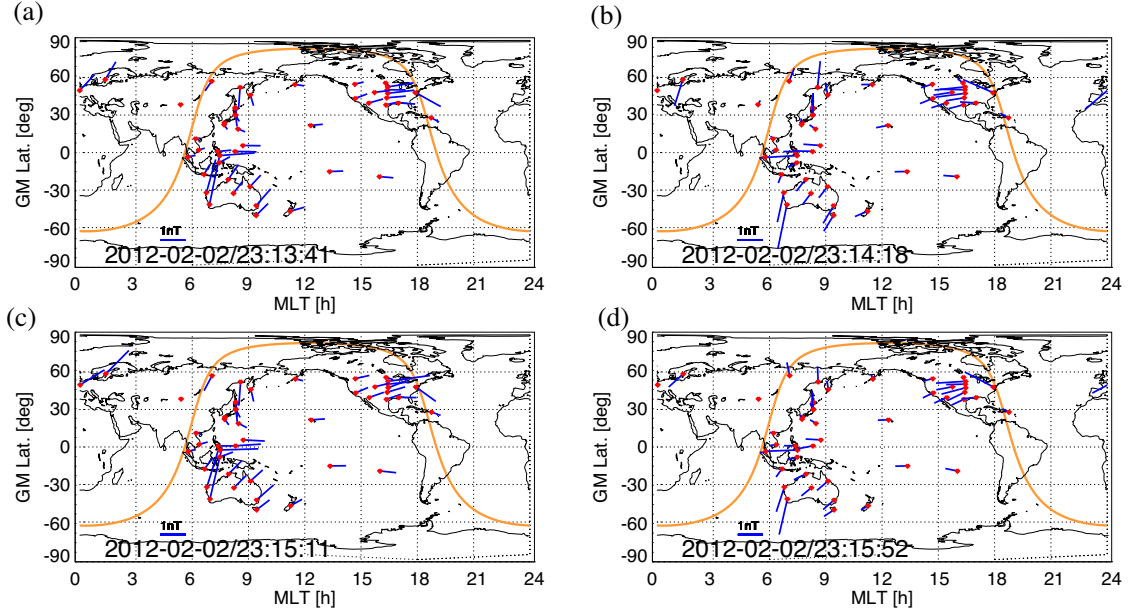
FIGURE 4.7: (a)-(d) Distributions of equivalent currents at the four successive times on the map in IGRF geomagnetic coordinates. Red dots show locations of stations and blue pointers show an equivalent current over each station. The grey and white regions show dark and sunlit regions at 100 km in altitude, respectively.

current distributions of both events basically support features of the previous event. Local maxima of $\sqrt{\Delta H^2 + \Delta D^2}$ are nearly coincident among latitudinally separated three dayside stations. The D oscillation at the prenoon station ASB is in antiphase with the D oscillation at the postnoon station TUC. The D amplitude at ASB is larger than the D amplitude at TUC. As a consequence, both events show similar equivalent current distributions to the previous event. Summarizing equivalent current distributions for three events, the equivalent current associated with the dayside Pi2 flowed into the equator region from a higher latitude region via meridional equivalent currents in the prenoon and postnoon sectors. The equivalent current system simultaneously oscillated with a Pi2 period and exhibited the prenoon-postnoon asymmetry that the meridional component in the prenoon sector was larger than those in the postnoon sector.
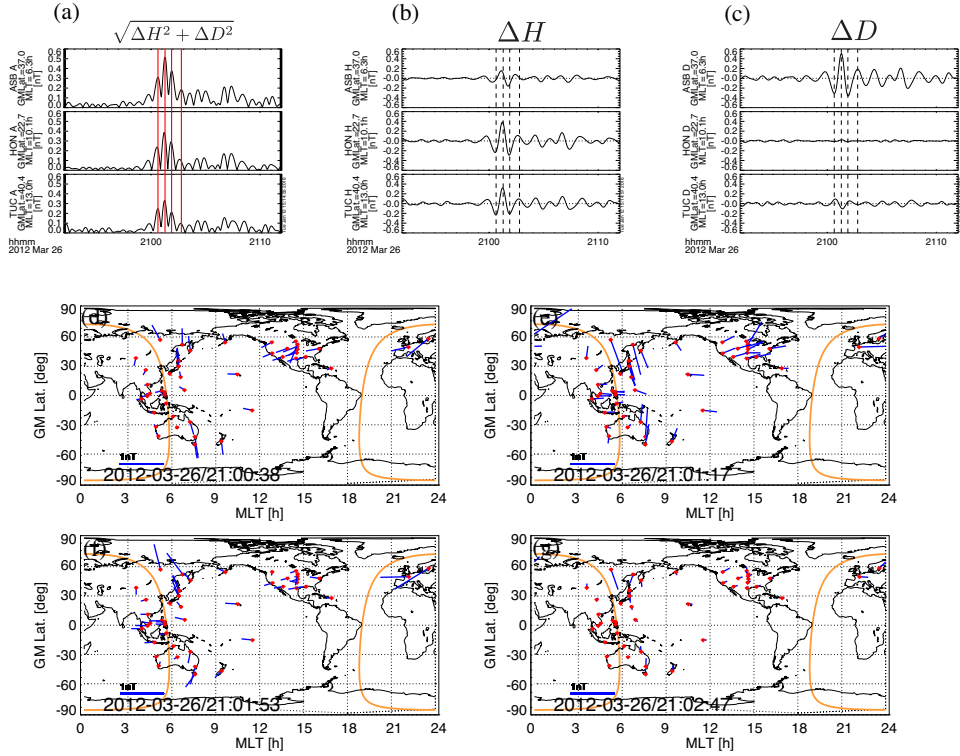
FIGURE 4.8: (a)-(c) Filtered magnetic data for 2326−2346 UT on 2 March 2012, in the same format as Figure 4.4 and 4.5. (d)-(g) distributions of equivalent currents at the four successive times in the same format as Figure 4.7.

4.4 Statistical Analysis

4.4.1 Longitudinal Features of Dayside Pi2

I statistically analyze dayside Pi2s simultaneously observed at ASB, HON, and TUC, located in the prenoon, noon, and postnoon sectors, respectively. The local time separation between ASB and HON is −4.0 h, and the local time separation between TUC and HON is 3.2 h. Pi2 events are selected from HON data during the period from 1 November 2011 to 31 October 2012 between 10 and 14 h LT. I select a total of 69 Pi2 events in this interval using the procedure presented in section 3.1. TAM data are used as a reference of nightside Pi2 for visual inspection. Thus, ASB is in the local time sector 6.0 to 10.0 h, and TUC is in the local time sector 13.2 to 17.2 h.

I confirm whether nearly simultaneous Pi2 oscillations among longitudinally separated station, which are found in the case study, are found in the majority of dayside Pi2 events. To calculate the time lag of peaks of $\sqrt{\Delta H^2 + \Delta D^2}$, I use a cross-correlation
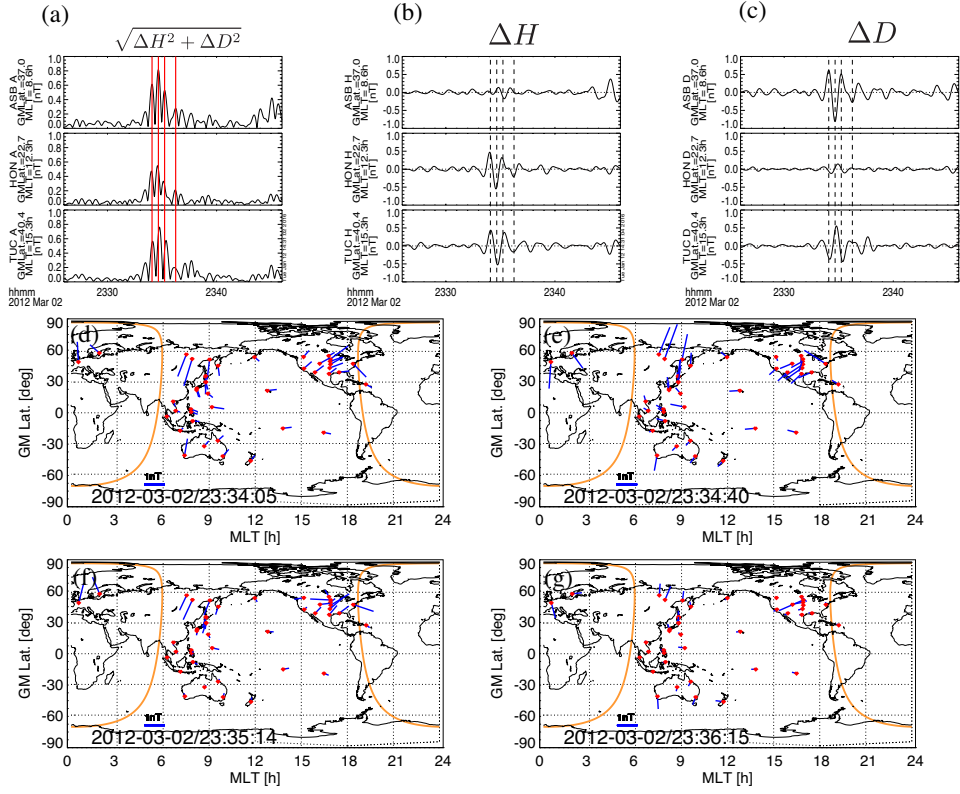
FIGURE 4.9: Filtered magnetic data for 2052−2112 UT on 26 March 2012 and the distributions of equivalent currents at the four successive times in the same format as Figure 4.8

analysis. The correlation function $(R(\tau))$ is calculated in the interval of $T_{max} - 150$ s to $T_{max} + 150$ s as:

$$R(\tau) = \int_{T_{max}-150}^{T_{max}+150} A_{\mathrm{HON}}(t) A_{\mathrm{STN}}(t - \tau) dt \qquad (4.1)$$

where $A_{\mathrm{STN}}(t)$ is $\sqrt{\Delta H^2 + \Delta D^2}$ at STN and τ is a lag $(-90 \leq \tau \leq 90$ s$)$. The delay time is determined by τ when the $R(\tau)$ is a maximum peak. To avoid analytical errors, the delay time was only used in the analysis when maximum $R(\tau)$ was greater than 0.75. About 78% and 86% of the events satisfied this threshold for ASB and TUC, respectively.

Figure 4.10 shows typical examples of the selected events. ΔT_{ASB} and ΔT_{TUC} are time delays of A_{ASB} and A_{TUC} from A_{HON}, respectively. The ΔT_{ASB} and ΔT_{TUC} are small and positive. The waveforms show that ASB D is in nearly antiphase with TUC D. The amplitude of HON H is much larger than that of HON D. The amplitude of ASB
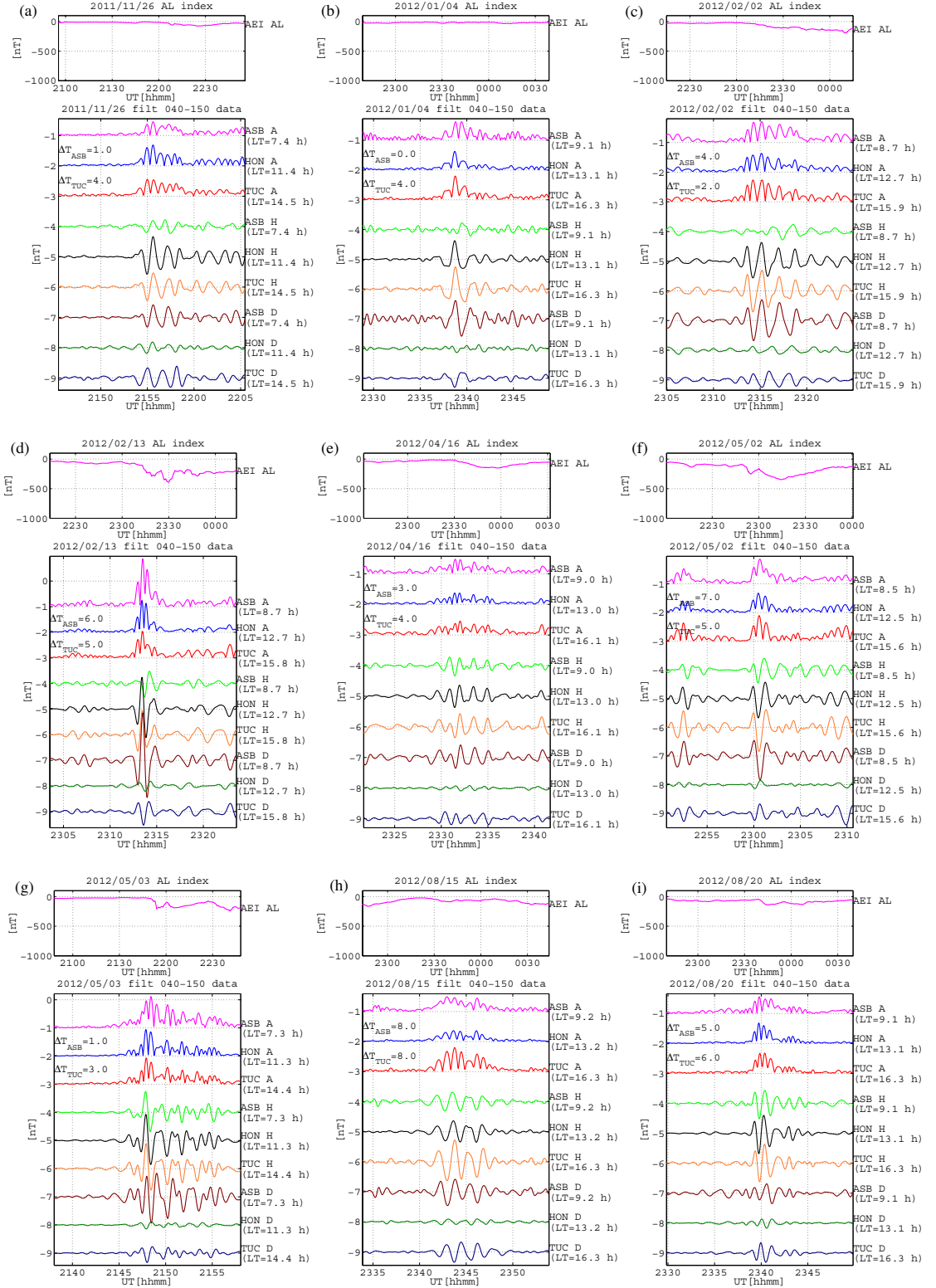
FIGURE 4.10: Typical examples of the selected events. For each events, upper panel shows AL index, and lower panel shows $\sqrt{\Delta H^2 + \Delta D^2}$, H, and D components filtered data at ASB, HON, and TUC. ΔT_{ASB} and ΔT_{TUC} are time delays of A_{ASB} and A_{TUC} from A_{HON}, respectively.

D is larger than that of ASB H. The amplitude of TUC H is larger than that of TUC D. Although the D-to-H amplitude ratios are different among stations, $\sqrt{\Delta H^2 + \Delta D^2}$ is comparable.

Figure 4.11 shows distributions of phase lags between HON H and ASB D, between HON H and TUC D, and between ASB D and TUC D. The phase of ASB D is delayed by $\sim 45°$ from HON H. The phase of HON H leads TUC D by $\sim 135°$, which corresponds to a phase delay of $\sim 45°$ from an antiphase relation ($180°$). As expected from Figure 4.11a and b, ASB D is in nearly antiphase with TUC D (Figure 4.11c), which is consistent with case studies. About 81% of phase lag is within $180 \pm 45°$.
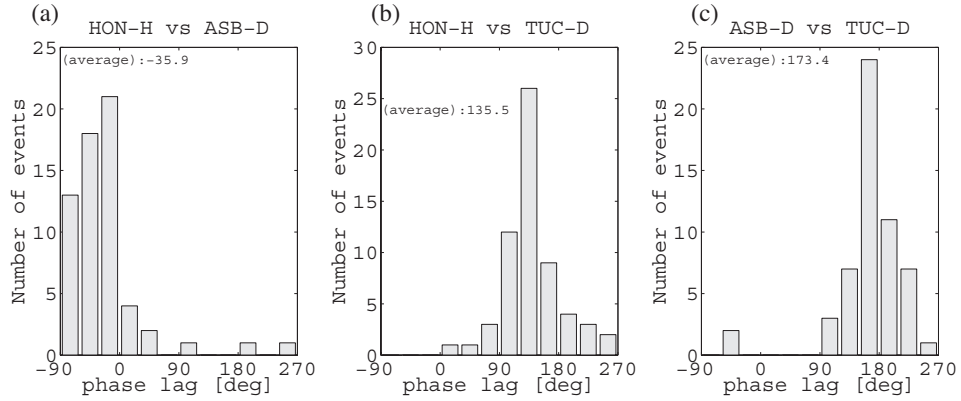
FIGURE 4.11: Distributions of phase lags (a) between HON H and ASB D, (b) between HON H and TUC D, and (c) between ASB D and TUC D.

Figure 4.12 is distributions of D-to-H amplitude ratio. Most of D-to-H amplitude ratios at ASB is larger than 1, which means that D component is dominant in the prenoon sector. The D-to-H amplitude ratio at HON is very small, indicating that most of low-latitude Pi2 pulsations around the noon is polarized in the H direction. At TUC, the D-to-H amplitude ratio is also small but larger than at HON. The mean values at ASB, HON, and TUC are 1.92, 0.30, and 0.49, respectively.

Figure 4.13 illustrates the distribution of time lag of $\sqrt{\Delta H^2 + \Delta D^2}$. Positive time lag indicates that HON is delayed from ASB or TUC. Up to 76% of time lags for ASB and 91% of time lags for TUC are within ± 10 s, although HON tends to lead ASB and TUC. Thus dayside Pi2s nearly simultaneously oscillate in a wide local time sector in most cases.

Figure 4.14 is the relation of maximum $\sqrt{\Delta H^2 + \Delta D^2}$ among ASB, HON, and TUC. The correlation coefficient between HON and ASB is 0.815 and the correlation coefficient
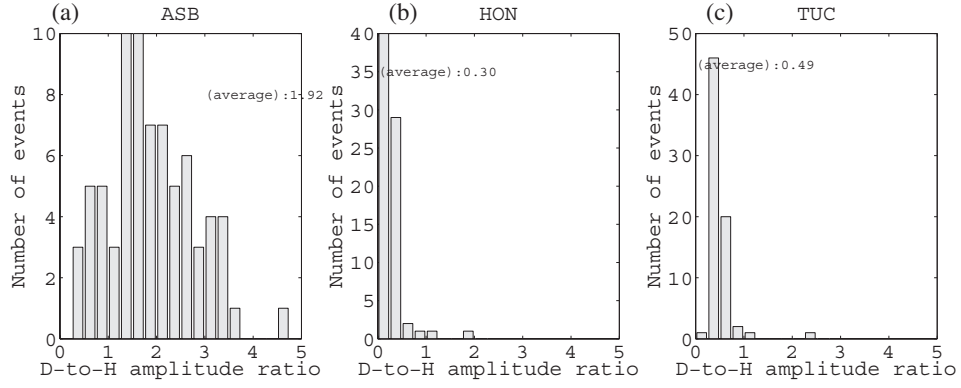
FIGURE 4.12: Distributions of *D*-to-*H* amplitude ratios at (a) ASB, (b) HON, and (c) TUC.
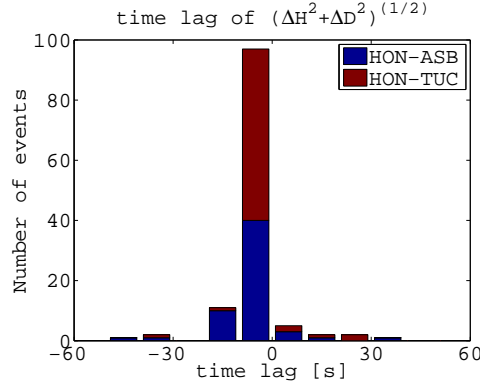
FIGURE 4.13: Distributions of time lags of $\sqrt{\Delta H^2 + \Delta D^2}$ between HON and ASB, and between HON and TUC.

between HON and TUC is 0.842. The equations of the regression line are described as:

$$y = 0.930x + 0.115 \tag{4.2}$$

for HON vs ASB, and

$$y = 1.244x + 0.010 \tag{4.3}$$

for HON vs TUC, respectively. The gradient of the regression lines is close to 1 and the intercept coefficient is small, indicating that the amplitude of dayside low-latitude Pi2 varies little with local time.

Here I also examine the amplitude relation between dayside and nightside to confirm that the dayside Pi2 source is still related to the nightside Pi2 source. Figure 4.15 shows the relation of maximum $\sqrt{\Delta H^2 + \Delta D^2}$ between dayside HON and nightside TAM. The

(a)   **(b)**
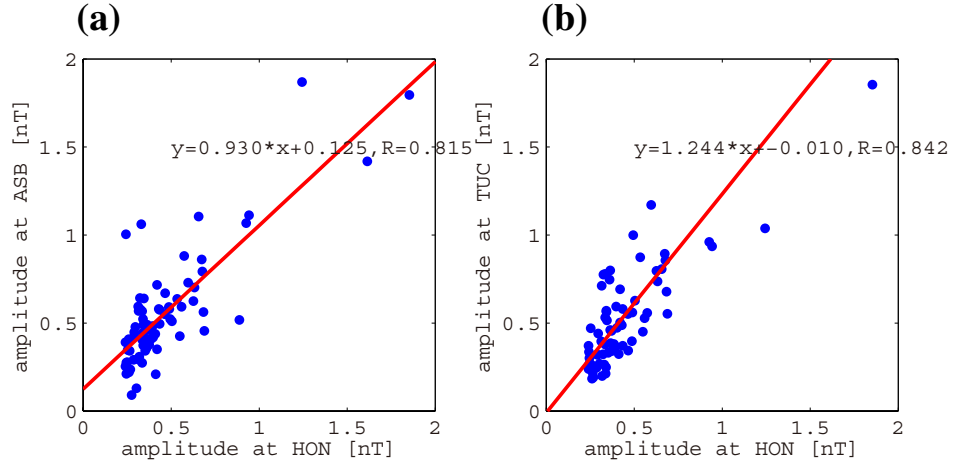
FIGURE 4.14: relation of maximum $\sqrt{\Delta H^2 + \Delta D^2}$ (a) between HON and ASB (b) between HON and TUC.

correlation coefficient is substantially high (0.784) and the amplitude of nightside Pi2 is about twice times larger than that of dayside Pi2.
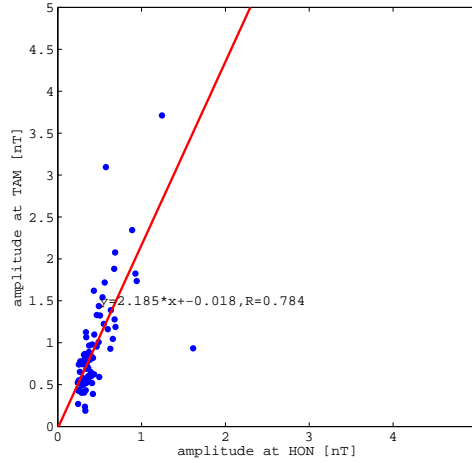
FIGURE 4.15: The relation of maximum $\sqrt{\Delta H^2 + \Delta D^2}$ between dayside HON and nightside TAM

4.5   Interpretations of Observational Results

I found the D component in the prenoon sector is in antiphase with that in the postnoon sector. Since the magnetic effects of nightside FACs and fast mode waves probably cannot reach the dayside regions, these D oscillations would be produced by ionospheric current. In this context, the D phase reversal means that the meridional ionospheric current in the prenoon sector is in antiphase with that in the postnoon sector.

Largely, one can recognize a in phase relation between the prenoon D and the noon H, and antiphase relation between the postnoon D and the noon H. This result leads to the same conclusion as before that the meridional component of equivalent currents is oppositely directed between prenoon and postnoon sectors so as to connect with zonal equivalent currents at noon and the magnetic equator. This pattern was also found in the previous study of the equivalent current distributions of Pc5 (Figure 10 in *Motoba et al.* (2002)) although they did not mention this point. The source region of Pc5 is believed to be in the dayside (or dawn and dusk) magnetosphere while the Pi2 source is localized in a narrow region of the nightside magnetosphere. The magnetospheric components (e.g., FACs and fast mode waves) associated with such dayside-source phenomena may significantly contribute to the ground magnetic variation at dayside low latitudes, and the ionospheric current contribution become relatively small. I suggest that the dayside Pi2 equivalent current pattern better reflects ionospheric currents than dayside magnetospheric source currents.

The D-to-H amplitude ratio in the prenoon sector ($\sim$1.92 on average) is larger than that in the postnoon sector ($\sim$0.49 on average). Consequently, the equivalent currents exhibited the prenoon-postnoon asymmetry that the ratio of meridional currents to zonal currents in prenoon sector was larger than that in the postnoon sector. *Tsunomura and Araki* (1984) calculated the two-dimensional ionospheric current distribution produced by upward and downward FACs around dawn and dusk auroral regions. The calculated ionospheric current distribution shows a similar asymmetry of the present equivalent current distribution. Numerical calculations by previous studies have shown that a global electric potential distribution is deformed under the condition of a nonuniform conductivity distribution (e.g., *Wolf*, 1970; *Peymirat and Fontaine*, 1994; *Tsunomura*, 1999; *Nakamizo et al.*, 2012; *Ebihara et al.*, 2014). A common feature of these results is that the polar potential tends to expand to the lower latitude region on the dawn side and remain in the polar region on the dusk side. *Yoshikawa et al.* (2013) theoretically separated ionospheric currents into a symmetric part and an asymmetric part (the primary current system and the secondary current system, respectively, in their paper). The asymmetric part is composed of the total Hall current and the secondary Pedersen current driven by Hall polarization fields. However, it is still not clear that FACs localized on the nightside can create dayside current closures with a similar type of the asymmetry. The numerical calculation of the global ionospheric current system

driven by nightside localized FACs will be investigated in the next chapter.

The phase relation of dayside Pi2s supported the dayside ionospheric current closure proposed in the previous chapter (Figure 3.23). Considering the prenoon-postnoon asymmetry of D-to-H amplitude ratio, I modify the shape of the current closure as shown in Figure 4.16. The meridional current intensively flows into the equator in the prenoon sector and gradually returns from the equator in the postnoon sector. In the low-to-middle latitudes, the meridional current producing the D magnetic field in the prenoon sector is larger than that in the postnoon sector. The deformation may also explain why the meridian of the D phase reversal on the dusk side tends to shift about $1-3$ h sunward from the dusk terminator. Magnetic perturbations produced by the premidnight FAC can easily penetrate to the dusk side sunlit region if the dusk side meridional ionospheric current is weak. It is also considered that the magnetic effect of the premidnight FAC is probably stronger than that of the postmidnight FAC because the Pi2 source, which is considered to be at the center of Pi2-associated FACs, is shifted to premidnight side on average (e.g., *Uozumi et al.*, 2007).

Small time differences of peaks of the horizontal amplitude (within$\pm 10°$) indicate that the propagation time of the electric field is much shorter than a period of Pi2 ($40-150$ s) in the context of the ionospheric current system. The TM_0 mode wave propagates at the speed of light from the polar ionosphere to the dayside equatorial ionosphere within ~ 0.05 s, which agrees with the small time difference, although there has been no observation directly determining the propagation mechanism of the electric field. Small time differences also mean that the induction effect is not significant at low latitudes. On the other hand, *Shinohara et al.* (1998) showed the phase difference at the dip equator is delayed by $\sim 30°$. However, this phase shift does not significantly affect the pattern of equivalent current because the value at the $30°$ phase shift from a peak does not differ much from a peak value (86% of a peak value for a sine function). I suggest that the induced ionospheric current at the equator may exist but this is not significant compared with the electrostatic currents.

The amplitude at noon HON had high correlation with that of prenoon ASB, postnoon TUC, and nightside TAM. The high correlation of amplitudes between different local times means that the dayside Pi2 is driven by a common source, and the amplitude observed by each observatory is strongly controlled by the magnitude of the Pi2 source.

I suggest that 'Pi2 magnitude', which is the magnitude of Pi2 event, can be defined by correction of the local time dependence on the Pi2 amplitude.

Hashimoto et al. (2011) found antiphase deflections of the D component magnetic bay between prenoon and postnoon sectors after a substorm onset. They interpreted that these deflections were caused by the meridional ionospheric current connecting to the equatorial counterelectrojet driven by the region 2 sense FACs that are in antiphase with the SCW. This means that the relation between H magnetic variations at the dayside equator and those at nightside low latitudes differs between Pi2 oscillations and magnetic bays, and the global configuration of the oscillating current system of Pi2 differs from that of the non-oscillatory current system. It is worth comparing global features between Pi2 perturbations and magnetic bays to further understand the relation between the current systems of Pi2 and substorm.
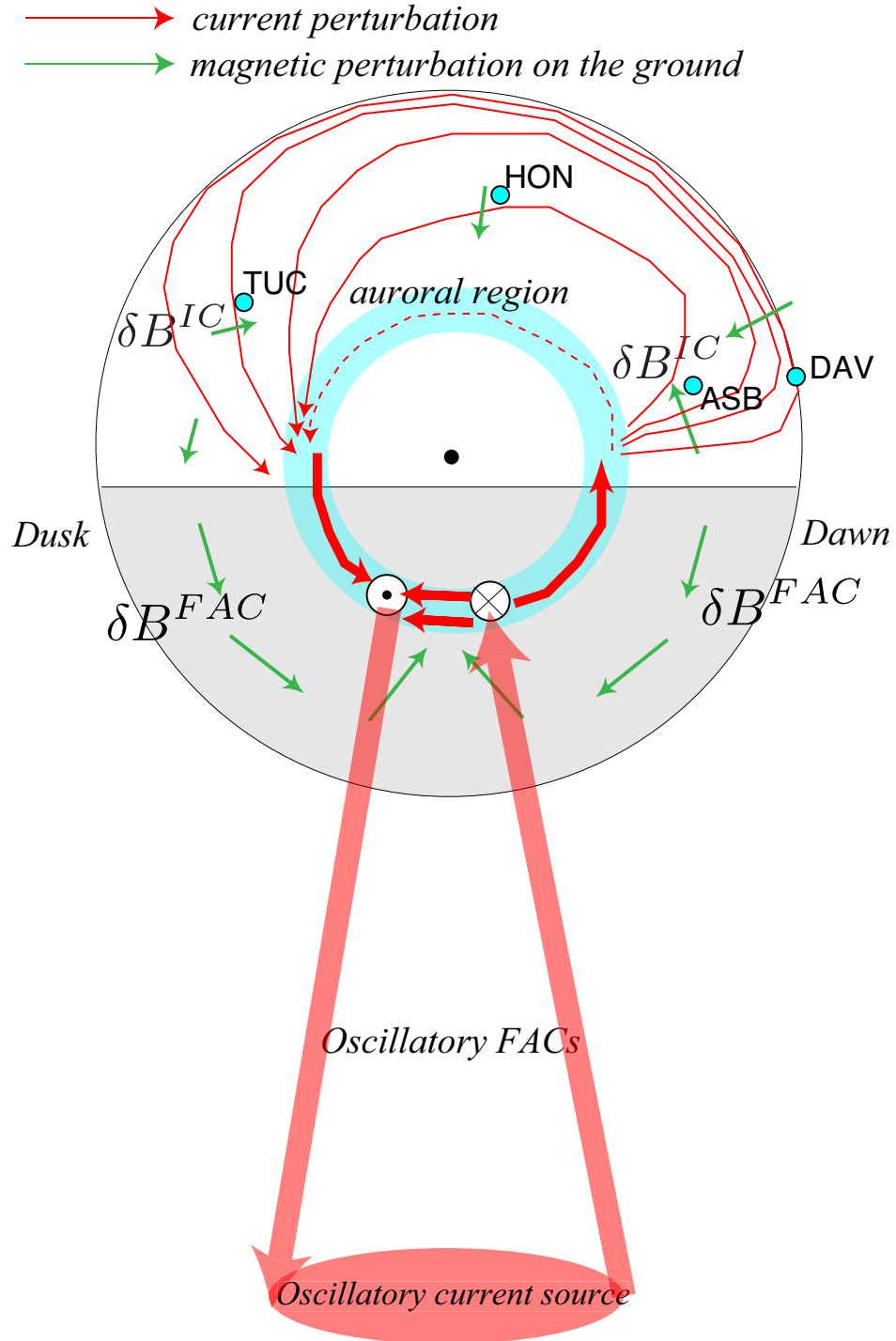
FIGURE 4.16: Schematic illustration of the current system to explain equivalent current distributions of dayside Pi2. Green arrows indicate magnetic perturbations, and red stream lines indicate current closures. Magnetic perturbations produced by mainly FACs are represented by δB^{FAC}, and magnetic perturbations on the ground produced by mainly ionospheric currents are represented by δB^{IC}.

Chapter 5

Application of Global Three Dimensional Current Model: Numerical Modeling of Ground Magnetic Field

5.1 Description of Model

In this section, I introduce the model to calculate ground magnetic fields produced by the three-dimensional current system. The model adopts the polar coordinates (r, θ, ϕ) in which r is the radial distance from the center of the Earth, θ is the colatitude, and ϕ is the longitude. First I make the model three-dimension current system, and then calculates the ground magnetic field produced by the current system using the Biot-Savart law generalized in polar coordinates (*Kisabeth and Rostoker*, 1977). As shown in Figure 5.2, the current system consists of three parts, FACs, a magnetospheric closure current, and horizontal ionospheric currents. All these currents are derived from the scalar current density of FACs on the ionospheric shell ($j^I_{//}$, positively downward). The altitude of the ionospheric shell (r^I) in which the horizontal ionospheric current flows is set to $r^I = R_E + 100$ km. The distribution of the $j^I_{//}$ is given similarly as that of previous studies (*Kamide and Matsushita*, 1979; *Tsunomura*, 1999; *Nakamizo et al.*, 2012) as follows:

$$j_{//}^I = -j_0 \exp\left[-\frac{(\theta-\theta_0)^2}{D_\theta{}^2} - \frac{(\phi-\phi_W)^2}{D_\phi{}^2}\right] + j_0 \exp\left[-\frac{(\theta-\theta_0)^2}{D_\theta{}^2} - \frac{(\phi-\phi_E)^2}{D_\phi{}^2}\right] \quad (5.1)$$

where j_0 is the maximum value of $j_{//}^I$, θ_0 is the latitude of peaks of $j_{//}^I$, ϕ_W and ϕ_E are the longitudes of peaks of westside and eastside FACs, respectively, and D_θ and D_ϕ are latitudinal and longitudinal scale parameters of $j_{//}^I$, respectively. D_θ and D_ϕ are fixed to $3°$ and $15°$, respectively, for all calculations.

The grid points on the ionospheric shell are composed of 257 (longitude) $\times$ 257 (latitude) matrix. The latitudinal grid spacing is smaller near the equatorial region since the conductivity gradient is large due to the modification of the Cowling conductivity; 20% of the grid points is used in the colatitude of $80-100°$ and remaining 80% of grid points is used in other latitudes (Figure 5.1). Note that the grid size shown in Figure 5.1 is reduced by 1/4 of the actual grid size for better visibility.
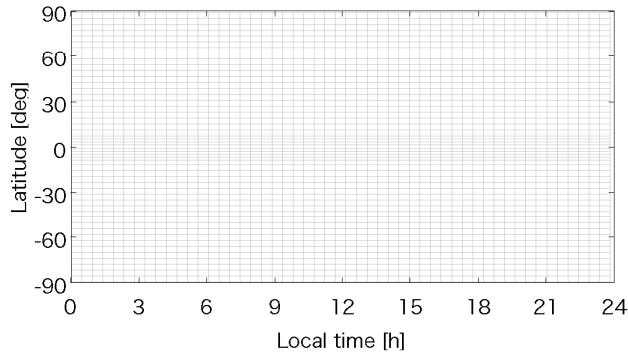
FIGURE 5.1: The grid distribution in the ionospheric shell. Note that the grid size is reduced by 1/4 of the actual grid size for better visibility.

The diagram of the procedure for making the model current system is shown in Figure 5.3. The horizontal ionospheric current ($\mathbf{J}$) is simulated under realistic conductivity distributions solving the electrostatic potential. FACs ($j_{//}^M$) are made by tracing the dipole field line from each grid of ionospheric FAC footprint. The magnetospheric closure current ($\mathbf{j}_\perp^M$) closes in the equatorial plane ($\theta = \frac{\pi}{2}$), and flows in purely azimuthal direction. The input parameters are only $j_{//}^I$ and conductivity distributions ($\mathbf{\Sigma}$) on the ionospheric shell. I will explain in detail methods for making the model current for each component in the following subsections.
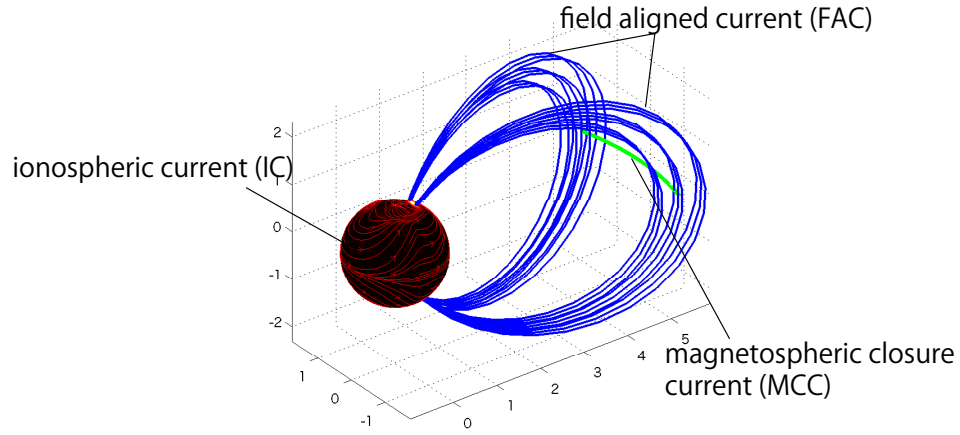
FIGURE 5.2: The configuration of the model current system.
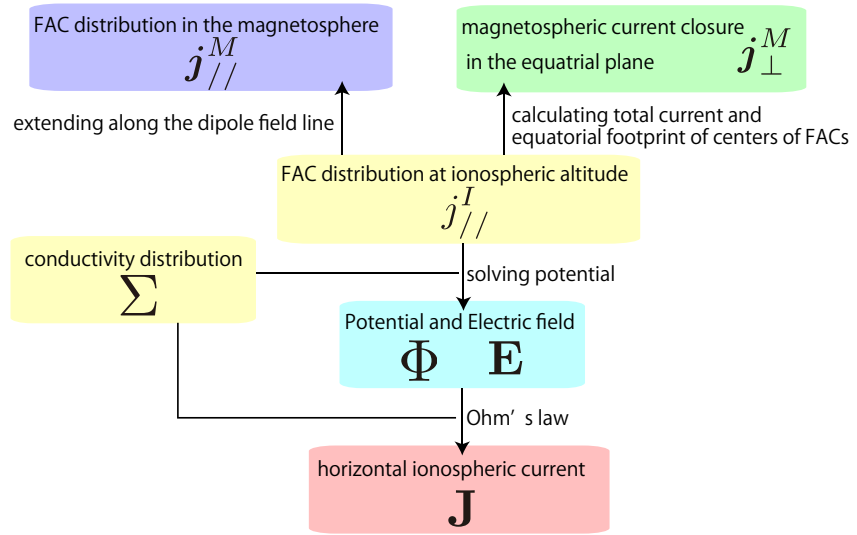
FIGURE 5.3: The diagram of the procedure for making the model current system.

5.1.1 Field-Aligned Current

I assume that the FAC is purely along the dipole field line. The location of the current line extended from the ionospheric altitude is given by

$$r = r^I \left(\frac{\sin \theta^I}{\sin \theta} \right)^2 \tag{5.2}$$

where θ^I is the colatitude at the ionospheric footprint of the dipole line. The number of grid in one field line is 180 points, and the latitudinal spacing is uniform.

The current density along the field line from the ionosphere to the equatorial plain ($\boldsymbol{j}_{//}^M$) can be described by values at the ionospheric altitude:

$$\boldsymbol{j}_{//}^M = \pm j_{//}^I \frac{r^{I2} \sin \theta^I}{r^2 \sin \theta} \frac{1}{\sqrt{4 \cot^2 \theta^I + 1}} (2 \cot \theta \hat{\boldsymbol{r}} + \hat{\boldsymbol{\theta}}). \tag{5.3}$$

where a positive sign is for the Northern Hemisphere and a negative sign is for the Southern Hemisphere. The derivation method of the equation is shown in the Appendix A.

5.1.2 Magnetospheric Closure Current

I assume that FACs are closed in the equatorial plane ($\theta = \frac{\pi}{2}$) in the magnetosphere, and the closure current flows in purely azimuthal direction. I treat this magnetospheric closure current (MCC) $\boldsymbol{j}_{\perp}^M$ as a line current for simplicity because the current is far away from the Earth's ground and the volume of the current probably does not affect the result. The absolute value of $\boldsymbol{j}_{\perp}^M$ equals to the total current intensity of the overall current system. The total current intensity corresponds to a half of the spherical surface integration of $\left| j_{//r}^I \right|$, which is the absolute value of the radial component of FACs at the ionospheric altitude:

$$\left| \boldsymbol{j}_{//}^M \right| = \iint_S \frac{1}{2} \left| j_{//r}^I \right| r^{I2} \sin \theta^I \delta \theta^I \delta \phi^I \tag{5.4}$$

$$j_{//r}^I = \frac{2 \cot \theta^I}{\sqrt{4 \cot^2 \theta^I + 1}} j_{//}^I. \tag{5.5}$$

The current is assumed to flow between the equatorial footprints of peaks of FACs, and the location of the current line is

$$r = \frac{r_1}{\sin^2 \theta_0} \tag{5.6}$$

$$\theta = \frac{\pi}{2} \tag{5.7}$$

$$\phi_W \leq \phi \leq \phi_E. \tag{5.8}$$

The number of grids between ϕ_W and ϕ_E is 60 points, and the longitudinal spacing is uniform.

5.1.3 Ionospheric Current

I numerically simulate the distribution of ionospheric currents (ICs) generated by FACs, solving the ionospheric electrostatic potential. The electrostatic potential is calculated in the frame of the model developed by *Nakamizo et al.* (2012), which is a model that applies so called "thin shell model" (e.g., *Fejer*, 1953; *Kamide et al.*, 1981; *Tsunomura and Araki*, 1984; *Tsunomura*, 1999) to the global ionosphere. In this section I briefly describe the model and basic equations used in this simulation.

To ensure current continuity, the divergence of ionospheric horizontal currents should equal to the radial component of FACs. The current continuity equation is given by

$$\nabla \cdot \mathbf{J} = j^I_{//r}, \tag{5.9}$$

where $\mathbf{J}$ are an ionospheric horizontal current. The zonal ionospheric current J_ϕ (positive east) and the meridional ionospheric current J_θ (positive north) are given by the Ohm's law,

$$
\begin{aligned}
\mathbf{J} &= \mathbf{\Sigma} \cdot \mathbf{E} \\
\begin{pmatrix} J_\theta \\ J_\phi \end{pmatrix} &= \begin{pmatrix} \Sigma_{\theta\theta} & \Sigma_{\theta\phi} \\ \Sigma_{\phi\theta} & \Sigma_{\phi\phi} \end{pmatrix} \begin{pmatrix} E_\theta \\ E_\phi \end{pmatrix}, \Sigma_{\phi\theta} = -\Sigma_{\theta\phi},
\end{aligned}
\tag{5.10}
$$

where $\mathbf{\Sigma}$ is a hight-integrated conductivity tensor integrated from 90 to 300 km in altitude, and $\mathbf{E}$ is an ionospheric electric field. I calculate the distribution of the hight-integrated conductivity tensor, using the FORTRAN code provided by Dr. Nakamizo (*Nakamizo et al.*, 2012). The method in this code includes the modifications by auroral precipitation (*Hardy et al.*, 1987) and the equatorial Cowling conductivity (*Tsunomura*, 1999). I do not take into account the conductivity change caused by the input FACs because the intensity of FACs associated with Pi2 is much smaller than that of background FACs (e.g., region-1 and -2 FACs). Thus the amplitude of input FACs is not important in this study because it does not affect conductivities and relative amplitude of an ionospheric current distribution.

Although the current system associated with Pi2 pulsation is not a steady state current, I assume that the inductive electric field is much smaller than the electrostatic field. $\mathbf{E}$

is obtained from only the electrostatic potential in the ionosphere Φ:

$$\mathbf{E} = -\nabla \cdot \Phi. \tag{5.11}$$

By substituting the equations 5.10 and 5.11 into the equation 5.9, I finally obtain the equation to be solved:

$$
\begin{aligned}
-r^{I^2} j^I_{//r} \sin \theta \;=\; & (\sin \theta \Sigma_{\theta\theta}) \frac{\partial^2 \Phi}{\partial \theta^2} + \left(\frac{\Sigma_{\phi\phi}}{\sin \theta}\right) \frac{\partial^2 \Phi}{\partial \phi^2} \\
& + \left\{ \frac{\partial}{\partial \theta}(\sin \theta \Sigma_{\theta\theta}) - \frac{\partial \Sigma_{\theta\phi}}{\partial \phi} \right\} \frac{\partial \Phi}{\partial \theta} \\
& + \left(\frac{1}{\sin \theta} \frac{\partial \Sigma_{\phi\phi}}{\partial \phi} + \frac{\partial \Sigma_{\theta\phi}}{\partial \theta} \right) \frac{\partial \Phi}{\partial \phi}.
\end{aligned}
\tag{5.12}
$$

The equation 5.12 is solved for Φ by the bi-conjugate gradient stabilized method (*Van Der Vorst*, 1992) ("bicgstab", built-in function of the MATLAB). $\mathbf{E}$ can be obtained by substituting Φ in equation 5.11, and J_ϕ and J_θ are obtained by substituting $\mathbf{E}$ in equation 5.10.

5.2   Results

5.2.1   Symmetric Input Parameters

First I use the symmetric input parameters shown in Figure 5.4 for simplicity. (The illustrations in the polar coordinate of figures in this section are available in Appendix B.) The $j^I_{//}$ distribution is symmetric with respect to the equator and midnight meridian. The center of upward FACs is located at 23 LT and $65°$ in latitude and the center of downward FACs is located at 1 LT and $65°$ in latitude. (*Samson and Rostoker*, 1983) showed that the peak amplitude of H component Pi2 is located at $64 - 68°$ geomagnetic latitude, and footpoints of Pi2-associated FACs is considered to be located in the same geomagnetic latitude range. $\Sigma_{\theta\theta}$ and $\Sigma_{\phi\phi}$ distributions are symmetric with respect to the equator and $\Sigma_{\theta\phi}$ distribution is antisymmetric with respect to the equator. Although the original calculated conductivity includes a weak dawn-dusk asymmetry, in this calculation the conductivity tensor in the $0-12$ LT sector is mirrored in the $12-24$ LT sector.
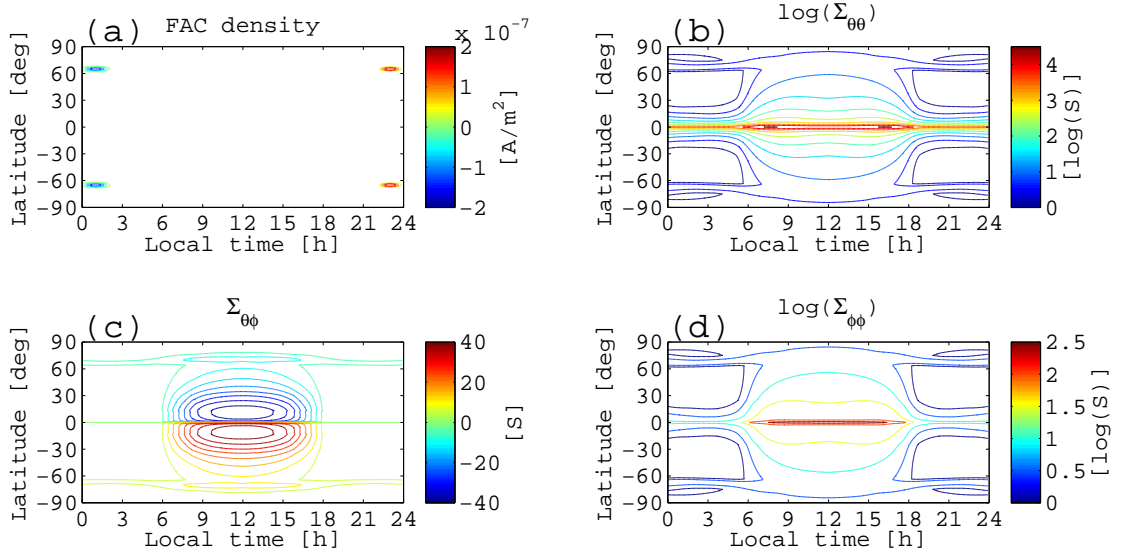
FIGURE 5.4: The distributions of (a) the FAC density at the ionospheric altitude ($j_{//}^I$), (b)-(d) Elements of the hight-integrated conductivities tensor.

Figure 5.5 illustrates distributions of the ionospheric potential and ionospheric electric field vectors. It is clear that the electric field is strong near the footprints of FACs. At low latitudes, the nightside electric field is stronger than the dayside electric field. The potential contour lines are asymmetrically deformed with respect to the noon-midnight meridian. Consequently the electric field also exhibits a dawn-dusk asymmetry.

FIGURE 5.5: Distributions of the ionospheric potential (Φ) and ionospheric electric field ($\mathbf{E}$) vector.

The two-dimensional distribution of simulated height-integrated ionospheric currents is shown in Figure 5.6. The current amplitude ($|\mathbf{J}|$) illustrated by the background color is saturated for visibility in the middle-to-equatrial latitudes (actual maximum value is

7.42×10^{-2}). Naturally the ionospheric current provided by the FACs mainly closes as the intense westward current in the auroral region because of a small distance between the upward and downward FACs and higher conductivities due to auroral precipitation. However, some parts of the ionospheric current flow out to the dayside region. The meridional currents in the dayside region flow equatorward in the prenoon sector and poleward in the postnoon sector. Around the noon meridian, the zonal current reaches a peak at the equator because of higher conductivities modified by the Cowling effect. The simulated dayside current system shows the prenoon-postnoon asymmetry similar to equivalent current distributions of dayside Pi2s, in which the meridional current in the prenoon sector is larger than in the postnoon sector.
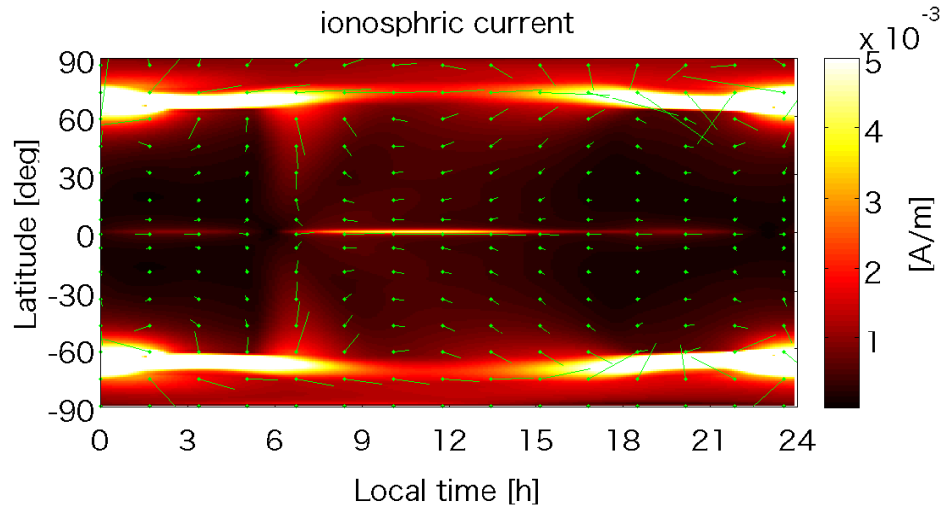
FIGURE 5.6: Simulated height-integrated ionospheric current distribution (**J**). The background color shows the current amplitude (|**J**|).

Figure 5.7 shows distributions of the calculated ground magnetic field and the equivalent current. The equivalent current vectors (Figure 5.7b, c, and d) are simply derived by rotating the magnetic vectors by 90° clockwise. Looking at Figure 5.7a, at low-to-middle latitudes, the east-west magnetic component is dominant around 8 LT, while the north-south magnetic component is dominant in $10-18$ LT. It is clear that the east-west magnetic component in the Northern Hemisphere is opposite to that in the Southern Hemisphere in the entire local time sector. The amplitude has a peak at the dayside equator. It should be noted that the total equivalent current pattern (Figure 5.7b) on the dayside is similar to the simulated ionospheric current pattern on the dayside. This means that the ionospheric current mainly contributes to the dayside equivalent current (or magnetic field). To confirm this interpretation, the equivalent currents caused by the

FIGURE 5.7: (a) Total magnetic vectors, (b) total equivalent current vectors, (c) equivalent current vectors caused by the ionospheric current, and (d) equivalent current vectors caused by the magnetospheric current. The color contour in (a), (c), and (d) shows the absolute value of the magnetic field. The background color in (b) shows the percentage of the contribution of the ionospheric current.
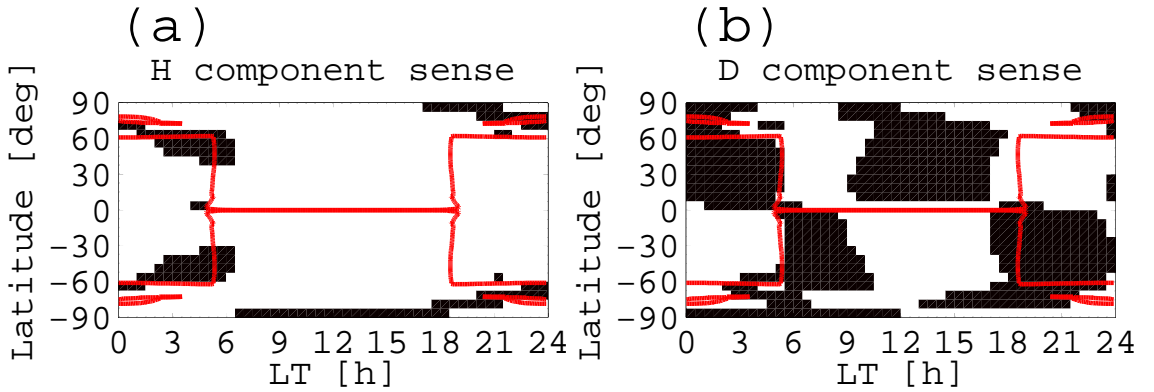
FIGURE 5.8: The distributions of sign of (a) H and (b) D components. The red line shows the isoline of $|\Sigma_{\theta\phi}| = 0.8$, which indicates that edges of conductivity near the terminator and the auroral region.

ionospheric current ($\mathbf{J}$) and the magnetospheric current ($\boldsymbol{j}_{//}^{M} + \boldsymbol{j}_{\perp}^{M}$) are shown in Figure 5.7c and d, respectively. The equivalent current of ionospheric current contribution on the dayside is larger than that on the nightside, and the equivalent current of magnetospheric current contribution is confined in the nightside region. The percentage of the ionospheric current contribution (R^{I}) shown in the background color in Figure 5.7b is defined as:

$$\mathrm{R}^I = \frac{\left|\mathbf{B}^I\right|}{\left|\mathbf{B}^I\right| + \left|\mathbf{B}^M\right|} \times 100 \tag{5.13}$$

At the latitudes between $-60°$ and $60°$, R^I on the dayside is about 90%, while R^I on the nightside is only about 20%. In the nightside auroral region, R^I is about 80% due to a strong auroral electrojet. The rise of R^I on the dawn side is steeper than the decrease in R^I on the dusk side.

If the current system oscillates in a quasi-steady state, the sign of magnetic fields shows phase relations of exactly $0°$ or $180°$. Figure 5.8 shows the distributions of the sign of H and D components. The white area is positive and the black area is negative. The red line shows the isoline of $|\Sigma_{\theta\phi}| = 0.8$, which indicates the edge of the higher conductivity region (sunlit and auroral regions). The H component is positive in most regions except the midnight auroral region and postmidnight middle latitudes. This means that the sign of H component at the low latitudes does not vary with local time. On the other hand, the D component shows a more complicated structure. The sign is antisymmetric with respect to the equator. In the middle-to-low latitude region, the sense changes at the 0, 5, 10 and 17 LT.

To see the contribution of each current component in detail, I show the LT dependence of magnetic fields at the specific latitudes produced by each current component in Figure 5.9. On the dayside, it is clear that the IC contribution nearly equals to the total magnetic field, and the MCC contribution cancels out the FAC contribution. The MCC contribution to H component is nearly constant over both latitude and local time, and the contribution to the D component is very small. The FAC contribution increases with latitude and becomes dominant on the nightside especially for the D component. The changes in sign of the D component appear at 0, 5, 10 and 17 LT. The change around midnight has been predicted by the model calculation of SCW (*McPherron et al.*, 1973; *Clauer and McPherron*, 1974). The sign changes near dawn and dusk are caused by a change of a main contribution from the FAC to the IC, and vice versa. The sign change near dawn occurs with a start of the increase in conductivities, while the sign change near dusk occurs $1-2$ h before conductivities reach the lowest level. The sign change at 10 LT is caused by a sign change in the meridional ionospheric current, which corresponds to the outward and inward current flows to the equatorial ionosphere. At
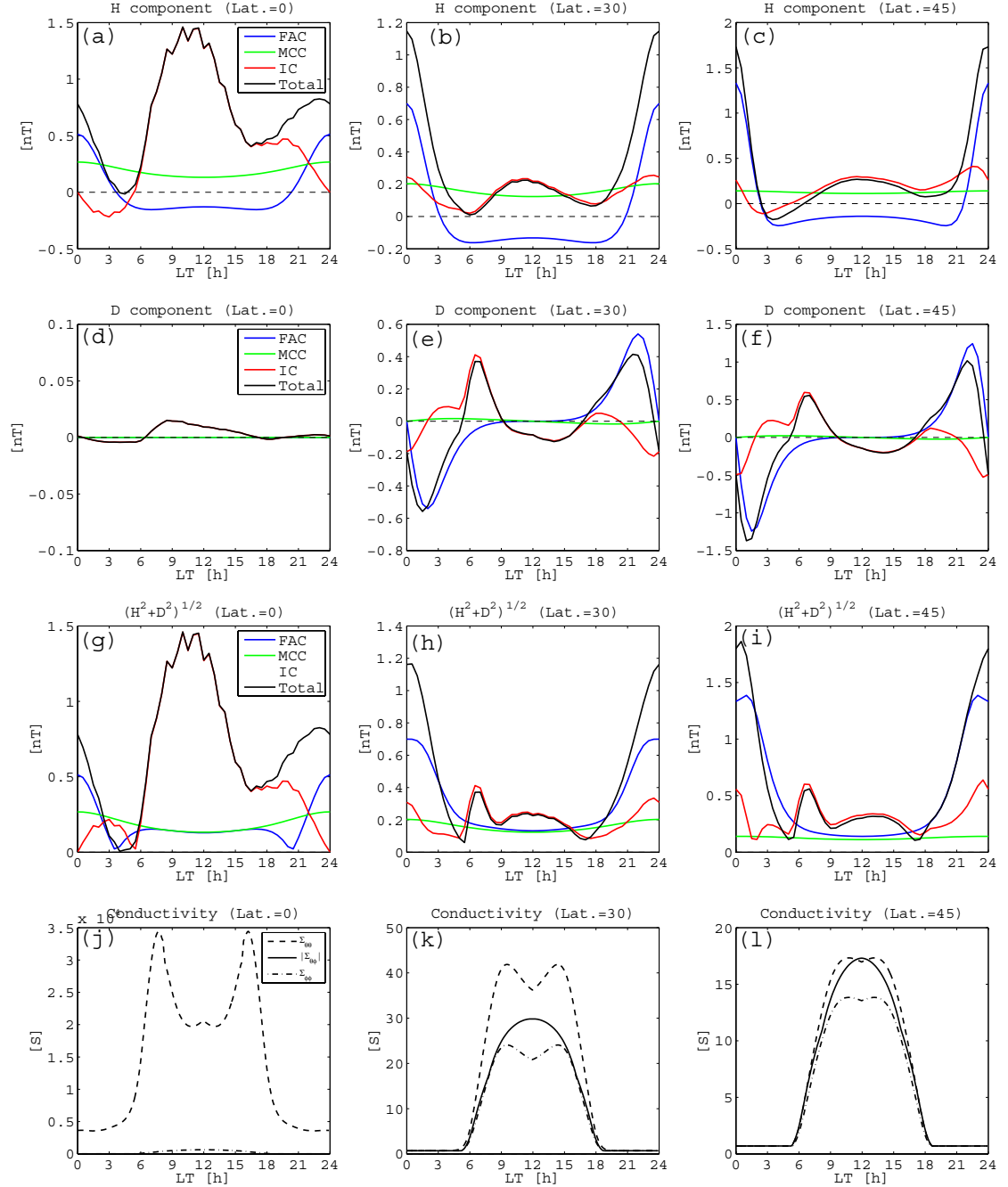
FIGURE 5.9: LT dependence of magnetic field at the specific latitudes produced by each current component at 0°, 30°, and 45° latitudes. The magnetic fields of (a)-(c) *H* components, (d)-(e) *D* components (g)-(i) absolute values of the horizontal component, and (f)-(h) the height-integrated conductivities.

the $30°$ and $45°$ latitudes, the maximum D in the prenoon sector is about 2 times larger than that in the postnoon sector.

5.2.2 Asymmetric Input Parameters

5.2.2.1 Asymmetric FACs with Respect to the Noon-midnight Meridian

I examine the effect of the location of FACs. In the averaged situation the Pi2 source is considered to be located in the premidnight sector (*Uozumi et al.*, 2007). I set the upward FAC located at 21 LT and $65°$ in latitude and downward FAC located at 23 LT and $65°$ in latitude. The same symmetric conductivity tensor is used (see Figure 5.4).

Figure 5.10 shows distributions of calculated ground magnetic field and the equivalent current in the same format as Figure 5.7. The pattern of the total equivalent current on the dayside is similar to the symmetric FAC case. The equivalent current distribution shows the prenoon-postnoon asymmetry that the meridional component in the prenoon sector is larger than in the postnoon sector. On the other hand, the total equivalent current distribution on the nightside is shifted to the premidnight sector. Looking at Figure 5.10d, one can see that this shift is clearly caused by the location of the magnetospheric current. This result indicates that the location of the FACs strongly affects the equivalent current on the nightside, while it little affects the equivalent current on the dayside.

5.2.2.2 Asymmetric Conductivity with Respect to the Equator: Summer-Winter Asymmetry

At the summer and winder solstices, the conductivity distribution is highly asymmetric with respect to the equator because the location of the terminator is not symmetric. I examine the difference between summer and winter hemispheres. The FAC and conductivity distributions at the summer solstice are shown in Figure 5.11. The conductivity tensor in the $0-12$ LT sector is mirrored in the $12-24$ LT sector. Northern Hemisphere, which is the summer hemisphere in this simulation, has a greatly high conductivity region. The FAC distribution is same as Figure 5.4a.

Figure 5.12 shows distributions of calculated ground magnetic field and the equivalent current in the same format as Figure 5.7. Naturally, the magnetospheric current contribution (Figure 5.12d) is not affected by the asymmetry of the conductivity. The ionospheric current contribution exhibits a clear asymmetry with respect to the equator. The equivalent current on the dayside summer hemisphere is about $2-3$ times stronger than that on the dayside winter hemisphere. On the contrary, the westward equivalent current in the midnight auroral region on the winter hemisphere is about 1.2 times stronger than that on the summer hemisphere. Although the summer-winter asymmetry pattern in the total equivalent distribution is notable on the dayside, the prenoon-postoon asymmetry similar to the previous result can be seen in both hemispheres.

5.3   Discussion

The calculation of ground magnetic field produced by the SCW-type current system have been studied by many previous studies (e.g., *Kisabeth and Rostoker*, 1971; *McPherron et al.*, 1973; *Clauer and McPherron*, 1974; *Samson and Rostoker*, 1983; *Sergeev et al.*,
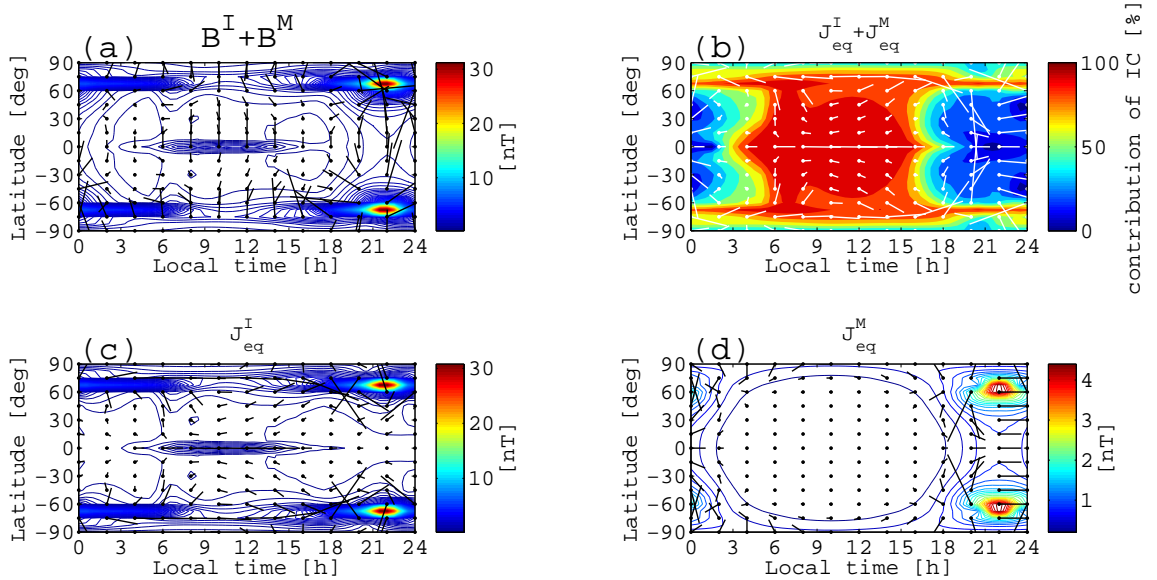
FIGURE 5.10: (a) Total calculated magnetic vectors, (b) total equivalent current vectors, (c) equivalent current vectors caused by the ionospheric current, and (d) equivalent current vectors caused by the magnetospheric current. The color contour in (a), (c), and (d) shows the absolute value of the magnetic field. The background color in (b) shows the percentage of the contribution of the ionospheric current.
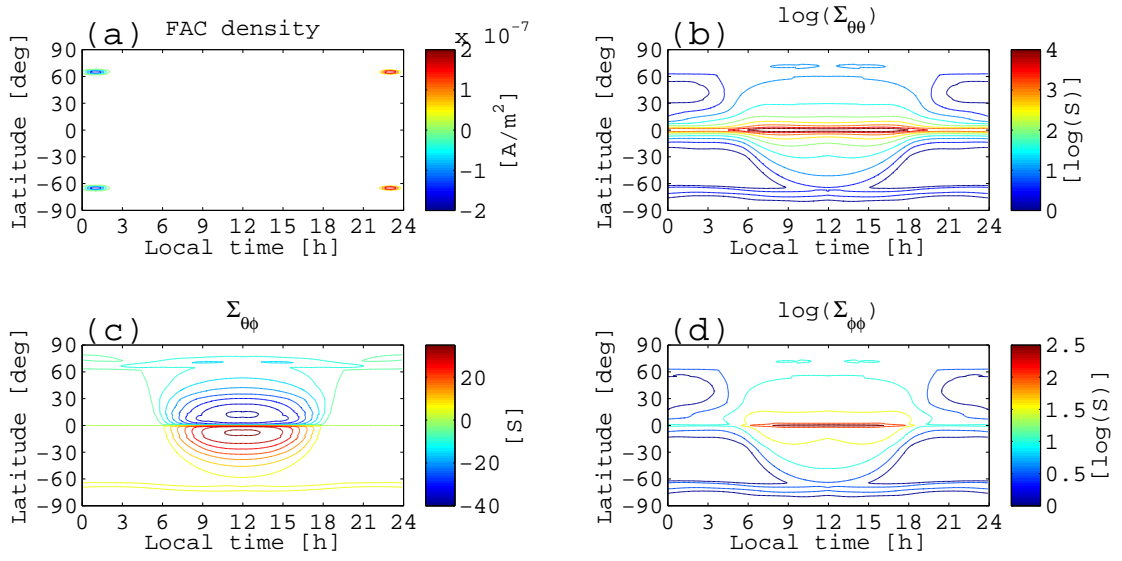
FIGURE 5.11: The distributions of (a) the FAC density at the ionospheric altitude ($j_{//}^I$), (b)-(d) Elements of the hight-integrated conductivities tensor at the summer solstice.
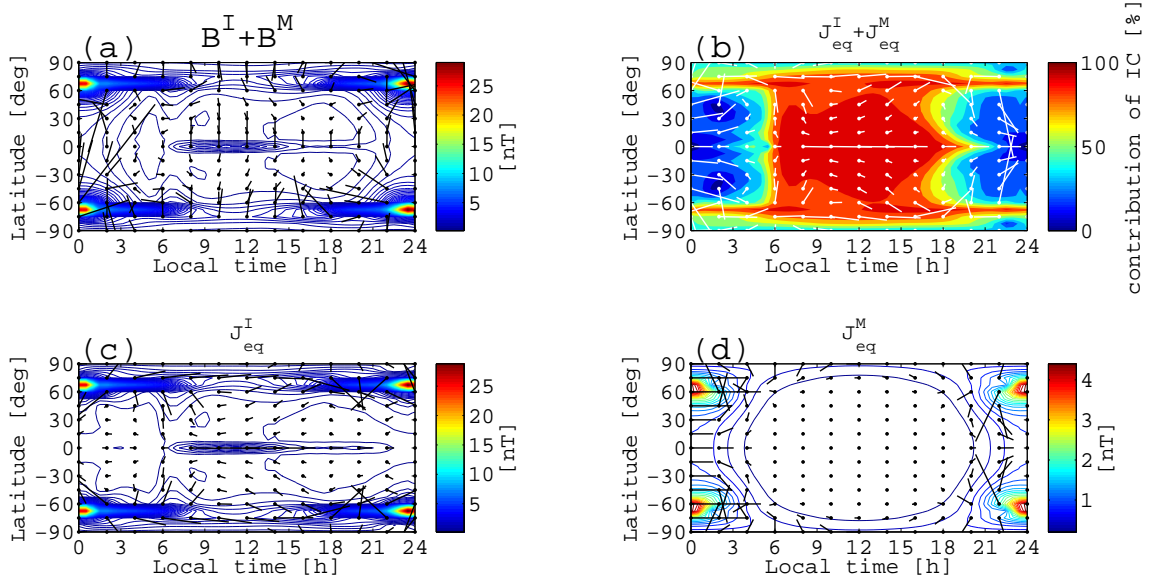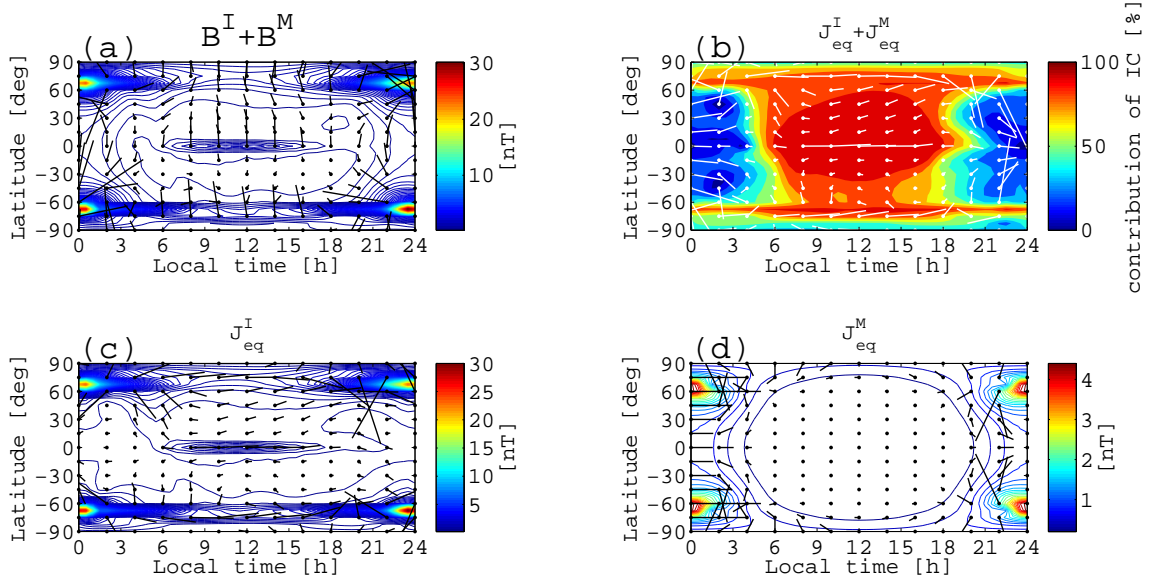

FIGURE 5.12: (a) Total calculated magnetic vectors, (b) total equivalent current vectors, (c) equivalent current vectors caused by the ionospheric current, and (d) equivalent current vectors caused by the magnetospheric current. The color contour in (a), (c), and (d) shows the absolute value of the magnetic field. The background color in (b) shows the percentage of the contribution of the ionospheric current.

2011). However, no study shows the changes in sign of the east-west magnetic field near noon and the dawn/dusk terminator. Because the purpose of these studies is to understand the magnetic field in the nightside middle-to-polar region, the dayside current closure was not taken into account. The present results of nightside magnetic

field at equatorial-to-middle latitude are consistent with previous results since the FAC distributions used in this study are basically the same and the nightside magnetic field at equatorial-to-middle latitude is mainly produced by FACs. The difference of the present study from the previous study of SCW is that I used the global ionospheric current system calculated under realistic conductivity including modification at the equator by Cowling conductivity. If the conductivity at the equator was not enough, the current would not extend to the equator because the equatorial region is far from the FAC footprint. Consequently, the meridional current that connects to the equatorial current will be weak, and the D magnetic field on the dayside will be weak.

As I expected from the present observational result, the numerical calculation shows that the D phase reversal near the terminator occurs as a result of the balance of magnetic perturbations caused by the nightside FAC and the dayside meridional ionospheric current. The D magnetic perturbation of nightside FACs hardly reaches the dayside, while the ionospheric current contribution is dominant in the dayside region where the conductivity is high.

On the dayside, the H component produced by FACs cancels out that produced by the MCC, and consequently the magnetospheric current contribution is very small. If the MCC magnetic effect is not taken into account, the H component on the dayside is very weak or even opposite sense because of the FAC contribution. Basically, the magnetic field outside the current loop is much weaker than that inside the current loop. In the present model current, the main current loop consists of the FAC, MCC and the westward electrojet. The MCC plays a role in confining the magnetic field produced by the nightside current loop.

Although the conductivity in the low-latitude dark ionosphere is very low, the magnetic field by IC on the nightside has same order as that on the dayside (See Figure 5.9b and e). Since the ionospheric current on the low-latitude dayside is weak, it is not considered that the IC contribution is only caused by the overhead ionospheric current. I suggest that, in the present simulation, the IC contribution in the low-latitude nightside region partially originates from the intense ionospheric current in the auroral region. Figure 5.13 is the LT dependence of H magnetic fields at 30° in latitude produced by total IC and IC in the latitude of −60 to 60. The difference of the two line plots means that the intense ionospheric current in the auroral region produces magnetic fields not only

just below but also at a distant point. In $22-03$ LT, the H magnetic field produced by lower latitude ionospheric currents is about $2/3-1/3$ smaller than the H magnetic field produced by the all ionospheric currents. The sense of H magnetic field produced by the auroral electrojet reverses at the certain latitude where the magnetic field is directed to the Z axis in the HZ plane because of the curve of the Earth surface. The H magnetic field produced by the westward electrojet is negative at high latitudes and positive at low latitudes.
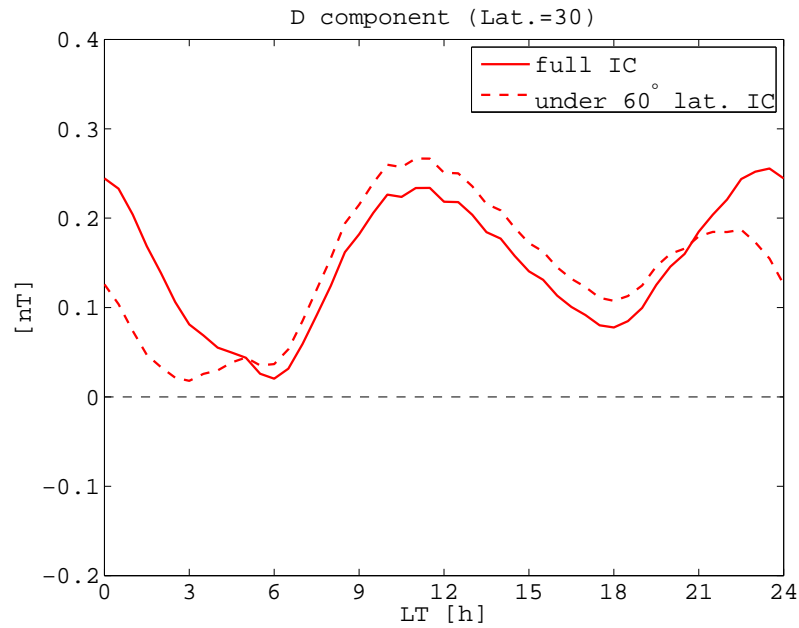
FIGURE 5.13: The LT dependence of H magnetic fields at $30°$ in latitude produced by the total IC (red solid line) and the IC in the latitude of $-60°$ to $60°$ (red broken line).

The numerical simulation reproduced the observed prenoon-postnoon asymmetry that the D component in the prenoon sector is larger than in the postnoon sector. This is due to the asymmetry of the ionospheric current on the dayside. This result supports the hypothesis that the dayside ionospheric current system produces dayside Pi2 pulsations. The reason why the ionospheric current shows the asymmetry will be discussed in the next chapter.

Features of high-latitude Pi2 may not be well explained by the oversimplified FAC configuration in this study. The features of high-latitude Pi2 are highly localized, and quite variable from event to event.This indicates that the magnetic field in the region near the FAC footprint is easily affected by the fine structure and location of the FAC. *Rostoker* (1991a,b) proposed that the SCW consisted of small-scale current elements

called "wedgelets". Using data from Cluster 1 and 4, ground-based magnetometers, and optical instruments, *Forsyth et al.* (2014) showed that there were a lot of upward and downward current sheets during a substorm but these were reduced to the simple line current model of the SCW as a sum of effects of each current element. Although the small-scale structure of Pi2-associated oscillatory FACs has not been studied by the in-situ observation by satellites, I expect that the features of the middle-to-low latitude Pi2 (especially for the D component) is a result of a sum of the magnetic effect of small-scale oscillatory wedgelets.

The ionospheric current on the dayside is less affected by the small-scale structure of FACs. The small-scale structure of the potential caused by the small-scale structure of FACs can be limited in the region near the FACs, but the small-scale potential structure is reduced to a large scale potential structure in the region distant from potential sources. The electric field distribution on the dayside may show similar pattern to the electric field distribution in the case of a simple FAC structure as used in this study. As a result, the ionospheric current near the FACs has complicated structures, while the ionospheric current pattern on the dayside depends on the large-scale pattern of FACs.

Chapter 6

General Discussion

6.1 Formation Process of Dayside Ionospheric Current Closure: Roles of the Dawn and Dusk Terminators

In this section, I discuss how the dayside ionospheric current closure including the equatorial Cowling current is formed.

Kikuchi et al. (1996) suggested that for DP2 ionospheric current system, the equatorial ionospheric current is directly connected to the upward and downward FACs as a Pedersen current. According to their model, the polar electric field is transmitted to the equatorial ionosphere in the TM_0 mode, and drives Pedersen currents and Cowling Hall currents. However, the Pedersen current at low-to-high latitude, connecting the FACs to the equatorial ionospheric current, is not strong to supply an enough current to the equatorial region because the conductivity in the prenoon and postnoon low-to-high latitude is not high compared to that in the equatorial region. To ensure current continuity, the surplus current enhanced by the Cowing effect must be closed by other closures.

The global Cowling channel (*Yoshikawa et al.*, 2012) is a model that explains the closure of the equatorial Cowling current. This model suggests that the terminator, where the conductivity is highly non-uniform, plays a role in the formation of the meridional current connecting to the equatorial current. The schematic of the model is shown in Figure 6.1. It is assumed that there are region-1 sense FACs at the dawn and dusk polar regions. In

this case, the primary Pedersen current extends from the FACs to the equatorial region, and the Pedersen current in the middle-to-low latitudes near the terminator flows along with the terminator. On the other hand, the primary Hall current near the terminator flows antisunward perpendicular to the terminator. This Hall current diverges due to a strong conductivity gradient and generates positive charges along the terminator, and the polarization electric field drives the secondary Pedersen current that cancels out the divergence of the Hall current. The polarization electric field also drives a secondary Hall current which is in the same direction as the primary Pedersen current. The meridional current is formed by the integration of the primary meridional Pedersen current and the secondary meridional Hall current. This enhancement of the meridional current near the terminator is exactly the Cowling effect due to the horizontal charge separation, which is similar to the Cowling effect of the auroral electrojet. It is considered that the secondary meridional Hall current is connected with the equatorial Cowling current, so this current channel of the secondary Hall current along the terminator and the magnetic equator is the "global Cowling channel".
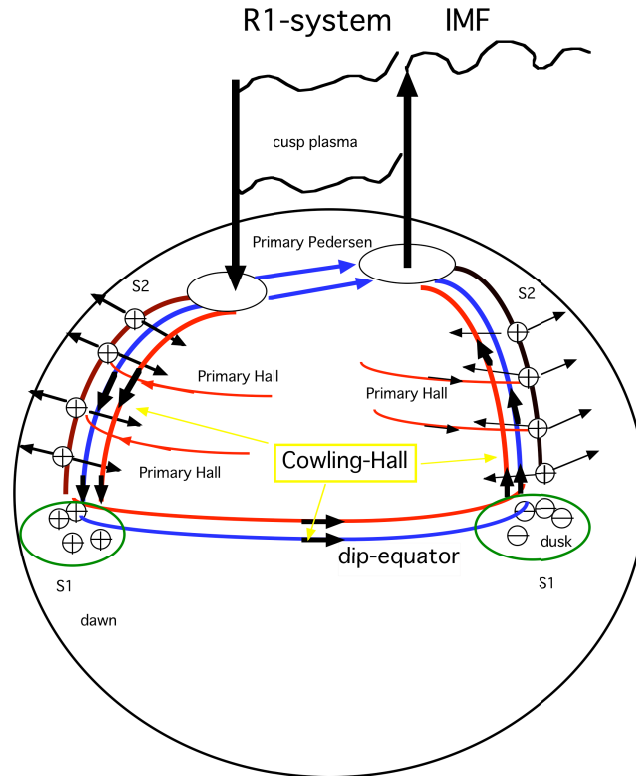
FIGURE 6.1: The schematic of the global Cowling channel produced by the region-1 sense FACs in the dawn and dusk polar regions (courtesy of Dr. Akimasa Yoshikawa).

Although the global Cowling channel model was applied to the current system produced

by region-1 sense FACs in the dawn and dusk polar regions, this model is also valid for the case of the SCW-type FACs localized near the midnight. Figure 6.2 shows the picture of the global Cowling channel produced by the nightside localized FACs. Since the primary Hall current has a substantial normal component to the terminator line, the positive Hall polarization can occur. The primary Pedersen current also has the normal component, and generate negative charge at the dawn terminator and positive charge at the dusk terminator. However, since the Hall conductivity is typically larger than the Pedersen conductivity, total electric charges at the both terminators are still positive. Thus the polarization electric field drives the meridional secondary Hall currents, which are connected to the zonal equatorial current, and consequently a global Cowling channel is formed.
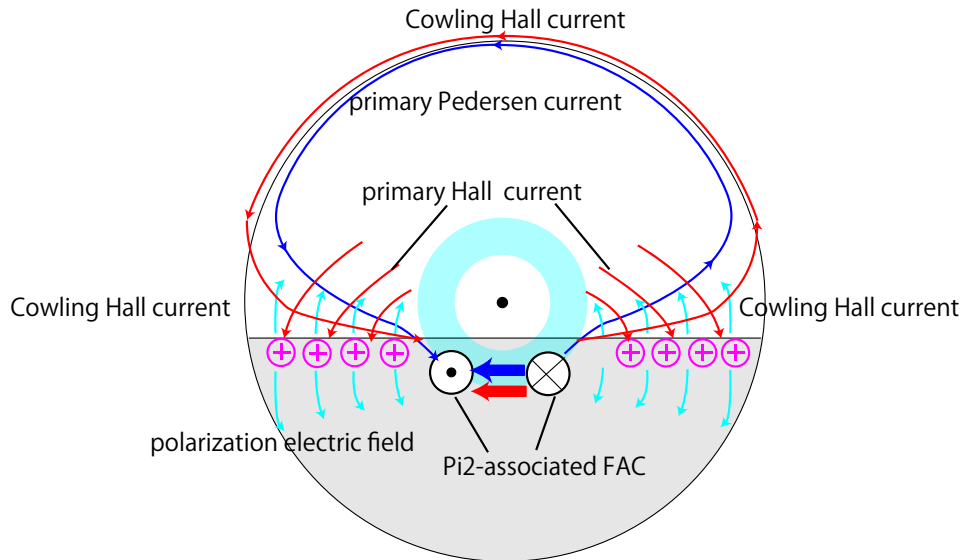
FIGURE 6.2: The schematics of the global Cowling channel produced by the SCW-type FACs localized near the midnight.

In my numerical simulation, the ionospheric current provided by the nightside FACs leaks into the dayside ionosphere through the auroral region. The leaking ionospheric current flow eastward when the sense of FACs is same as SCW. The eastward electrojet for substorm current system, which corresponds to a positive H magnetic bay, are often found in evening sector (e.g., *Akasofu and Meng*, 1967; *Kamide and Fukushima*, 1972). However, since substorm current system is a mixture of the SCW and convection (direct driven) current system (e.g., *Rostoker*, 1991b; *Kamide and Kokubun*, 1996; *Gjerloev and Hoffman*, 2001), the proposed current system for Pi2 pulsation cannot be simply compared to the substorm current system. *Rostoker* (1991b) proposed that the

eastward current in the evening sector is a part of the convection current system rather than dayside closure of the SCW. It seems unlikely that convection current system includes the Pi2 fluctuation components since the Pi2 pulsation is not a solar wind origin phenomenon.

The Cowling channel of the westward electrojet in the auroral region inside of the SCW-type current system has been considered by previous studies (*Boström*, 1964). The Cowling channel of the eastward electrojet is probably formed in the auroral region outside of the SCW-type current system. The primary Hall current flows equatorward in the outside of the SCW-type current system, and generates a positive charge along the equatorial edge of the auroral region and a negative charge along the poleward edge of the auroral region. The poleward polarization field generated by the charges drives the eastward secondary Hall current.

6.2 Prenoon-postnoon (Dawn-dusk) Asymmetry of Ionospheric Current

6.2.1 Hall Current and Polarization Effects

The simulated ground magnetic field showed that the ionospheric current contributed significantly to the dayside magnetic field. The simulated ionospheric current exhibited the prenoon-postnoon (dawn-dusk) asymmetry that the meridional current in the prenoon sector was stronger than that in the postnoon sector. Although the meridional secondary Hall current explains the closure of the equatorial Cowling current, this current closure is symmetric with respect to the noon meridian.

Yoshikawa et al. (2013) separated ionospheric currents into the primary current system and the secondary current system. The primary current system is composed of the primary Pedersen current and secondary Pedersen current driven by the Pedersen polarization field. This current system is directly connected with the input FACs. The primary current system has an antisymmetric structure as long as FACs are antisymmetric and conductivity distributions are symmetric with respect to the central meridian of the input upward and downward FACs. The secondary current system is composed of the total Hall current and the secondary Pedersen current driven by Hall polarization

fields. This current system is not directly connected with FACs but its divergence is cancel out the divergence of the primary current system at the edge of a conductivity gradient. Because the symmetric Hall current is driven by antisymmetric charges and the antisymmetric Hall current is driven by symmetric charges, the summention of Hall current itself and currents driven by Hall polarization has a mixture structure of symmetric and antisymmetric structures. Thus the secondary current system becomes an asymmetric, distorts the total current system. I suggest that, in the secondary current, the Hall current driven by the primary field mainly causes the prenoon-postnoon asymmetry of the meridional current. Figure 6.3 is a schematics of this explanation. When the premidnight FAC is upward and postmidnight FAC is downward, the meridional component of the primary Hall current on the dayside flows equatorward. Thus, the equatorward Cowling current in the prenoon sector is enhanced and the poleward Cowling current in the postnoon sector is reduced.
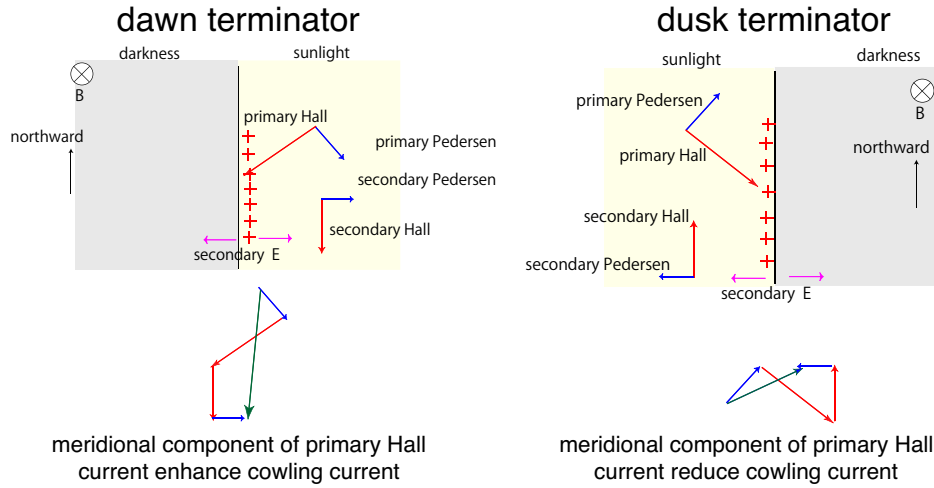
FIGURE 6.3: The schematics explaining role of the primary Hall current in the prenoon-postnoon asymmetry.

In this thesis I give only a qualitative explanation for the asymmetry of the ionospheric current system due to the physical nature of the ionospheric current. Numerical separations between Pedersen and Hall currents and between primary and secondary currents are necessary for further understanding reasons for the prenoon-postnoon asymmetry.

6.2.2 Configuration of Field-Aligned Currents

I discuss the possibility that the configuration of FACs affects the structure of the dayside current system. Figure 6.4 shows the simulated ionospheric currents produced by a pair of downward and upward FACs shifted duskward and dawnward. In the case of duskward shifted FACs (Figure 6.4a), the peaks of upward and downward FACs are located at 21 LT and 23 LT, respectively. The configuration of the dayside ionospheric currents is basically the same as the case of symmetric FACs shown in Figure 5.6. The dawnward shifted FAC system, in which the peaks of upward and downward FACs are located at 1 LT and 3 LT, respectively, also generates a similar dayside current system (Figure 6.4b). These results indicate that the shape of the dayside current system does not strongly depend on the configuration of FACs. Thus the present model suggests that locations of Pi2-associated FACs for individual events are not significant for dayside equivalent currents.
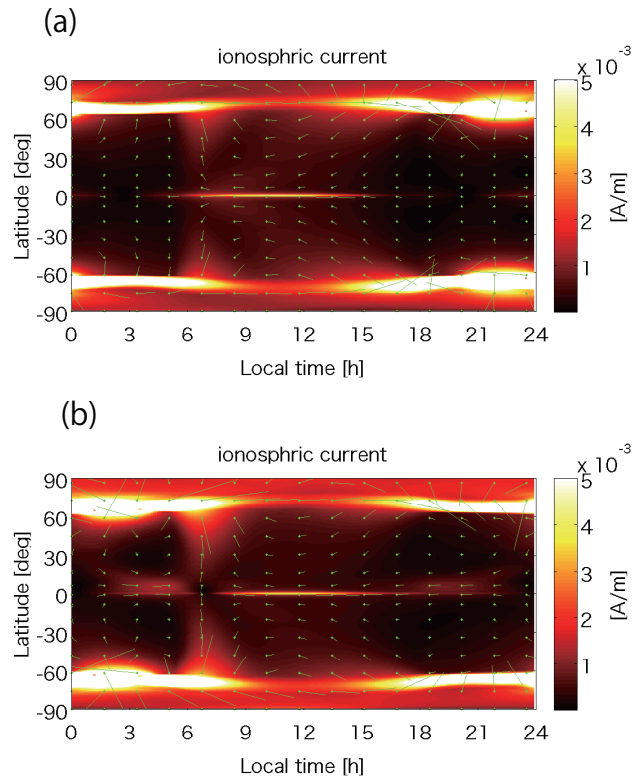
FIGURE 6.4: Simulated ionospheric current distributions produced by a pair of downward and upward FACs shifted (b) duskward (2100 LT and 2300 LT) and (b) dawnward (0100 LT and 0300).

6.2.3 Asymmetry of the Equatorial Current

The asymmetric current system also explains the asymmetry of the amplitude of Pi2 at the magnetic equator. *Yumoto and the CPMN Group* (2001) reported that horizontal amplitude of Pi2 observed at the equatorial POH station (0.09° geomagnetic latitude) is maximized at 10 LT (Figure 5 in their paper). The LT dependence of Pi2 amplitude on the dayside is similar to the H component at the equator calculated by the present model (Figure 5.9a). The calculated dayside H component reflects the zonal ionospheric current. The peak of ionospheric current is shifted to the dawnward because the intense prenoon meridional current flows into the narrower width of the equatorial region than the postnoon meridional current.

6.3 Causes of Small Phase Shift

If the Pi2 pulsations driven by only the simultaneous electrostatic current oscillation, the Pi2 is purely linearly polarized and their phase relations are just 0° or 180°. Although the longitudinal phase variation shown in this study is roughly constant or 180° steplike change, there are some cases in which phases are not distributed around 0°/180° or gradually change (Figure 3.20). Also the time difference of the peak of the horizontal amplitude is small (within 10 s) but they are slightly earlier at the noon than at the prenoon and the postnoon (Figure 4.13).

One reason is the uncertainty of an estimation of phase differences. Since Pi2 pulsations are impulsive and irregular oscillations, their spectrum densities tend to be broad and change with time. Also, data contain variations other than Pi2 pulsations in some degree. These uncertainties affect the degree of variability but may not cause the bias of the variability.

The other possibility is that the phase is changed by some Pi2 components driven by a mechanism other than the electrostatic current oscillation. These Pi2 components are not always necessary to be in phase with the electrostatic current oscillation. If these components do not have the gradual phase variation (finite propagation time), they can be a cause of phase shifts of the total magnetic oscillation because the modulation of the phase depends on the amplitude and initial phase the of additional components.

One such Pi2 components is fast mode waves. If the initial phase is different from the electrostatic oscillation, they can cause the phase shift. *Uozumi et al.* (2009) showed that the time delay between the middle-latitude D component and low-latitude H component is very small (nearly antiphase or in-phase relation). They considered that D oscillations were mainly driven by the oscillation of the SCW and H oscillations were mainly caused by the fast mode wave. They suggested that the start of the current oscillation and arrival of the fast mode wave is nearly simultaneous. In this case, the phase modulation by the fast mode wave is very small. The Alfvén wave driven by the fast mode wave may cause a larger propagation delay toward sunward direction but this delay is not significant at low latitudes. On the dayside around the noon, the effect of fast mode wave probably small because the Pi2 is not observed in the dayside magnetosphere and F-region ionosphere. In dawn and dusk regions, although the fast mode wave is attenuating during sunward propagation, the fast mode wave may contribute to the ground magnetic field (mainly H component) to some extent.

Another possibility is propagation and inductive effects of ionospheric electric fields. If the electric field propagates over the globe from the footprint of the FACs with a significant propagation time relative to a period of Pi2, this propagation effect may cause the time delay of the driving of the ionospheric current. The TM_0 mode wave (*Kikuchi*, 2014) propagates at the speed of light from the polar ionosphere to the dayside equatorial ionosphere within ~0.05 s, which is much shorter than a period of Pi2 ($40-150$ s). The propagation effect of the electric field may not affect the phase of the P2.

The inductive ionospheric current can change the phase of Pi2. The inductive horizontal electric field is given as

$$-\frac{\partial \mathbf{B}}{\partial t} = \nabla \times \mathbf{E}. \tag{6.1}$$

If the initial ionospheric current is given by a harmonic function, the phase of the primary inductive field induced by the magnetic field produced by the initial current is delayed by $90°$ from the initial current. The inductive current driven by the inductive electric field changes the phase of the initial ionospheric current. Each element of the current closures has different inductance and conductance. The phase shift due to the inductive effect is different from location to location. *Shinohara et al.* (1998) estimated the inductance and

resistance of ionosphere-ground current circuit at low latitudes and the magnetic equator, where the conductivity was assumed to be one order larger than that of low latitudes. From their estimation, the phase difference of $\sim 30°$ can arise from an inductive effect. However, the current circuit is not realistic because the vertical displacement current is included. The Pi2 period is too long to generate effective displacement current.

In chapter 4, phases of ASB D in the prenoon sector and TUC D in the postnoon sector relative to HON H near the noon meridian are delayed by $\sim 45°$ from the in-phase and antiphase relations, respectively. The D component may reflect a part of meridional ionospheric current connecting to the equatorial current. On the other hand, the low-latitude current closure on the noon meridian plane does not involve the equatorial current. The current closure including the equatorial region may have a large inductance because the length of the current line is long. The conductance is also large because this current closure has a Cowling conductivity. The current closure including prenoon and postnoon low latitudes and the equatorial region may have larger inductive effect than that in the low latitude noon. A numerical estimation of the inductive effect of the global current system is worth investigating in further study.

However, I emphasize that the electrostatic current oscillation can explain the major part of the longitudinal phase structure at low-to-middle latitudes. Although other components of Pi2 pulsation (FACs, MHD waves, induced ionospheric currents) would exist, I conclude that major part of Pi2 on dayside and near the terminator is produced by the electrostatic oscillation of the three dimensional current system.

Chapter 7

Summary

7.1 Summary and Conclusion of this Thesis

This thesis presented detail observations of dayside Pi2s and terminator Pi2s using the middle-to-equatorial latitude ground magnetic data provided from multiple worldwide ground-based magnetometer networks (MAGDAS/CPMN, INTERMAGNET, Mc-MAC). The model current system proposed by this thesis provided a quantitative interpretation of the observational results.

The thesis first clarifies the effects of dawn and dusk terminators on the Pi2 pulsations. I examined Pi2 pulsations observed simultaneously at middle-to-low latitude stations around dawn and dusk terminators. The phase reversal of the D component occurred around dawn and dusk terminators whereas the H component was nearly in phase. The D component was in antiphase with respect to the magnetic equator not only in darkness but also in sunlight. A statistical analysis using Pi2 events that occurred during 1 November 2011 to 31 October 2012 showed that some features of Pi2s are controlled by the relative location of the terminator (at 100 km in altitude, where the highly conducting E region is located) rather than local time. The phase reversal of the D component occurred $0.5-1$ h after sunrise and $1-2$ h before sunset. The D-to-H amplitude ratio on the dawn side started to increase at sunrise and reached a peak at approximately 2 h after sunrise, while the D-to-H amplitude ratio on the dusk side reached a peak at sunset. The change of the features controlled by the terminator cannot be explained by existing models alone (e.g., plasmaspheric resonance, substorm current

89

wedge oscillation). I suggested that the terminator effect can be explained by a change in contributing currents, namely the FACs on the nightside to the ionospheric currents on the sunlit side of the terminator, and vice versa. The ionospheric current on the sunlit side was expected to be a part the dayside current system (Figure 3.23).

I analyzed some Pi2 events using at least 36 magnetometers in the dayside middle-to-equatorial latitude region (geomagnetic latitude lower than $60°$ and the sunlit region at 100 km in altitude) to examine the dayside ionospheric current system. I derived equivalent current distributions, which are a useful approach to visualize the ionospheric current structure if the magnetic effect of ionospheric current is dominant in the examined region. Equivalent current vectors of Pi2 are determined by rotating the filtered horizontal magnetic field vectors at the local maxima of the horizontal amplitude ($\sqrt{\Delta H^2 + \Delta D^2}$, where ΔH and ΔD are bandpass filtered north-south and east-west component geomagnetic data, respectively, with a period of 40 to 150 s) by an angle of $90°$ clockwise. The local maxima of the horizontal amplitude of Pi2 occurs nearly simultaneous at almost all dayside stations, indicating that their oscillations in the direction of the major axis are nearly in phase. The meridional component of equivalent current vectors was reversed between in the prenoon sector and the postnoon sector, so as to connect the equatorial equivalent current to higher latitude regions. The equivalent currents exhibited the prenoon-postnoon asymmetry that the ratio of the meridional component to the zonal component in prenoon sector was larger than that in the postnoon sector. To systematically test the generality of these features, I statistically analyzed dayside Pi2s observed simultaneously at the longitudinally separated three stations (ASB, HON and TUC) in prenoon, noon, and postnoon sectors during 1 November 2011 to 31 October 2012. It was confirmed that the averaged features are consistent with the feature of the individual events shown in case studies. Based on the current system in Figure 3.23, I proposed the current system including the skewed dayside ionospheric current which can explain the prenoon-postnoon asymmetry of the Pi2 feature (Figure 4.16).

The present observational results imply that dayside Pi2s are associated with oscillating ionospheric currents. To quantitatively examine the proposed model current system, I calculated the ground magnetic field produced by the three-dimensional current system consisting of FACs localized in the nightside auroral region, the magnetospheric closure current, and the ionospheric current produced by the FACs. The magnetic field is calculated by the generalized Biot-Savart law in the spherical coordinates. The current

distribution of the current system was derived from the FAC density at the ionospheric altitude and the height-integrated ionospheric conductivity tensor given by the method of *Nakamizo et al.* (2012). It was assumed that the FACs flowed along the dipole field line, and the magnetospheric closure current flowed in azimuthal direction to connect between equatorial footprints of the center of the FACs. The ionospheric current was derived by numerically solving the global electrostatic potential distribution. The simulated ionospheric current on the dayside showed the similar pattern to the observed equivalent current on the dayside. The simulated equivalent current also showed the similar pattern to the observed equivalent current on the dayside, indicating that the ionospheric current mainly contributes to the dayside equivalent current. On the other hand, since the ionospheric current is very weak at nightside low latitudes, the magnetospheric current contribute mainly to the magnetic field in this region. The sense of simulated both H and D magnetic field is consistent with the longitudinal phase variation of the observed Pi2. By separation of the contribution of each current element, it was found that D component phase reveals around the terminator are caused by a change in contributing currents, namely FACs or meridional ionospheric currents.

While the previous Pi2 model for low latitudes cannot explain the observational result, the proposed model current system well explains the magnetic vector (or equivalent current vector) of Pi2 magnetic perturbation. The asymmetry of the dayside ionospheric current is due to the Hall current and its polarization field. The formation of the polar-to-equatorial ionospheric current implies that global Cowling channel (*Yoshikawa et al.*, 2012) can be applied to the nightside-source phenomena. I conclude that Pi2 pulsations are sent to the dayside ground by the quasi-electrostatic oscillating ionospheric current formed in the polar-to-equatorial region driven by localized nightside FACs.

7.2 Future Works

The location of Pi2-associated FAC regions was not determined for each event, and this thesis discusses only typical configuration of the FACs. In reality, the location of FAC varies from event to event, and the magnetic effect on the ground differ from event to event. To give further support to the present model, it is necessary to determine the configuration of FACs and use this information as input for the calculation of the ground magnetic field. A method of the determination is auroral observations. The localized

periodic intensification of auroral probably indicates the ionospheric footprint of the Pi2 associated FACs (e.g., *Nishimura et al.*, 2012). The dense and wide magnetic observation may be also used to determine the distribution of Pi2-associated FACs. However, since the conductivity in the nightside auroral region during the expansion phase is highly variable and nonuniform, the vortex center of the equivalent current does not match the FAC location. Only middle latitude magnetic data can be used to estimate an approximate central meridian of large-scale structure of FACs (*Lester et al.*, 1983).

The direct evidence for the existence of the Pi2-associated dayside ionospheric current has not been found. If the ionospheric current exists, the magnetic field observed at the upper side of the current and lower side of the current is in antiphase. However, most low-altitude satellite observations show that Pi2 pulsations were not detected in the F region ionosphere ($400-600$ km). Since the typical altitude of the intense ionospheric current is 90-130km, the satellite location is far from the current sheet. Moreover, the ground induced current enhances the ground magnetic field and reduces the magnetic field above the current sheet. The amplitude of the dayside ground magnetic field is small (typically smaller than 1 nT), Pi2 in the F region driven by the E region current may be very small and not enough to be detected. In future, the Pi2 can be detected in the dayside ionosphere if a satellite that have high time-resolution magnetometer in the very low altitude (around 200 km) will be operated. One possible way is to use the data when a satellite was descending. The CHAMP satellite started to drastically descend at the beginning of 2008 and crashed at the beginning of 2009. The altitude in the last half year is below 300 km, there may be a chance to detect signal of dayside Pi2s over an ionospheric current layer.

Appendix A

Derivation of the equation of FAC distribution in the magnetosphere

In this appendix, the derivation of equation 5.1.1 is shown.

The unit vector component of the dipole field is given by

$$\hat{e} = \frac{2\cot\theta}{\sqrt{4\cot^2\theta + 1}}\hat{r} + \frac{1}{\sqrt{4\cot^2\theta + 1}}\hat{\boldsymbol{\theta}} \tag{A.1}$$

Thus the ratios between $j_{//r}^M$ and $j_{//\theta}^M$ and between surface elements dS_r and dS_θ are given by

$$\frac{j_{//r}^M}{j_{//\theta}^M} = \frac{dS_r}{dS_\theta} = \frac{1}{2\cot\theta}. \tag{A.2}$$

The current intensity along a field line element is constant:

$$
\begin{aligned}
J_{//}^I &= J_{//}^M \\
j_{//}^I dS^I &= j_{//}^M dS \\
\sqrt{{j_{//r}^I}^2 + {j_{//\theta}^I}^2}\sqrt{{dS_r^I}^2 + {dS_\theta^I}^2} &= \sqrt{{j_{//r}^M}^2 + {j_{//\theta}^M}^2}\sqrt{{dS_r}^2 + {dS_\theta}^2}.
\end{aligned}
\tag{A.3}
$$

Using A.2 and A.3, I obtain the following relation,

$$
\begin{aligned}
j_{//r}^I dS_r^I &= j_{//r}^M dS_r \\
j_{//r}^M &= \frac{r^{I2} \sin \theta^I d\theta^I}{r^2 \sin \theta d\theta} j_{//r}^I.
\end{aligned}
\tag{A.4}
$$

Using the relation $r d\theta / dr = 1/2 \cot \theta$ for the dipole field line and replacing θ by θ^I, I obtain the equation,

$$
\frac{d\theta^I}{d\theta} = \frac{\cot \theta}{\cot \theta^I}.
\tag{A.5}
$$

I substitute equation A.5 into equation A.4:

$$
\begin{aligned}
j_{//r}^M &= \frac{r^{I2} \sin \theta^I \cot \theta}{r^2 \sin \theta \cot \theta^I} \frac{2 \cot \theta^I}{\sqrt{4 \cot \theta^I + 1}} j_{//}^I \\
j_{//r}^M &= \frac{r^{I2} \sin \theta^I}{r^2 \sin \theta} \frac{1}{\sqrt{4 \cot \theta^I + 1}} 2 \cot \theta j_{//}^I
\end{aligned}
\tag{A.6}
$$

$j_{//\theta}^M$ also can be derived in the same manner above.

Appendix B

Illustration in Polar Coordinates

The following figures are same as figures in Section 5.2.1 except that these are illustrated by polar coordinates.
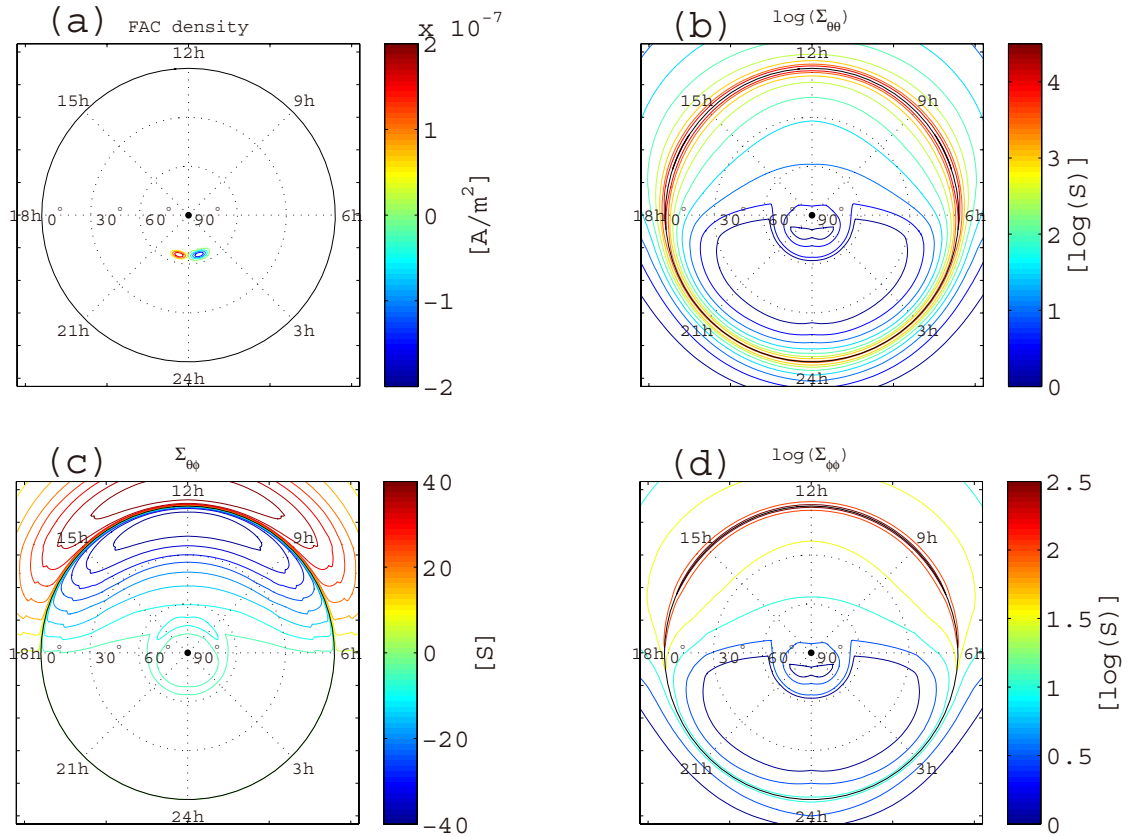
FIGURE B.1: Illustration by polar coordinates of Figure 5.4. The distributions of (a) the FAC density at the ionospheric altitude $(j_{//}^I)$, (b)-(d) Elements of the hight-integrated conductivities tensor.
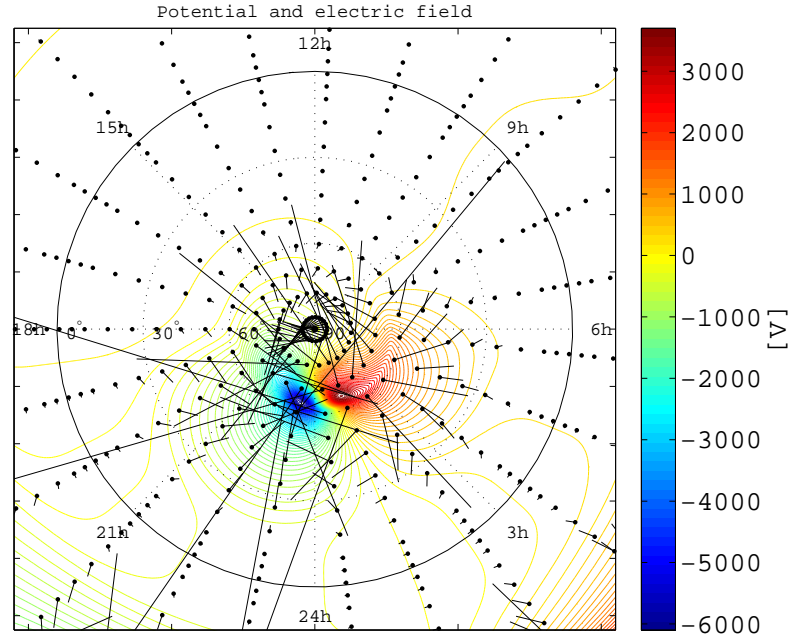
FIGURE B.2: Illustration by polar coordinates of Figure 5.5. Distributions of the ionospheric potential (Φ) and ionospheric electric field (**E**) vector.
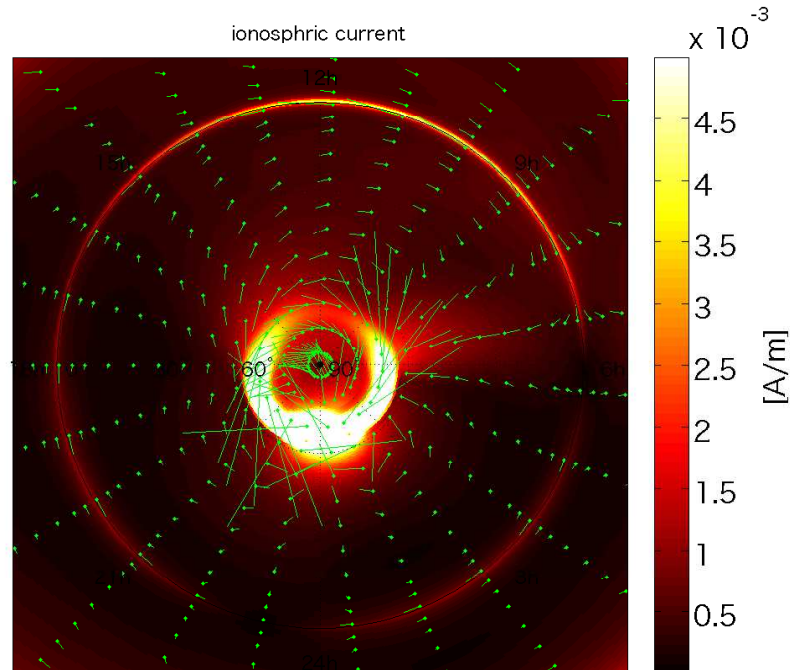
FIGURE B.3: Illustration by polar coordinates of Figure 5.6. Simulated height-integrated ionospheric current distribution (**J**). The background color shows the current amplitude (|**J**|).
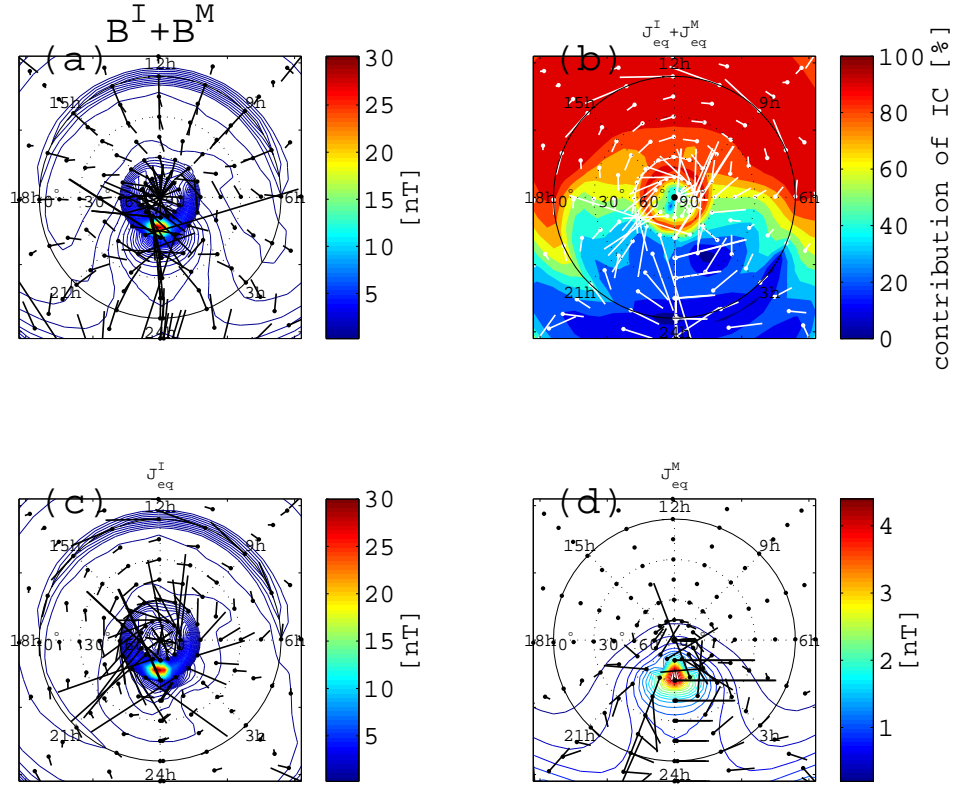
FIGURE B.4: Illustration by polar coordinates of Figure 5.7. (a) Total magnetic vectors, (b) total equivalent current vectors, (c) equivalent current vectors caused by the ionospheric current, and (d) equivalent current vectors caused by the magnetospheric current. The color contour in (a), (c), and (d) shows the absolute value of the magnetic field. The background color in (b) shows the percentage of the contribution of the ionospheric current.
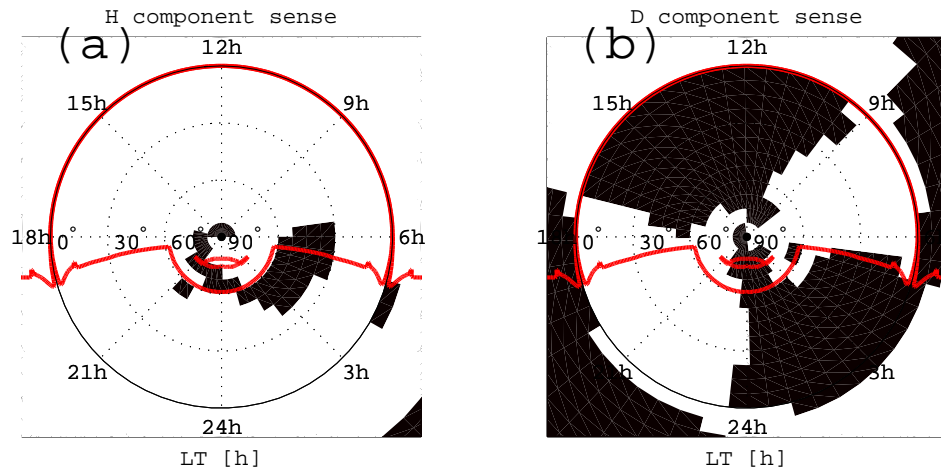
FIGURE B.5: Illustration by polar coordinates of Figure 5.8. The distributions of sign of (a) H and (b) D components. The red line shows the isoline of $|\Sigma_{\theta\phi}| = 0.8$, which indicates that edges of conductivity near the terminator and the auroral region.

Bibliography

Akasofu, S.-I., and C.-I. Meng (1967), Polar magnetic substorm in the evening sector, *J. Atmos. Terr. Phys.*, *29*(9), 1127 – 1135, doi:10.1016/0021-9169(67)90145-6.

Allan, W., F. W. Menk, B. J. Fraser, Y. Li, and S. P. White (1996), Are low-latitude Pi2 pulsations cavity/waveguide modes?, *Geophys. Res. Lett.*, *23*(7), 765–768, doi:10.1029/96GL00661.

Alperovich, L., B. Fidel, and O. Saka (1996), A determination of the hydromagnetic waves polarization from their perturbations on the terminator, *Ann. Geophys.*, *14*(6), 647–658, doi:10.1007/s00585-996-0647-9.

Araki, T. (1977), Global structure of geomagnetic sudden commencements, *Planet. Space. Sci.*, *25*(4), 373 – 384, doi:10.1016/0032-0633(77)90053-8.

Araki, T. (1994), A Physical Model of the Geomagnetic Sudden Commencement, in *Solar Wind Sources of Magnetospheric Ultra-Low-Frequency Waves*, *Geophys. Monogr. Ser.*, vol. 81, edited by M. J. Engebretson, K. Takahashi, and M. Scholer, pp. 183–200, American Geophysical Union, Washington, D. C., doi:10.1029/GM081p0183.

Baumjohann, W., and R. Treumann (2012), *Basic Space Plasma Physics*, Imperial College Press.

Boström, R. (1964), A model of the auroral electrojets, *J. Geophys. Res.*, *69*(23), 4983–4999, doi:10.1029/JZ069i023p04983.

Boström, R. (1972), Magnetosphere-ionosphere coupling, in *Critical Problems of Magnetospheric Physics*, vol. 1, p. 139.

Cao, J., J. Duan, A. Du, Y. Ma, Z. Liu, G. Zhou, D. Yang, T. Zhang, X. Li, M. Vellante, et al. (2008), Characteristics of middle- to low-latitude Pi2 excited by bursty bulk flows, *J. Geophys. Res.*, *113*(A7), doi:10.1029/2007JA012629.

Chi, P. J., C. T. Russell, and S. Ohtani (2009), Substorm onset timing via traveltime magnetoseismology, *Geophys. Res. Lett.*, *36*(8), doi:10.1029/2008GL036574.

Chi, P. J., M. J. Engebretson, M. B. Moldwin, C. T. Russell, I. R. Mann, M. R. Hairston, M. Reno, J. Goldstein, L. I. Winkler, J. L. Cruz-Abeyro, D.-H. Lee, K. Yumoto, R. Dalrymple, B. Chen, and J. P. Gibson (2013), Sounding of the plasmasphere by Mid-continent MAgnetoseismic Chain (McMAC) magnetometers, *J. Geophys. Res. Space Physics*, *118*(6), 3077–3086, doi:10.1002/jgra.50274.

Clauer, C. R., and R. L. McPherron (1974), Mapping the local time-universal time development of magnetospheric substorms using mid-latitude magnetic observations, *J. Geophys. Res.*, *79*(19), 2811–2820, doi:10.1029/JA079i019p02811.

Collier, A. B., A. R. W. Hughes, L. G. Blomberg, and P. R. Sutcliffe (2006), Evidence of standing waves during a Pi2 pulsation event observed on cluster, *Ann. Geophys.*, *24*(10), 2719–2733, doi:10.5194/angeo-24-2719-2006.

Ebihara, Y., T. Tanaka, and T. Kikuchi (2014), Counter equatorial electrojet and over-shielding after substorm onset: Global MHD simulation study, *J. Geophys. Res. Space Physics*, *119*(9), 7281–7296, doi:10.1002/2014JA020065, 2014JA020065.

Ellis, P., and D. Southwood (1983), Reflection of Alfvén waves by non-uniform iono-spheres, *Planet. Space Sci.*, *31*(1), 107 – 117, doi:10.1016/0032-0633(83)90035-1.

Ellis, W. (1899), Relation between magnetic disturbance and solar spot frequency, *Monthly Notices of the Royal Astronomical Society*, *60*, 148.

Fejer, J. (1953), Semidiurnal currents and electron drifts in the ionosphere, *J. Atmos. Terr. Phys.*, *4*(4), 184–203, doi:10.1016/0021-9169(53)90054-3.

Ferraro, V., and H. Unthank (1951), Sudden commencements and sudden impulses in geomagnetism: Their diurnal variation in amplitude, *Geofisica pura e applicata*, *20*(1), 27–30, doi:10.1007/BF01996889.

Forbes, J. M. (1981), The equatorial electrojet, *Reviews of Geophysics*, *19*(3), 469–504, doi:10.1029/RG019i003p00469.

Forbush, S. E., and E. H. Vestine (1955), Daytime enhancement of size of sudden com-mencements and initial phase of magnetic storms at Huancayo, *J. Geophys. Res.*, *60*(3), 299–316, doi:10.1029/JZ060i003p00299.

Forsyth, C., A. N. Fazakerley, I. J. Rae, C. E. J. Watt, K. Murphy, J. A. Wild, T. Karlsson, R. Mutel, C. J. Owen, R. Ergun, A. Masson, M. Berthomier, E. Donovan, H. U. Frey, J. Matzka, C. Stolle, and Y. Zhang (2014), In situ spatiotemporal measurements of the detailed azimuthal substructure of the substorm current wedge, *J. Geophys. Res. Space Physics*, *119*(2), 927–946, doi:10.1002/2013JA019302.

Ghamry, E., K.-H. Kim, H.-J. Kwon, D.-H. Lee, J.-S. Park, J. Choi, K. Hyun, W. S. Kurth, C. Kletzing, J. R. Wygant, and J. Huang (2015), Simultaneous Pi2 observations by the Van Allen Probes inside and outside the plasmasphere, *J. Geophys. Res. Space Physics*, *120*(6), 4567–4575, doi:10.1002/2015JA021095.

Gjerloev, J. W., and R. A. Hoffman (2001), The convection electric field in auroral substorms, *J. Geophys. Res.*, *106*(A7), 12,919–12,931, doi:10.1029/1999JA000240.

Glassmeier, K.-H. (1983), Reflection of MHD-waves in the Pc4-5 period range at ionospheres with non-uniform conductivity distributions, *Geophys. Res. Lett.*, *10*(8), 678–681, doi:10.1029/GL010i008p00678.

Han, D. S., T. Iyemori, M. Nosé, H. McCreadie, Y. Gao, F. Yang, S. Yamashita, and P. Stauning (2004), A comparative analysis of low-latitude Pi2 pulsations observed by Ørsted and ground stations, *J. Geophys. Res.*, *109*, A10209, doi:10.1029/2004JA010576.

Hardy, D. A., M. Gussenhoven, R. Raistrick, and W. McNeil (1987), Statistical and functional representations of the pattern of auroral energy flux, number flux, and conductivity, *J. Geophys. Res.*, *92*(A11), 12,275–12,294, doi:10.1029/JA092iA11p12275.

Hashimoto, K. K., T. Kikuchi, S. Watari, and M. A. Abdu (2011), Polar-equatorial ionospheric currents driven by the region 2 field-aligned currents at the onset of substorms, *J. Geophys. Res.*, *116*, A09217, doi:10.1029/2011JA016442.

Hirono, M. (1950a), On the influence of the Hall current to the electrical conductivity of the ionosphere. I, *J. Geomagn. Geoelectr.*, *2*(1), 1–8, doi:10.5636/jgg.2.1.

Hirono, M. (1950b), On the influence of the Hall current to the electrical conductivity of the ionosphere, II, *J. Geomagn. Geoelectr.*, *2*(4), 113–120, doi:10.5636/jgg.2.113.

Hirono, M. (1952), A theory of diurnal magnetic variations in equatorial regions and conductivity of the ionosphere *E* region, *J. Geomagn. Geoelectr.*, *4*(1), 7–21, doi: 10.5636/jgg.4.7.

Hsu, T. S., R. L. McPherron, V. Angelopoulos, Y. Ge, H. Zhang, C. Russell, X. Chu, and J. Kissinger (2012), A statistical analysis of the association between fast plasma flows and Pi2 pulsations, *J. Geophys. Res.*, *117*, A11221, doi:10.1029/2012JA018173.

Imajo, S., K. Yumoto, T. Uozumi, H. Kawano, S. Abe, A. Ikeda, K. Koga, H. Matsumoto, T. Obara, R. Marshall, V. A. Akulichev, A. Mahrous, A. Liedloff, and A. Yoshikawa (2014), Analysis of propagation delays of compressional Pi 2 waves between geosynchronous altitude and low latitudes, *Earth Planets Space*, *66*(1), 20, doi:10.1186/1880-5981-66-20.

Imajo, S., A. Yoshikawa, T. Uozumi, S. Ohtani, A. Nakamizo, R. Marshall, B. M. Shevtsov, V. A. Akulichev, U. Sukhbaatar, A. Liedloff, and K. Yumoto (2015), Pi2 pulsations observed around the dawn terminator, *J. Geophys. Res. Space Physics*, *120*(3), 2088–2098, doi:10.1002/2013JA019691.

Itonaga, M., and T. Kitamura (1988), Effect of non-uniform ionospheric conductivity distributions on Pc3–5 magnetic pulsations–Alfvén wave incidence, *J. Geomagn. Geoelectr.*, *40*(12), 1413–1435, doi:10.5636/jgg.40.1413.

Itonaga, M., and A. Yoshikawa (1996), The excitation of share Alfvén wave and the associated modulation of compressional wave in the inner magnetosphere, *J. Geomagn. Geoelectr.*, *48*, 1451.

Itonaga, M., and K. Yumoto (1998), ULF waves and the ground magnetic field, *J. Geophys. Res.*, *103*(A5), 9285–9291, doi:10.1029/98JA00288.

Itonaga, M., T.-I. Kitamura, O. Saka, H. Tachihara, M. Shinohara, and A. Yoshikawa (1992), Discrete spectral structure of low-latitude and equatorial Pi2 pulsation., *J. Geomagn. Geoelectr.*, *44*(3), 253–259.

Jacobs, J., and T. Watanabe (1962), Propagation of hydromagnetic waves in the lower exosphere and the origin of short period geomagnetic pulsations, *J. Atmos. Terr. Phys.*, *24*(6), 413 – 434, doi:10.1016/0021-9169(62)90207-6.

Jacobs, J. A., Y. Kato, S. Matsushita, and V. A. Troitskaya (1964), Classification of geomagnetic micropulsations, *J. Geophys. Res.*, *69*(1), 180–181, doi:10.1029/JZ069i001p00180.

Kamide, Y., and N. Fukushima (1972), Positive geomagnetic bays in evening high latitudes and their possible connection with partial ring current, *Rep. Ionos. Space Res. Jap.*, *26*, 79–101.

Kamide, Y., and S. Kokubun (1996), Two-component auroral electrojet: Importance for substorm studies, *J. Geophys. Res.*, *101*(A6), 13,027–13,046, doi:10.1029/96JA00142.

Kamide, Y., and S. Matsushita (1979), Simulation studies of ionospheric electric fields and currents in relation to field-aligned currents, 2. substorms, *J. Geophys. Res.*, *84*(A8), 4099–4115, doi:10.1029/JA084iA08p04099.

Kamide, Y., A. D. Richmond, and S. Matsushita (1981), Estimation of ionospheric electric fields, ionospheric currents, and field-aligned currents from ground magnetic records, *J. Geophys. Res.*, *86*(A2), 801–813, doi:10.1029/JA086iA02p00801.

Keiling, A. (2012), Pi2 pulsations driven by ballooning instability, *J. Geophys. Res. Space Physics*, *117*(A3), A03228, doi:10.1029/2011JA017223.

Keiling, A., and K. Takahashi (2011), Review of Pi2 models, *Space Sci. Rev.*, *161*, 63–148, doi:10.1007/s11214-011-9818-4.

Keiling, A., V. Angelopoulos, D. Larson, J. McFadden, C. Carlson, M. Fillingim, G. Parks, S. Frey, K.-H. Glassmeier, H. U. Auster, W. Magnes, W. Liu, and X. Li (2008), Multiple intensifications inside the auroral bulge and their association with plasma sheet activities, *J. Geophys. Res. Space Physics*, *113*(A12), A12216, doi:10.1029/2008JA013383.

Keiling, A., O. Marghitu, J. Vogt, O. Amm, C. Bunescu, V. Constantinescu, H. Frey, M. Hamrin, T. Karlsson, R. Nakamura, H. Nilsson, J. Semeter, and E. Sorbalo (2014), Magnetosphere-ionosphere coupling of global Pi2 pulsations, *J. Geophys. Res. Space Physics*, *119*(4), 2717–2739, doi:10.1002/2013JA019085.

Kepko, L., and M. Kivelson (1999), Generation of Pi2 pulsations by bursty bulk flows, *J. Geophys Res.*, *104*(A11), 25,021–25,034, doi:10.1029/1999JA900361.

Kepko, L., M. G. Kivelson, and K. Yumoto (2001), Flow bursts, braking, and Pi2 pulsations, *J. Geophys. Res.*, *106*(A2), 1903–1915.

Kerridge, D. (2001), INTERMAGNET: Worldwide near-real-time geomagnetic observatory data, in *Proceedings of the Workshop on Space Weather, ESTEC*, vol. 34.

Kikuchi, T. (2014), Transmission line model for the near-instantaneous transmission of the ionospheric electric field and currents to the equator, *J. Geophys. Res.*, *119*(2), 1131–1156, doi:10.1002/2013JA019515.

Kikuchi, T., and T. Araki (1979a), Transient response of uniform ionosphere and preliminary reverse impulse of geomagnetic storm sudden commencement, *J. Atmos. Terr. Phys.*, *41*(9), 917 – 925, doi:10.1016/0021-9169(79)90093-X.

Kikuchi, T., and T. Araki (1979b), Horizontal transmission of the polar electric field to the equator, *J. Atmos. Terr. Phys.*, *41*, 927–936, doi:10.1016/0021-9169(79)90094-1.

Kikuchi, T., T. Araki, H. Maeda, and K. Maekawa (1978), Transmission of polar electric fields to the equator, *Nature*, *273*(5664), 650–651, doi:10.1038/273650a0.

Kikuchi, T., H. Lühr, T. Kitamura, O. Saka, and K. Schlegel (1996), Direct penetration of the polar electric field to the equator during a DP 2 event as detected by the auroral and equatorial magnetometer chains and the EISCAT radar, *J. Geophys. Res.*, *101*(A8), 17,161–17,173, doi:10.1029/96JA01299.

Kikuchi, T., K. K. Hashimoto, T.-I. Kitamura, H. Tachihara, and B. Fejer (2003), Equatorial counterelectrojets during substorms, *J. Geophys. Res. Space Physics*, *108*(A11), 1406, doi:10.1029/2003JA009915.

Kim, K.-H., H.-J. Kwon, D.-H. Lee, H. Jin, K. Takahashi, V. Angelopoulos, J. W. Bonnell, K. H. Glassmeier, Y.-D. Park, and P. Sutcliffe (2010), A comparison of THEMIS Pi2 observations near the dawn and dusk sectors in the inner magnetosphere, *J. Geophys. Res.*, *115*, A12226, doi:10.1029/2010JA016010.

Kisabeth, J. L., and G. Rostoker (1971), Development of the polar electrojet during polar magnetic substorms, *J. Geophys. Res.*, *76*(28), 6815–6828, doi:10.1029/JA076i028p06815.

Kisabeth, J. L., and G. Rostoker (1977), Modelling of three-dimensional current systems associated with magnetospheric substorms, *Geophysical Journal International*, *49*(3), 655–683, doi:10.1111/j.1365-246X.1977.tb01310.x.

Kitamura, T., O. Saka, M. Shimoizumi, H. Tachihara, T. Oguti, T. Araki, N. Sato, M. Ishitsuka, O. Veliz, and J. B. Nyobe (1988), Global mode of Pi2 waves in the equatorial region: Difference of Pi2 mode between high and equatorial latitudes, *J. Geomagn. Geoelectr.*, *40*, 621–634, doi:10.5636/jgg.40.621.

Kwon, H.-J., K.-H. Kim, D.-H. Lee, K. Takahashi, V. Angelopoulos, E. Lee, H. Jin, Y.-D. Park, J. Lee, P. R. Sutcliffe, and H. U. Auster (2012), Local time-dependent Pi2 frequencies confirmed by simultaneous observations from THEMIS probes in the inner magnetosphere and at low-latitude ground stations, *J. Geophys. Res.*, *117*, A01206, doi:10.1029/2011JA016815.

Lee, D.-H., and K. Takahashi (2006), MHD Eigenmodes in the Inner Magnetosphere, in *Magnetospheric ULF Waves: Synthesis and New Directions*, *Geophys. Monogr. Ser.*, vol. 169, edited by K. Takahashi, P. J. Chi, R. E. Denton, and R. L. Lysak, pp. 73–89, American Geophysical Union, Washington, D. C., doi:10.1029/169GM07.

Lester, M., J. W. Hughes, and H. J. Singer (1983), Polarization patterns of Pi 2 magnetic pulsations and the substorm current wedge, *J. Geophys. Res.*, *88*(A10), 7958–7966, doi:10.1029/JA088iA10p07958.

Lester, M., W. J. Hughes, and H. J. Singer (1984), Longitudinal structure in Pi 2 pulsations and the substorm current wedge, *J. Geophys. Res. Space Physics*, *89*(A7), 5489–5494, doi:10.1029/JA089iA07p05489.

Lester, M., K. H. Glassmeier, and J. Behrens (1985), Pi 2 pulsations and the eastward electrojet: A case study, *Planet. Space Sci.*, *33*, 351, doi:10.1016/0032-0633(85)90066-2.

Li, Y., B. J. Fraser, F. W. Menk, D. J. Webster, and K. Yumoto (1998), Properties and sources of low and very low latitude Pi2 pulsations, *J. Geophys. Res.*, *103*(A2), 2343–2358, doi:10.1029/97JA02921.

Lin, C. A., L. C. Lee, and Y. J. Sun (1991), Observations of Pi 2 pulsations at a very low latitude (L = 1.06) station and magnetospheric cavity resonances, *J. Geophys. Res.*, *96*(A12), 21,105–21,113, doi:10.1029/91JA02029.

Liou, K., C.-I. Meng, P. T. Newell, K. Takahashi, S.-I. Ohtani, A. T. Y. Lui, M. Brittnacher, and G. Parks (2000), Evaluation of low-latitude Pi2 pulsations as indicators of substorm onset using Polar ultraviolet imagery, *J. Geophys. Res.*, *105*(A2), 2495–2505, doi:10.1029/1999JA900416.

Lui, A. T. Y. (1996), Current disruption in the earth's magnetosphere: Observations and models, *J. Geophys. Res.*, *101*(A6), 13,067–13,088, doi:10.1029/96JA00079.

Lyons, L. R., T. Nagai, G. T. Blanchard, J. C. Samson, T. Yamamoto, T. Mukai, A. Nishida, and S. Kokubun (1999), Association between Geotail plasma flows and auroral poleward boundary intensifications observed by CANOPUS photometers, *J. Geophys. Res.*, *104*(A3), 4485–4500, doi:10.1029/1998JA900140.

Maeda, H., and M. Yamamoto (1960), Daytime enhancement of the amplitude of geomagnetic sudden impulses in the equatorial region, *J. Atmos. Terr. Phys.*, *19*(3), 284 – 287, doi:10.1016/0021-9169(60)90050-7.

Matsushita, S. (1960), Studies on sudden commencements of geomagnetic storms using IGY data from United States stations, *J. Geophys. Res.*, *65*(5), 1423–1435, doi:10.1029/JZ065i005p01423.

McPherron, R. L., C. T. Russell, and M. P. Aubry (1973), Satellite studies of magnetospheric substorms on August 15, 1968: 9. Phenomenological model for substorms, *J. Geophys. Res.*, *78*(16), 3131–3149, doi:10.1029/JA078i016p03131.

Mene, N. M., A. T. Kobea, O. K. Obrou, K. Z. Zaka, K. Boka, C. Amory-Mazaudier, and P. Assamoi (2011), Statistical study of the DP2 enhancement at the dayside dip-equator compared to low latitudes, *Ann. Geophys.*, *29*(12), 2225–2233, doi:10.5194/angeo-29-2225-2011.

Motoba, T., T. Kikuchi, H. Lühr, H. Tachihara, T.-I. Kitamura, K. Hayashi, and T. Okuzawa (2002), Global Pc5 caused by a DP 2−type ionospheric current system, *J. Geophys. Res.*, *107*(A2), SMP 8–1–SMP 8–12, doi:10.1029/2001JA900156.

Murphy, K. R., I. R. M. I. J. Rae, A. P. Walsh, A. P. Milling, and A. Kale (2011), The dependence of Pi2 waveforms on periodic velocity enhancements within bursty bulk flows, *Ann. Geophys.*, *29*, 493–509, doi:10.5194/angeo-29-493-2011.

Nakamizo, A., Y. Hiraki, Y. Ebihara, T. Kikuchi, K. Seki, T. Hori, A. Ieda, Y. Miyoshi, Y. Tsuji, Y. Nishimura, and A. Shinbori (2012), Effect of R2-FAC development on the ionospheric electric field pattern deduced by a global ionospheric potential solver, *J. Geophys. Res.*, *117*, A09231, doi:10.1029/2012JA017669.

Nishida, A. (1968), Geomagnetic Dp 2 fluctuations and associated magnetospheric phenomena, *J. Geophys. Res.*, *73*(5), 1795–1803, doi:10.1029/JA073i005p01795.

Nishimura, Y., L. Lyons, T. Kikuchi, V. Angelopoulos, E. Donovan, S. Mende, P. Chi, and T. Nagatsuma (2012), Formation of substorm Pi2: A coherent response to auroral streamers and currents, *J. Geophys. Res.*, *117*, A09218, doi:10.1029/2012JA017889.

Nosé, M., K. Takahashi, T. Uozumi, K. Yumoto, Y. Miyoshi, A. Morioka, D. K. Milling, P. R. Sutcliffe, H. Matsumoto, T. Goka, and H. Nakata (2003), Multipoint observations of a Pi2 pulsation on morningside: The 20 september 1995 event, *J. Geophys. Res.*, *108*(A5), 1219, doi:10.1029/2002JA009747.

Nosé, M., K. Liou, and P. R. Sutcliffe (2006), Longitudinal dependence of characteristics of low-latitude Pi2 pulsations observed at Kakioka and Hermanus, *Earth Planets Space*, *58*, 775–783, doi:10.1186/BF03351981.

Olson, J. V. (1999), Pi2 pulsations and substorm onsets: A review, *J. Geophys. Res.*, *104*(A8), 17,499–17,520, doi:10.1029/1999JA900086.

Panov, E. V., R. Nakamura, W. Baumjohann, V. Angelopoulos, A. A. Petrukovich, A. Retino, M. Volwerk, T. Takada, K.-H. Glassmeier, J. P. McFadden, and D. Larson (2010), Multiple overshoot and rebound of a bursty bulk flow, *Geophys. Res. Lett.*, *37*(8), L08103, doi:10.1029/2009GL041971.

Panov, E. V., W. Baumjohann, R. Nakamura, O. Amm, M. V. Kubyshkina, K. H. Glassmeier, J. M. Weygand, V. Angelopoulos, A. A. Petrukovich, and V. A. Sergeev (2013), Ionospheric response to oscillatory flow braking in the magnetotail, *J. Geophys. Res.*, *118*(4), 1529–1544, doi:10.1002/jgra.50190.

Pashin, A. B., K. H. Glassmeier, W. Baumjohann, O. M. Raspopov, A. G. Yahin, H. J. Opgenoorth, and R. J. Pellinen (1982), Pi 2 magnetic pulsations, auroral break-ups and the substorm current wedge: A case study, *J. Geophys.*, *51*, 223.

Peymirat, C., and D. Fontaine (1994), Numerical simulation of magnetospheric convection including the effect of field-aligned currents and electron precipitation, *J. Geophys. Res.*, *99*(A6), 11,155–11,176, doi:10.1029/93JA02546.

Rostoker, G. (1991a), Auroral signatures of magnetospheric substorms and constraints which they provide for substorm theories, *J. Geomagn. Geoelectr.*, *43*(Supplement1), 233–243, doi:10.5636/jgg.43.Supplement1_233.

Rostoker, G. (1991b), Some Observational Constraints for Substorm Models, in *Magnetospheric Substorms*, *Geophys. Monogr. Ser.*, vol. 64, edited by J. R. Kan, T. A. Potemra, S. Kokubun, and T. Iijima, pp. 61–72, American Geophysical Union, Washington, D. C., doi:10.1029/GM064p0061.

Russell, C. T., and R. L. McPherron (1973), Semiannual variation of geomagnetic activity, *J. Geophys. Res.*, *78*(1), 92–108, doi:10.1029/JA078i001p00092.

Saito, T., and S. Matsushita (1968), Solar cycle effects on geomagnetic Pi 2 pulsations, *J. Geophys. Res.*, *73*(1), 267–286, doi:10.1029/JA073i001p00267.

Saito, T., K. Yumoto, and Y. Koyama (1976), Magnetic pulsation Pi2 as a sensitive indicator of magnetospheric substorm, *Planet. Space Sci.*, *24*(11), 1025–1029, doi:10.1016/0032-0633(76)90120-3.

Saka, O., T. J. Iijima, and T. Kitamura (1980), Ionospheric control of low latitude geomagnetic micropulsations, *J. Atmos. Terr. Phys.*, *42*(5), 517–520, doi:10.1007/BF00203620.

Saka, O., M. Itonaga, and T. Kitamura (1982), Ionospheric control of polarization of low-latitude geomagnetic micropulsations at sunrise, *J. Atmos. Terr. Phys.*, *44*(8), 703 – 712, doi:10.1016/0021-9169(82)90132-5.

Sakurai, T., and T. Saito (1976), Magnetic pulsation Pi2 and substorm onset, *Planet. Space Sci.*, *24*(6), 573–575, doi:10.1016/0032-0633(76)90135-5.

Samson, J. (1982), Pi 2 pulsations: High latitude results, *Planet. Space Sci.*, *30*(12), 1239–1247, doi:10.1016/0032-0633(82)90097-6.

Samson, J., and G. Rostoker (1983), Polarization characteristics of Pi 2 pulsations and implications for their source mechanisms: Influence of the westward traveling surge, *Planet. Space Sci.*, *31*(4), 435–458, doi:10.1016/0032-0633(83)90157-5.

Sarma, S., and T. Sastry (1995), On the equatorial electrojet influence on geomagnetic pulsation amplitudes, *J. Atmos. Terr. Phys.*, *57*(7), 749–754, doi:10.1016/0021-9169(94)00053-Q.

Sergeev, V. A., N. A. Tsyganenko, M. V. Smirnov, A. V. Nikolaev, H. J. Singer, and W. Baumjohann (2011), Magnetic effects of the substorm current wedge in a "spread-out wire" model and their comparison with ground, geosynchronous, and tail lobe data, *J. Geophys. Res. Space Physics*, *116*(A7), A07218, doi:10.1029/2011JA016471.

Shinohara, M., K. Yumoto, A. Yoshikawa, O. Saka, S. I. Solovyev, E. F. Vershinin, N. B. Trivedi, and J. M. D. Costa (1997), Wave characteristics of daytime and nighttime Pi 2 pulsations at the equatorial and low latitudes, *Geophys. Res. Lett.*, *24*, 2279–2282, doi:10.1029/97GL02146.

Shinohara, M., K. Yumoto, N. Hosen, A. Yoshikawa, H. Tachihara, O. Saka, T.-I. Kitamura, N. B. Trivedi, J. M. D. Costa, and N. J. Schuch (1998), Wave characteristics of geomagnetic pulsations across the dip equator, *Geophys. Res. Rett.*, *103*(A6), 11,745–11,754, doi:10.1029/97JA03067.

Stuart, W., and H. Barsczus (1980), Pi's observed in the daylight hemisphere at low latitudes, *J. Atmos. Terr. Phys.*, *42*(5), 487–497, doi:10.1016/0021-9169(80)90009-4.

Sugiura, M. (1953), The solar diurnal variation in the amplitude of sudden commencements of magnetic storms at the geomagnetic equator, *J. Geophys. Res.*, *58*(4), 558–559, doi:10.1029/JZ058i004p00558.

Sutcliffe, P. R., and H. Lühr (2010), A search for dayside geomagnetic Pi2 pulsations in the CHAMP low-Earth-orbit data, *J. Geophys. Res.*, *115*, A05205, doi:10.1029/2009JA014757.

Sutcliffe, P. R., and K. Yumoto (1989), dayside Pi 2 pulsations at low latitudes, *Geophys. Res. Lett.*, *16*(8), 887–890, doi:10.1029/GL016i008p00887.

Sutcliffe, P. R., and K. Yumoto (1991), On the cavity mode nature of low-latitude Pi 2 pulsations, *J. Geophys. Res.*, *96*(A2), 1543–1551, doi:10.1029/90JA02007.

Takahashi, K., and K. Liou (2004), Longitudinal structure of low-latitude Pi2 pulsations and its dependence on aurora, *J. Geophys. Res. Space Physics*, *109*(A12), A12206, doi:10.1029/2004JA010580.

Takahashi, K., S. Ohtani, and B. J. Anderson (1995), Statistical analysis of Pi 2 pulsations observed by the AMPTE CCE spacecraft in the inner magnetosphere, *J. Geophys. Res.*, *100*(A11), 21,929–21,941, doi:10.1029/95JA01849.

Takahashi, K., S.-i. Ohtani, W. J. Hughes, and R. R. Anderson (2001), CRRES observation of Pi2 pulsations: Wave mode inside and outside the plasmasphere, *J. Geophys. Res. Space Physics*, *106*(A8), 15,567–15,581, doi:10.1029/2001JA000017.

Takahashi, K., D.-H. Lee, M. Nosé, R. R. Anderson, and W. J. Hughes (2003), CRRES electric field study of the radial mode structure of Pi 2 pulsations, *J. Geophys. Res.*, *108*(A5), 1210, doi:10.1029/2002JA009761.

Tamao, T. (1964), The structure of three-dimensional hydromagnetic waves in a uniform cold plasma, *J. Geomagn. Geoelectr.*, *18*, 89, doi:10.5636/jgg.16.89.

Tanaka, Y.-M., K. Yumoto, A. Yoshikawa, M. Itonaga, M. Shinohara, S. Takasaki, and B. J. Fraser (2007), Horizontal amplitude and phase structure of low-latitude pc 3 pulsations around the dawn terminator, *J. Geophys. Res.*, *112*(A11), A11308, doi:10.1029/2007JA012585.

Trivedi, N. B., B. R. Arora, A. L. Padilha, J. M. Da Costa, S. L. G. Dutra, F. H. Chamalaun, and A. Rigoti (1997), Global Pc5 geomagnetic pulsations of March 24, 1991, as observed along the American Sector, *Geophys. Res. Lett.*, *24*(13), 1683–1686, doi:10.1029/97GL00215.

Tsunomura, S. (1999), Numerical analysis of global ionospheric current system including the effect of equatorial enhancement, *Ann. Geophys.*, *17*(5), 692–706, doi:10.1007/s00585-999-0692-2.

Tsunomura, S., and T. Araki (1984), Numerical analysis of equatorial enhancement of geomagnetic sudden commencement, *Planet. Space Sci.*, *32*(5), 599–604, doi:10.1016/0032-0633(84)90109-0.

Uozumi, T., K. Yumoto, H. Kawano, A. Yoshikawa, J. V. Olson, S. I. Solovyev, and E. F. Vershinin (2000), Characteristics of energy transfer of Pi 2 magnetic pulsations: Latitudinal dependence, *Geophys. Res. Rett.*, *27*(11), 1619–1622, doi:10.1029/1999GL010767.

Uozumi, T., K. Yumoto, H. Kawano, A. Yoshikawa, S. Ohtani, J. V. Olson, S.-I. Akasofu, S. I. Solovyev, E. F. Vershinin, K. Liou, and C.-I. Meng (2004), Propagation characteristics of Pi 2 magnetic pulsations observed at ground high-latitudes, *J. Geophys. Res.*, *109*, A08203, doi:10.1029/2003JA009898.

Uozumi, T., H. Kawano, A. Yoshikawa, M. Itonaga, and K. Yumoto (2007), Pi2 source region in the magnetosphere deduced from CPMN data, *Planet. Space Sci.*, *55*, 849–857, doi:10.1016/j.pss.2006.03.016.

Uozumi, T., S. Abe, K. Kitamura, T. Tokunaga, A. Yoshikawa, H. Kawano, R. Marshall, R. J. Morris, B. M. Shevtsov, S. I. Solovyev, D. J. McNamara, K. Liou, S. Ohtani, M. Itonaga, and K. Yumoto (2009), Propagation characteristics of Pi 2 pulsations observed at high- and low-latitude MAGDAS/CPMN stations: A statistical study, *J. Geophys. Res.*, *114*, A11207, doi:10.1029/2009JA014163.

Uozumi, T., K. Yumoto, T. Tokunaga, S. I. Solovyev, B. M. Shevtsov, R. Marshall, K. Liou, S. Ohtani, S. Abe, A. Ikeda, K. Kitamura, A. Yoshikawa, H. Kawano, and M. Itonaga (2011), AKR modulation and global Pi2 oscillation, *J. Geophys. Res.*, *116*(A6), A06214, doi:10.1029/2010JA016042.

Van Der Vorst, H. A. (1992), BI-CGSTAB: A Fast and Smoothly Converging Variant of BI-CG for the Solution of Nonsymmetric Linear Systems, *SIAM J. Sci. Stat. Comput.*, *13*(2), 631–644, doi:10.1137/0913035.

Voronkov, I. O., E. F. Donovan, and J. C. Samson (2003), Observations of the phases of the substorm, *J. Geophys. Res.*, *108*(A2), 1073, doi:10.1029/2002JA009314.

Welch, P. D. (1967), The use of fast Fourier transform for the estimation of power spectra: A method based on time averaging over short, modified periodograms, *Audio and Electroacoustics, IEEE Transactions on*, *15*(2), 70–73, doi:10.1109/TAU.1967.1161901.

Wilhelm, K., J. W. Münch, and G. Kremser (1977), Fluctuations of the auroral zone current system and geomagnetic pulsations, *J. Geophys. Res.*, *82*(19), 2705–2716, doi:10.1029/JA082i019p02705.

Wolf, R. A. (1970), Effects of ionospheric conductivity on convective flow of plasma in the magnetosphere, *J.Geophys. Res.*, *75*(25), 4677–4698, doi:10.1029/JA075i025p04677.

Yanagihara, K., and N. Shimizu (1966), Equatorial enhancement of micro-pulsation pi-2, *Mem. Kakioka Mag. Obs.*, *12*, 57–63.

Yeoman, T., and D. Orr (1989), Phase and spectral power of mid-latitude Pi2 pulsations: Evidence for a plasmaspheric cavity resonance, *Planet. Space Sci.*, *37*(11), 1367 – 1383, doi:10.1016/0032-0633(89)90107-4.

Yeoman, T. K., M. P. Freeman, G. D. Reeves, M. x, and D. Orr (1994), A comparison of midlatitude Pi 2 pulsations and geostationary orbit particle injections as substorm indicators, *J. Geophys. Res.*, *99*(A3), 4085–4093, doi:10.1029/93JA03233.

Yoshikawa, A. (2002), Excitation of a Hall-current generator by field-aligned current closure, via an ionospheric, divergent Hall-current, during the transient phase of magnetosphere–ionosphere coupling, *J. Geophys. Res.*, *107*(A12), SMP 18–1–SMP 18–16, doi:10.1029/2001JA009170, 1445.

Yoshikawa, A., O. S., A. Nakamizo, T. Uozumi, and Y.-M. Tanaka (2012), Formation of Cowling channel from polar to equatorial ionosphere, Abstract SM13C-06 presented at 2012 AGU Fall Meeting, San Francisco, Calif., 3−7 Dec, .

Yoshikawa, A., O. Amm, H. Vanhamäki, A. Nakamizo, and R. Fujii (2013), Theory of Cowling channel formation by reflection of shear Alfven waves from the auroral ionosphere, *J. Geophys. Res. Space Physics*, *118*(10), 6416–6425, doi:10.1002/jgra. 50514.

Yumoto, K., and the CPMN Group (2001), Characteristics of Pi 2 magnetic pulsations observed at the CPMN stations: A review of the STEP results, *Earth Planets Space*, *53*(10), 981–992, doi:10.1186/BF03351695.

Yumoto, K., and the MAGDAS Group (2006), MAGDAS project and its application for space weather, in *Solar Influence on the Heliosphere and Earth's Environment: Recent Progress and Prospects*, edited by N. Gopalswamy and A. Bhattacharya, pp. 399–405, Quest Publications, Wheaton.

Yumoto, K., and the MAGDAS Group (2007), Space weather activities at SERC for IHY: MAGDAS, *Bull. Astr. Soc. India*, *35*, 511–522.

Yumoto, K., K. Takahashi, T. Saito, F. W. Menk, B. J. Fraser, T. A. Potemra, and L. J. Zanetti (1989), Some aspects of the relation between Pi $1 − 2$ magnetic pulsations

observed at $L = 1.3 - 2.1$ on the ground and substorm-associated magnetic field variations in the near-Earth magnetotail observed by AMPTE CCE, *J. Geophys. Res.*, *94* (A4), 3611–3618, doi:10.1029/JA094iA04p03611.